DEWETTING OF THIN FILMS ON FLEXIBLE SUBSTRATES VIA DIRECT-WRITE LASER EXPOSURE

by

ANTHONY JESUS FERRER

A dissertation submitted to the

Graduate School-New Brunswick

Rutgers, The State University of New Jersey

In partial fulfillment of the requirements

For the degree of

Doctor of Philosophy

Graduate Program in Materials Science and Engineering

Written under the direction of

Professor GLENN G. AMATUCCI

And approved by

_____

_____

_____

_____

New Brunswick, New Jersey

May, 2015

ABSTRACT OF THE DISSERTATION

Dewetting of Thin Films on Flexible Substrates via Direct-Write Laser Exposure

By ANTHONY JESUS FERRER

Dissertation Advisor:

Glenn G. Amatucci

Microelectromechanical systems (MEMS) have enabled a wide variety of technologies both in the consumer space and in industrial/research areas. At the market level, such devices advance by the invention and innovation of production techniques. Additionally, there has been increased demand for flexible versions of such MEMS devices. Thin film patterning, represents a key technology for the realization of such flexible electronics. Patterns and methods that can be directly written into the thin film allow for design modification on the fly with the need for harsh chemicals and long etching steps. Laser-induced dewetting has the potential to create patterns in thin films at both the microscopic and nanoscopic level without wasting deposited material. This thesis presents the first demonstration of high-speed direct-write patterning of metallic thin films that uses a laser-induced dewetting phenomenon to prevent material loss. The ability to build film material with this technique is explored using various scanning geometries. Finally, demonstrations of direct-write dewetting of a variety of thin films will be presented with special consideration for high melting point metals deposited upon polymer substrates.

Dedication

I would like to dedicate this thesis to my parents, Jesus and Martha Ferrer for their support during all the stressful moments of my education. They have always pushed me to do my best and ensured that I was raised in an environment that fostered the very best learning. I would like to thank my brother, for always helping me find perspective and offering different outlooks on life. Finally, I would also like to dedicate this thesis to my wife, Alison Mac. I would not have been able to complete this work had I not had someone to consistently offer their love and understanding as we start our life a new together.

Acknowledgments

I would like to express a great deal of gratitude towards my Ph.D. advisor, Prof. Glenn Amatucci, for his nearly six and a half years of guidance. From my years working as an undergraduate worker through my time within the graduate program, I have come to understand that he always expected the best work and in return he has always displayed an incredible amount of dedication to his students and staff. Because of him and my experience at the ESRG, I have grown as both a researcher and as a person.

I would like to thank my thesis committee members, Prof. Lisa Klein, Prof. John Matthewson, and Prof. Stephen Tse for their dedication to their students and for their participation in helping me achieve my goals.

I would also like to thank all the staff members of the ESRG, Ms. Irene Plitz, Ms. Linda Sung, Mr. John Gural, Mr. Barry Vanning, Ms. Fadwa Badway, Ms. Anna Halajko, and Dr. Nathalie Pereira, who have helped me in my work and who have made my time at the ESRG enjoyable. Finally I must express my gratitude towards my fellow graduate students present and past, Dr. Andrew Gmitter, Dr. William Yourey, Dr. Matthew Parkinson, Dr. Kimberley Scott, Dr. Jonathan Ko, Josh Kim, and Nick Faenza. Your camaraderie and discussions have been essential to my work and my time within the graduate school.

All work in Chapter 3 was originally published as “Micro-patterning of Metallic Film Structures through Direct-Write Dewetting,” A. J. Ferrer, A. Halajko, and G. G. Amatucci. *Advanced Engineering Materials.* 2014, 16: 1167-1178. doi: 10.1002/adem.201400240 A. Halajko contributed thin films created with chemical vapor deposition, thermal evaporation, and sputter deposition techniques.

The work in Chapter 4 has yet to be submitted for publication as of March, 2015. A. Halajko contributed thin films created with chemical vapor deposition, thermal evaporation, and sputter deposition techniques.

Table of Contents

List of Figures

List of Tables

1 Introduction

1.1 Motivation

The advent of the microelectromechanical system (MEMS) has enabled the miniaturization and mobilization of a number of technologies in recent history. The most prominent and oldest applications for MEMS consist of accelerometers[1], gyroscopes[2], inkjet heads[3], and pressure sensors[4]. Each of these categories boast a market size valued over $1 billion and accounted for nearly 60% of the $8.9 billion MEMS market in 2010. In addition, to these highly commercialized devices, a number of MEMS technologies are poised to make large leaps in growth in the coming years. Examples include micro displays[5], micro oscillators[6], and especially microfluidics[7-9]. While most current microfluidics devices are created for niche applications, their market volume is projected to increase drastically as designs become more robust and more devices are produced for research purposes in a variety of fields combined with commercial purposes such as *in-vitro* diagnostics for the medical and chemical fields. **Table 1.1** lists several MEMS categories along with established commercial or emerging applications that are likely to see increased activity in the near future.

All of these miniaturization efforts were initially made possible through micromachining and patterning methods first used in integrated circuit (IC) technology, but adapted for the creation of the 2.5D and 3D mechanical structures characteristic of MEMS technology. The first batch-fabricated MEMS devices appeared in the mid to late 60's and used a combination of electroplating and photolithography.[10] Traditional IC manufacturing techniques, however, cannot overcome all of the design requirements dictated by the higher amounts of geometric variation and applications of the final MEMS

products. There is no equivalent “Moore’s Law” for MEMS devices since there is no standard, universal process, such as CMOS manufacturing, nor is there a single functional structure, e.g. the p-n junction, on which to focus development upon. Furthermore, where IC technology strives to continuously increase the amount of transistors that can fit onto a particular area/volume with the goal of added computing power, MEMS devices do not have a unified manufacturing goal that will benefit all end-users. There is a limit to the usefulness of additional micro-sensors and actuators on a single commercial device if the existing sensors built into it already succeed in their purpose. Therefore, size reduction does not necessarily represent the major developmental goal in this field.

Instead, current MEMS technology progresses through the advent and optimization of new micromachining/patterning techniques.[11] New manufacturing techniques will give MEMS designers greater freedom in their architecture and increased device throughput while keeping costs down. Such cost reduction is essential for fabrication companies seeking to make a profit, as there is an enormous price pressure on the commercial MEMS units. Additionally, there is a growing desire in the MEMS market to move towards a “fabless” structure, where the burden of fabrication is shifted from the hardware and design companies and placed upon specialized fabrication outfits for mass production.[12] Thus, now more than ever, it is crucial that new scalable fabrication processes are explored and characterized.

In this respect, new 2.5D and 3D microfabrication techniques for both IC and MEMS devices have proven to be a rapidly growing area of research and development. Such techniques provide increased freedom and optimization of device design. Unfortunately, much like their 2D counterparts, 3D patterning will often require the removal of unwanted material, which ultimate raises front-end costs. Alternatively, additive processes must sacrifice manufacturing throughput in order to obtain the high resolutions needed to

construct features at the micro-scale. The work detailed in this thesis seeks to expand the options available to the researchers and process engineers who seek to pattern thin films onto flexible substrates for use in the MEMS and microfluidics industries.

Table 1.1: Market valuation and projections for MEMS devices.

MEMS Category	**2010 Market** [Millions US $]	**2017 Market** [Millions US $] **(Projected)**	**Commercial & Emerging Applications**	**Ref**
Accelerometers	$1,411	$1,564	-automotive electronic stability control	13
			-platform stability	13
			-automotive impact detection	13
Pressure Sensors	$1,355	$2,240	-mass air pressure sensor	14
			-intraocular pressure	15
Ink Jet	$1,567	$1,939	-commercial ink printer head control	3
Gyroscopes	$1,006	$1,468	-automotive rollover detection	16
			-navigation (in combination with accelerometers)	16
Optical MEMS	$965	$2,555	-micro-grating array	5
			-micro-mirror array	5
Microfluidics	$1,154	$4,794	-"lab on chip" medical diagnostics	7
			-biomedical research	8
			-micro fuel cells	17
Oscillators	$12	$463	-frequency control	18
			-surface acoustic wave sensors	19
Micro Displays	$ -	$261	-face mask HUD	20
			-flexible displays	21
RF MEMS	$359	$1,028	-micro switches for Radar	22
			-tunable capacitors	23
Uncooled IR	$303	$652	-military FLIR cameras	24
Miscellaneous	$198	$991	-piezoelectric energy harvester	25

1.2 Literature Review on Thin Film Patterning

To deal with the diverse nature of MEMS, the methods for fabricating and patterning their foundational thin-films have continuously evolved towards the improved performance and production beyond those of integrated circuits. Still, the foundation upon which all MEMS technology is based rests on the original silicon processing techniques used for IC. The following is a literature review on micro-fabrication techniques used to pattern thin films for use in IC and MEMS devices beginning with older techniques, such as masked deposition of thin films and proceeding to more advanced, experimental techniques.

1.2.1 Masked Deposition

Masked deposition represents one of the oldest and simplest forms of patterning thin-films. Also known as stencil lithography, this *in-situ* process relies on the precise and accurate creation of stencil masks to block out deposition of a thin-film in a specific pattern. Masks are most often used in conjunction with physical vapor deposition (PVD) techniques such as sputter deposition or evaporation deposition – techniques in which the trajectory of the depositing particles can be described as "line of sight" from the source to the target.[26] **Figure 1.1** diagrams a typical PVD source and target apparatus with a mask in place for patterning. The spacing of the apparatus components dictate the final profile of the deposited features and represent an area of great importance for the technique. Sopori and Chang (1977) investigated the edge profile of deposited microscale features using a mask and sputter deposition combination.[27] Theoretical and experimental studies described a discontinuity in the tapered profile of deposited

material that proved dependent upon the thickness of the mask itself. In 1979, Yao developed analytical and computational models to predict the profile of mask-patterned features for the purpose of constructing mesoscale (~300 μm) thin-film Luneberg lenses.[28] This group demonstrated that careful construction of the mask could enable user-defined deposition profiles and proceeded to create lenses of a pre-determined thickness and taper.

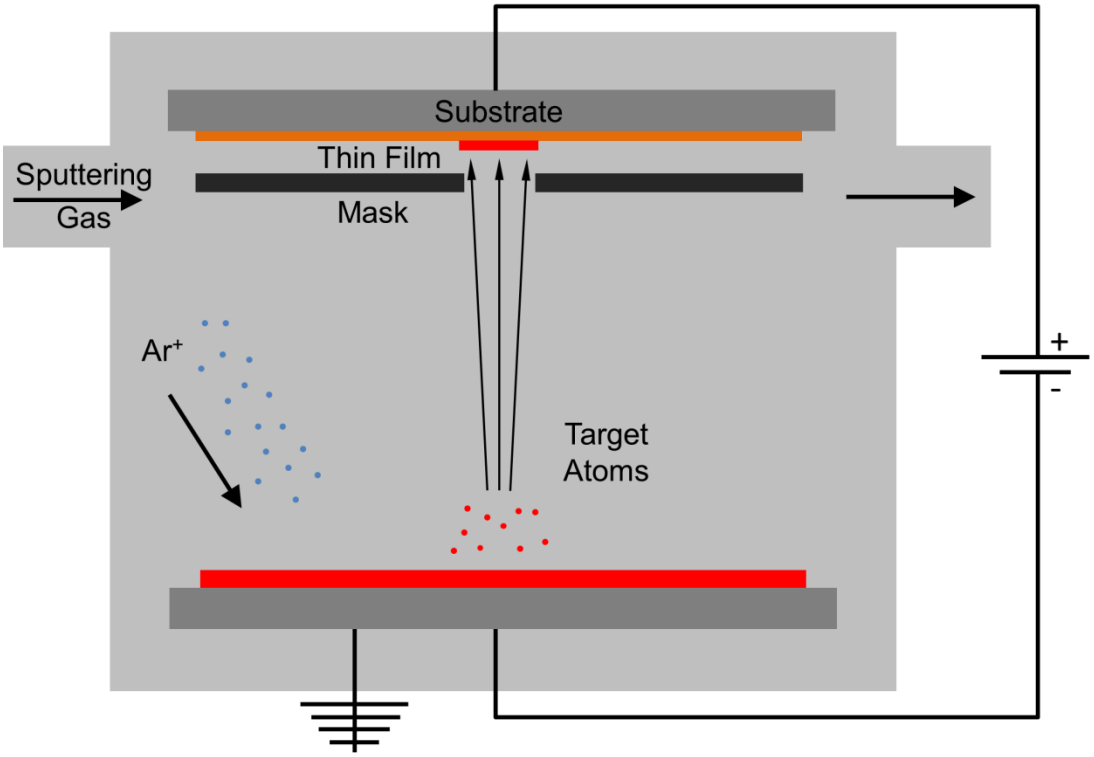

Figure 1.1: Diagram of a sputtering deposition.

More recent examples include work in which silicon micro-machining techniques are used to create a shadow mask to enable *in-situ* patterning of electrode materials with features down in the 100's of microns.[29] **Figure 1.2** details some examples of possible patterns created using the shadow mask system. The latest masks are capable of producing features down to 20 nm in size using patterned gold thin films (**Figure 1.3**) for the purpose of biosensing.[30]

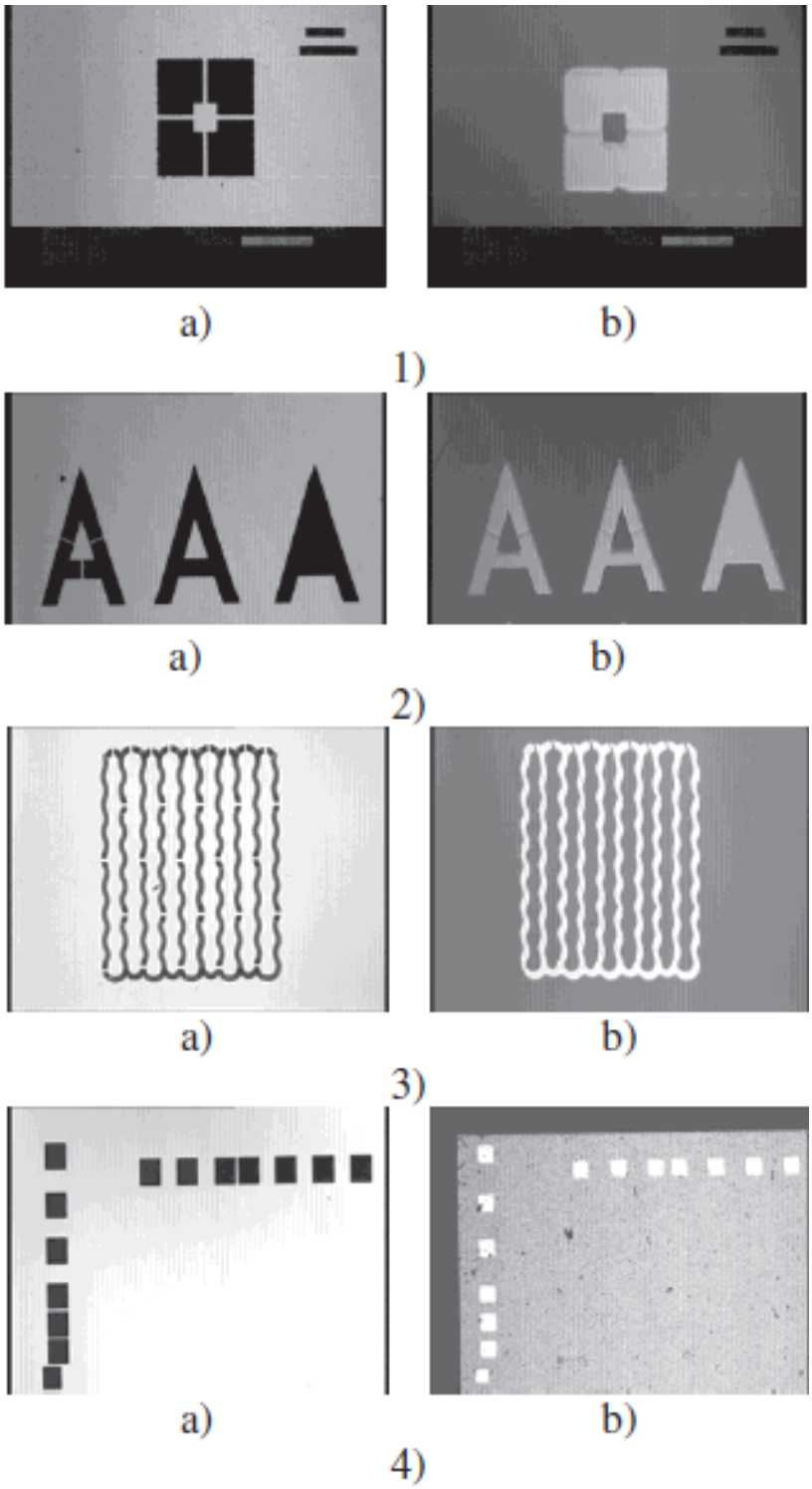

Figure 1.2: Visual association between the etched patterns of a shadow mask (a) and the resulting deposition through the mask (b). The geometries attempted consist of: (1) a square (height = 320 μm); (2) letters (height = 50 μm); (3) a spring (height = 1000 μm); (4) an IC with square contacts of 100 μm × 100 μm.[29]

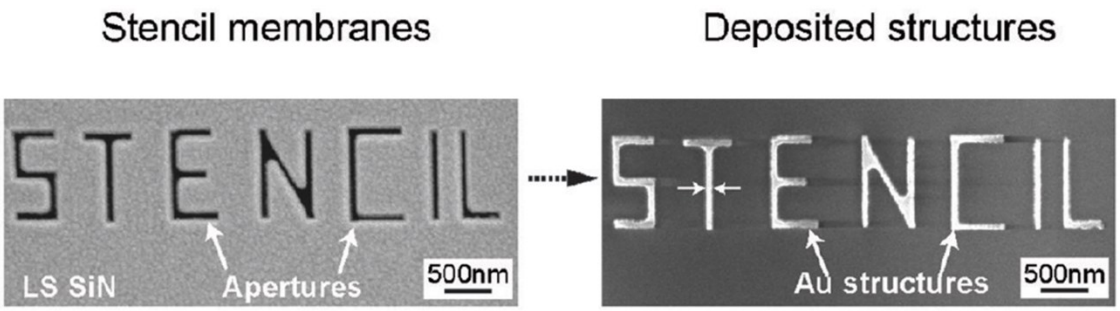

Figure 1.3: The word "STENCIL" created out of Au deposited onto SU-8 photoresist. Adapted with permission from Vazquez-Mena et. al. Copyright 2012 American Chemical Society. [30]

1.2.2 Photolithography

Photolithography represents the most commercially successful thin-film patterning methods to date. Nearly all IC devices are currently created using some form of photolithography. As such, the technology is very well developed; however, there are more advanced versions in development and on the verge of more widespread adoption that may offer improved resolution and throughput. A total of six basic steps comprise traditional photolithographic processes: thin film deposition, photoresist preparation, masked exposure, post-bake/development, etching, and removal of the photoresist (**Figure 1.4**).

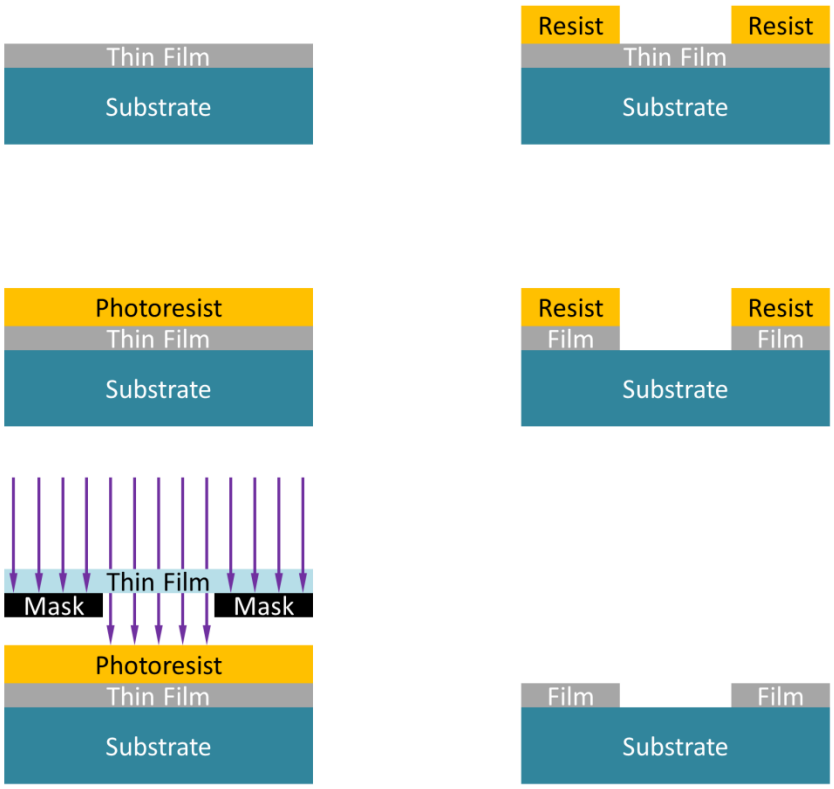

Figure 1.4: The basic steps of lithography for the patterning of thin films.

The entire process relies upon properties of photo-sensitive polymers that enable a change in solubility upon exposure to radiation. Originally, photolithographic processes relied on filtering of mercury arc lamp radiation and exposure of the photoresist through masked features of 1:1 proportionality. Modern photolithographic regimes use a modified optical-step process that takes chromium masks and uses a series of lenses to project the mask's image onto the photoresist at a reduced size. In this way, the limit to feature size and depth of field are described by the Rayleigh diffraction limit as described by **Equation 1** & **2**, where k_1 is a dimensionless constant based on the imaging system, λ is the wavelength of the radiation in the medium, θ_0 is the half angle aperture of the

lens, and NA_0 = $\sin\theta_0$. All features are restricted by the wavelength of the radiation used.

$$R = k_1 * \lambda / \sin\theta_0 \quad (\mathbf{1})$$

$$DOF \propto \lambda / NA_0^2 \quad (\mathbf{2})$$

There are ways, however, to decrease the effective minimum resolution of the lithography process – some of which are already being used in the IC and MEMS industry. Such methods include the implementation of immersion lithography, two-photon polymerization, x-ray lithography, extreme ultraviolet lithography (EUVL), multiple exposure processes, and combinations of two or more of these. Rather than using particles with shorter wavelengths (such as in x-ray, extreme UV, or electron lithography) immersion lithography increases the index of refraction of the medium through which the exposure occurs – thus lowering the effective wavelength of the radiating particle as described by **Equation 3**, where λ_0 is the wavelength of the particle in a vacuum and n is the index of refraction through the medium.

$$\lambda = \lambda_0 / n \quad (\mathbf{3})$$

In 2001, Switkes and Rothschild demonstrated the technique using a modified interference lithography system with a 157 nm exposure source and a system index of refraction of n = 1.37 to give an effective wavelength of 115 nm.[31] Linear features with a pitch length of 60 nm were created in a thin layer of photoresist (**Figure 1.5**). The authors explored several perfluoropolyether (PFPE) liquids as the index matching immersion fluid and noted that this was a relatively simple and easy modification since

the source and optical components need not be changed from their original “dry” configuration. By extension, more complex, optical-step lithography systems would need only slightly more complicated modification in order to implement the technique. Immersion lithography has seen successful use in combination with 193 nm sources for use in 55 and 45 nm IC devices[32]. Most current instances of this technique use an aqueous immersion fluid that can reduce the effective wavelength down from 193 nm to 134 nm.[33] Thus, smaller features may be created than what would be possible with a “dry” system using 157 nm sources.

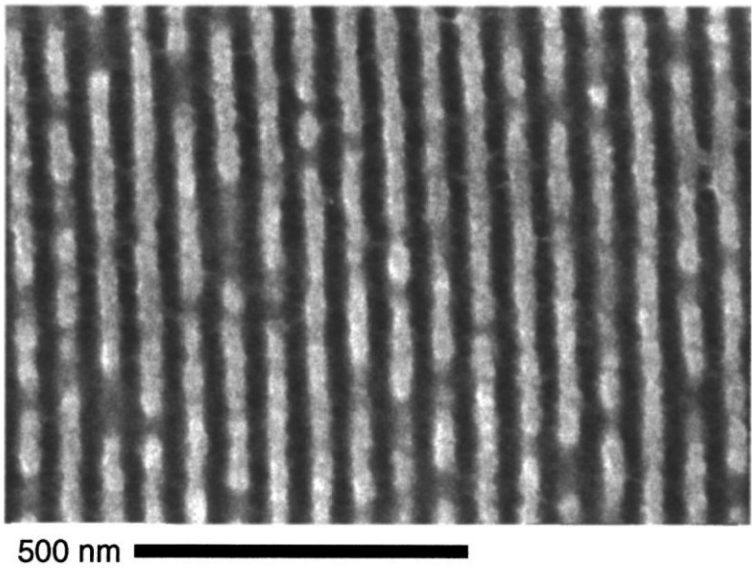

Figure 1.5: Photoresist features created using 157 nm immersion photolithography with 60 μm line-to-line spacing. Reprinted with permission from Switkes and Rothschild. Copyright 2001, American Vacuum Society.[31]

Of course, if a source with a much smaller wavelength can be used in conjunction with immersion fluid processes, smaller features may be achieved. To this end, extreme ultraviolet lithography is being developed as a possible successor to immersion lithography at the 16 nm node of CMOS development. Tin, xenon, and lithium have been investigated as possible for sources for EUVL due to their similar excitation

energies at 13.5 nm.[34] These sources may be divided into two separate categories: discharge produced plasma and laser produced plasma. An industry goal of 3% conversion efficiency from input laser/discharge power to in-band EUV output was set in 2005. Therefore, choice of source composition along with increasing the power output of the exposure system is crucial to the implementation of the technology. For high volume manufacturing, Sn source targets have emerged as the most promising targets. There are still difficulties creating clean and effective photoresist patterns. All of the optical elements in EUVL systems must be comprised of Mo/Si Bragg-reflectors. As a result, speckle is introduced into the pattern as a result of the surface roughness of the mask.[35] However, some groups have made progress. In 2012, a 22 nm device was demonstrated using a combination of 193 nm immersion lithography and EUVL.[36] In this device, two layers were printed using EUV lithography – one on top of the other. Examination showed good feature wall smoothness as well as reproducibility.

1.2.3 High Aspect Ratio Techniques

Modern MEMS devices use a wide variety of chemistries, such as ceramics, metals, polymers, etc… for which traditional IC manufacturing techniques are ill-suited or uneconomical. Additionally, MEMS may require aspect ratios or other geometries that are not necessary in IC devices. Thus, more complex and versatile methods of patterning are necessary for the realization of commercially viable and practical microsystems. Dry reactive ion etching was developed as an extension of radio frequency (RF) glow sputtering, which uses an RF current to create plasma arch and accelerate argon towards the desired target. By changing out the argon gas for a fluoride gas, the plasma will create reactive ions that can be used to etch hard-to-sputter

targets such as Si_3N_4, SiO_2, and silicon.[37] While initial etching rates measured on the order of 0.3 to 0.6 nm/min newer processing equipment and gases have allowed etching rates to reach rates on the order of 3 to 4 μm/min.[38] Such high rates have been used to create high aspect features for use in MEMS device creation.

It is important to note that DRIE requires some level of photolithography to create a etch mask out of the photoresist, but it avoids the use of wet etch techniques that can employ dangerous chemicals. The technique has also been used to create hierarchal surface patterns for the purpose of modifying hydrophobicity.[39] By creating features at both the micro and nanoscale, the researchers were able to achieve apparent contact angles of 158° with minimal contact angle hysteresis.

LIGA (LIthographie Galvanoformung Abformung) processes refer to a series of steps combining deep X-ray or UV lithography with electroplating and mechanical forming. By using deep X-ray exposure from a synchrotron source, features with aspect ratios on the order of 100:1 can be patterned into a chosen resist (typically PMMA). Because of the collimated nature of synchrotron radiation in addition to the high energy photons, the surface walls of the resist features typically exhibit a high degree of verticality. Following this variation of lithography, metal is electroformed onto the surface, which can be used as a final product or as a mold for the production of high-quality injection-molded structures.[40] With additional lithography and etching steps, 3D structures can be formed with precise moving parts. Unless extreme aspect ratios are needed, UV sources can be used to provide a lower cost option that still follows the basic LIGA process. In this way, come of the costly Such UV-LIGA patterning techniques use SU-8 photoresist to create the templates for further electroforming and injection molding. It has been recently used as the basis for creating MEMS gyroscopes[41] and low cost micro-channels for heat exchange.[42] A modified UV-LIGA protocol has also been used to create a

template for hot embossing micro-features into a prototype light guide plate used in the construction of the LCD screens that are common in contemporary display technology.[43]

1.2.4 Direct-Write Techniques

Direct write techniques represent a pathway to free-form patterning of thin films and micromachining of bulk structures. There are two main categories for direct-write techniques: mechanical and directed energy. At the micro-scale, mechanical energy is often carried out using atomic-force microscopes (AFM) due to their ability to carefully modulate and monitor the forces placed on a surface. This “dip pen" technique relies on the tendency of AFM tips to promote condensation of water near the tip to surface interface. By pre-coating the tip with the desired molecules, patterns on the nanometer scale are achievable. **Figure 1.6** provides a diagram of the process. The first demonstration of this technique made use of 1-octadecanethiol to create 30 nm lines along the surface of an Au thin film.[44] Patterning was carried out in 34% humidity and took a total of 5 minutes. It was also shown that relative humidity played a key role in the deposition rate and resolution of the deposited features, where an increase to 42% relative humidity was able to generate 100 nm lines in 1.5 minutes.

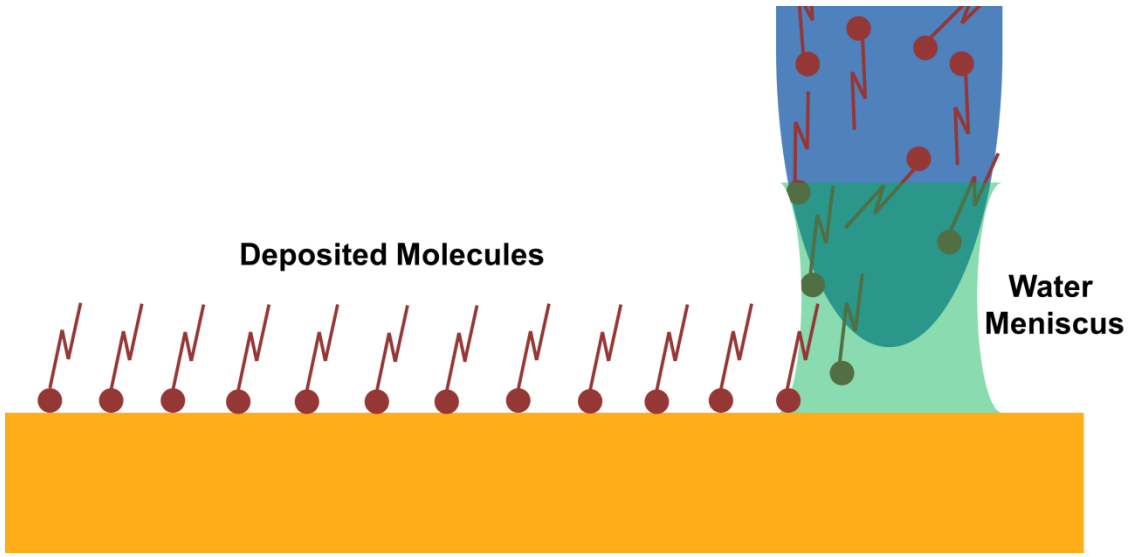

Figure 1.6: Diagram of dip-pen lithography.

Other groups have expanded the technique to pattern oxides[45] and metals.[46] Processing time remains the major drawback to this technique. By using arrays of the cantilever "dip pens" production time can be cut down significantly. It has been shown that arrays of 55,000 separate cantilever tips are effective at patterning a variety of molecules onto dot-arrays with nanometer precision. One square centimeter of area was patterned with over 88 million individual features.[47] Three-dimensional patterning is also possible; however, the array of cantilevers must be scaled down, as individual control of each tip is necessary. Topographical representations of greyscale pictures have been demonstrated using an array of 18 individually controlled cantilever tips.[48] By using fewer tips, a greater amount of control may be exerted on each individual point. In this way, much more complex shapes may be created, such that 3D structures are possible.

Energy-based direct write methods for patterning thin films use a directed beam of laser energy to enact a morphological or chemical change to the local area of exposure. As with photolithography, the ultimate resolution of the system is dictated by the

wavelength of the incident radiation according to the Rayleigh diffraction limit. Therefore, micrometer resolution is possible with lasers operating in the near-infrared region (NIR) and nanometer resolution with laser operating in the visible to ultraviolet range. In some processes, lasers may be used to directly deposit material onto the desired substrates via physical or photochemical means. Laser-induced forward transfer (LIFT) processes have received a great deal of attention due to their ability to direct write metal thin film structures. The process uses short pulses of focused laser radiation to induce a breakdown at the target thin-film/substrate interface and subsequent "blasting" of the target film onto the acceptor substrate. An alternative mechanism is a result of the thermo-mechanical phenomena within the film induced by the laser radiation, where the thermal expansion of the film causes delamination, tearing, and eventually is expelled across the separation distance onto the acceptor substrate.[49] A number of different target films and substrates have been demonstrated using various metals as transfer targets with substrates consisting of ceramics and oxide glasses. These types of lines have also been used as seed layers for subsequent electroplating.[50] Aside from metals, the technique has been used by researchers to create transparent indium tin oxide (ITO) electrodes for use in transparent electronic devices. By focusing a frequency quadrupled (λ = 266 nm) Nd:YVO_4 laser under pulsed operation, onto a spin coated suspension of ITO particles, the researchers were able to create linear patterns of ITO measuring 850 nm high, 20 μm wide, and a line to line spacing of 30 μm.[51] Fluence, as measured in deposited energy per area, emerges as an effective way of characterizing the varying lasing parameters provided that the unit power per area is consistent. For the described LIFT patterning, fluences ranged from 10 mJ/cm^2 to 100 mJ/cm^2, with the most effective settings ranging between 20 mJ/cm^2 and 30 mJ/cm^2. After printing, the deposited ITO particles were consolidated using an excimer laser operating at a

wavelength of 248 nm with 30 ns pulses but without focusing. Fluence above 38 mJ/cm^2 sufficiently fused the particles such that conductivity rose drastically. The lack of focusing resulted in the amalgamation of the nanoparticles without the concentrated rapid heating in the LIFT protocol.

By increasing the intensity as well as the fluence, it is possible to completely ablate thin films in a type of negative space laser direct-write technique. In 1989, Ballentine et al. explored patterning of superconducting thin films using a pulsed Nd:YAG laser operating at a wavelength of 1064 nm and a pulse length of 120 picoseconds. In their work, patterns were ablated out of a 1.5 μm, Y-Ba-Cu-O film mounted on an X-Y, computer controlled motion stage.[52] With an average power of 10 mW and a spot size of approximately 10 μm, the pulse fluence during processing was calculated to be on the order of several J/cm^2. Complex patterns were demonstrated with ablated lines as thin as 6 μm. A micro-bridge was also created using the X-Y system measuring 200 μm wide and several millimeters long. The authors claim that the super conductivity of the film was unaffected. More recent work on laser ablation patterning has focused on applications in photovoltaic (PV) devices. In 2010, Bovatsek et al. studied the laser scribing parameters for use on a variety of PV materials, including molybdenum, SnO_2, amorphous silicon, and a multilayered film deposition.[53] Multiple lasers were tested for efficacy in scribing. Two wavelengths were investigated: 1064 nm and 534 nm. All lasers operated in a pulsed fashion with pulse lengths ranging from 6 to 70 nanoseconds. Images of the scribed lines are displayed in **Figure 1.7**. For the patterned lines, the authors made use of galvanometer mounted mirrors to scan the beam across the surface of the film, which would allow free-form patterning of the layers to suit any solar cell design. Threshold fluences of the SnO_2 and molybdenum were measured to be on the order of 1 J/cm^2. Threshold values for scribing the amorphous

silicon and the multilayered film stack were measured to be on the order of 0.1 J/cm^2, where there was a cited preference for shorter pulse duration and thus lower thermal loading on the targets. The scalloping of the edges is due to the overlap percentage of the pulses, which is controlled by the scan speed of the mirrors, as well as the frequency of the laser pulsing. For the features presented, scan speeds ranged between 0.5 m/s to 1.5 m/s, demonstrating that high-speed laser processing is viable for processing thing films for the purpose of micro-electronic systems.

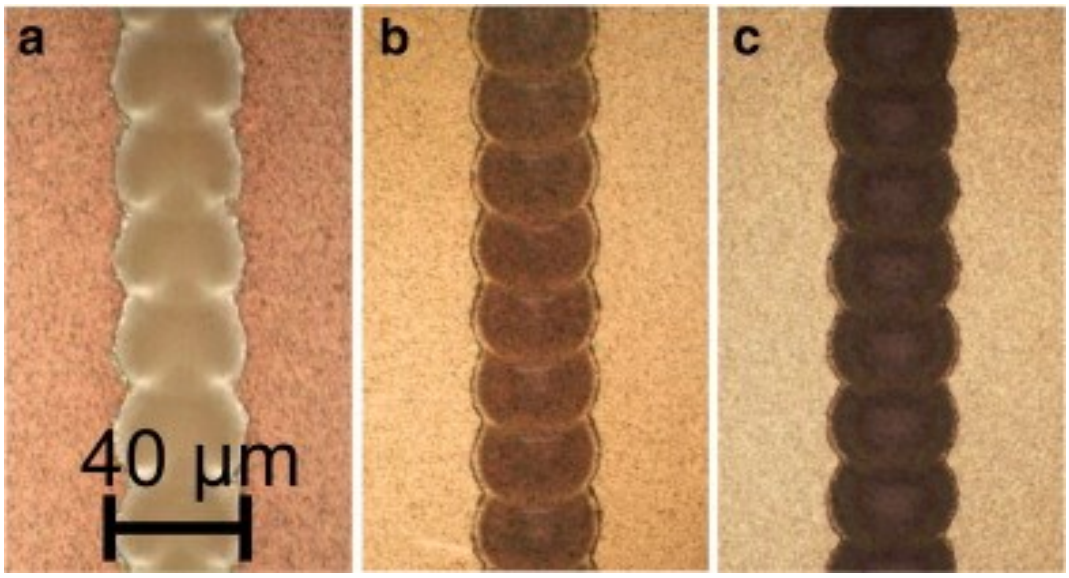

Figure 1.7: Example scribes of a) SnO_2, b) amorphous-Si, and c) a multi-layered film of Al/ZnO/amorphous-Si.[53]

In 2011, Heise et al. investigated the ablation of thin molybdenum films deposited on transparent glass substrates. Using a technique similar to the LIFT technique, the authors were able to create series of ablated lines in both a “direct” configuration where the beam impinges directly on the film and in an “indirect” configuration where the beam is passed through the transparent glass substrate before striking the Mo thin film.[54] It was found that while the direct, film-side exposure process required a fluence of 1.7

J/cm^2 but the threshold for indirect, substrate-side exposure was 0.11 J/cm^2. This highlighted a difference in the mechanism that causes film removal upon exposure dependent on the side of illumination. While direct exposure experiences complete thermodynamic heating, melting and evaporation, exposure through the substrate cause a non-thermodynamic event that is characterized by breakdown at the substrate film interface with subsequent delamination, cracking and disintegration. With the shift in modern consumer electronics towards developing cheap, flexible, and polymer based devices, it is important to demonstrate the viability of using a laser to pattern thin films on flexible substrates. Using a similar mechanism as the through-substrate indirect ablation, some researchers have demonstrated patterning of thin copper-indium-gallium-diselenide (CIGS) films that were deposited on polyimide (PI) substrates.[55] Instead of relying on the transparency of the substrate to allow exposure of the film-substrate interface, the group chose a laser wavelength (248 nm) that would actually induce a small amount of ablation of the substrate itself. The trials were conducted on a multi-layered set of films consisting of a 2.2 μm thick CIGS film deposited on 1 μm of molybdenum deposited upon a 25 μm thick polyimide substrate. Using a 25 ns pulsed excimer laser and an X-Y-Z moveable stage, the authors created linear patterns to demonstrate the efficacy of their technique.

According to the researchers, when the ablation event is initiated at the surface of the PI substrate, shock waves are created that travel perpendicular through the plane of the polymer to strike the target CIGS film where delamination and ultimately cracking and destruction occur. In this manner, the group was able to create lines measuring approximately 73 μm wide using three pulses per point, each with a fluence of 8.6 J/cm^2 – significantly higher than other laser processing regimes. The benefit seen from this

method stems from the thermal insulation afforded by the substrate and the lack of laser generated heat on the target film itself.

1.3 Laser Dewetting

1.3.1 Undirected Laser-Induced Dewetting

There exists a small window of processing parameters where laser modification of thin films does not result in traditional or mechanical ablation of the target film, but rather, induces a localized melting effect that enables forces of surface tension to cause dewetting of the film from the substrate. In this regard, the minimum amount of material is removed while creating structures of varying height and width within the thin film. Even though, some control over the geometry of the features is relinquished dewetting of metastable thin films presents as an interesting way to generate micro patterns without wasting precious film material. The mechanism behind laser induced dewetting of thin films – specifically metallic ones – was first investigated by Bischof et al. in 1996.[56] The films explored, consisted of Au, Cu, and Ni deposited upon fused-silica substrates. Dewetting was induced by illumination of the films via a frequency-doubled (λ = 532 nm) Nd:YAG laser operating in a Q-switched mode with pulse durations of 7 ns. Spatial distribution of the beam intensity closely matched a TEM_{00} profile. A perfect TEM_{00} intensity distribution will take on a Gaussian spatial profile. True beams can approach a Gaussian profile, but as beam power increases, so does the deviation from the ideal intensity profile. In this initial work, the beam underwent mild focusing down to a spot diameter of ~1 mm. As described by the authors, the dewetting of the 25 nm to 50 nm

films presented two different distributions of hole-diameter. For the larger, 5 μm holes, the authors observed small nucleation points at the center of the dewetting region, thus confirming the nucleation and growth mode of dewetting. Alternatively, smaller, 2 μm holes exhibited a characteristic length scale, but the centralized defects or hillocks representative of the nucleation and growth of holes were not observed. As described by previous work on liquid polymer systems, these smaller holes originated from surface perturbations whose amplitudes increased via capillary flow.[57-60] This mode of hole formation and film retraction was termed "spinodal dewetting," since the dynamics and appearance of the morphology was analogous to the spinodal decomposition phase separation that is found in certain binary solid systems. The dewetting mechanisms of thin films were further explored in 1998 by Xie et al., whose group used polystyrene on silicon substrates to demonstrate that films thicker than 100 nm tend to dewet via nucleation and growth of holes, while films thinner than 100 nm will tend to dewet via the spinodal decomposition-like change. Spinodal dewetting was again utilized to create nano-patterns on ultra-thin (1 to 8 nm thick) cobalt films.[61-64] The authors demonstrated the use of unfocused UV (λ = 266 nm) laser exposure while in a vacuum atmosphere to observe and characterized the undirected re-ordering of the film. Beam spot area was cited as 3 x 3 mm^2. By varying the number of pulses irradiating a single area, the authors were able to note the effects of an increasing cumulative fluence. As in earlier work done on polymer films, the metal films progress from a series of connected voids to a series of isolated drops with a specific characteristic wavelength that is dependent on initial film thickness.[58] This characteristic wavelength is described by **Equation 4**, where *d* is the thickness of the film and α is a constant related to the film/substrate combination.

$$\lambda = 2\pi * \sqrt{2/3} * d^2/\alpha \quad (4)$$

The spinodal dewetting nature of ultra-thin silver films as deposited on SiO_2 substrates was investigated by Krishna *et al* in 2010 and used, in large part, the same protocol as was described for the ultra-thin Co films.[65] Once again, it was shown how the characteristic length may be tailored by controlling the initial thickness of the deposited film. It was also shown that above a certain thickness (> 11.5 nm) discrete holes begin to form at the outset of dewetting rather than the characteristic "bicontinuous" morphology seen in other spinodal films. Finally, spinodal dewetting was demonstrated on ultra-thin nickel films where a 12 ns pulse of unfocused laser radiation resulted in metallic liquid lifetimes on the order of 25 ns.[66]

1.3.2 Pre-patterned directed laser dewetting

By pre-patterning the film, some researchers have essentially constrained the flow of the dewetting, molten metal so as to create structures of a variety of shapes. Rack *et al* demonstrated this technique using electron beam lithography to pattern PMMA substrates that were then coated in a 30 nm Ni film.[67] In addition to surface tension forces, the authors attribute some of the retraction to the change in density experienced by the mass of irradiated nickel. A more specific manner of patterning took advantage of the observed Rayleigh-Plateau instability that is observed in ribbons of dewetting film by pre-patterning specific edge profiles, into the deposited films.[68,69] Rayleigh-Plateau instability describes the tendency of a column of liquid to break up into individual drops over time as a result of infinitesimal varicose perturbations of the column's surface. The growth rates of the perturbations are a function of wavelength, however, for patterned

edge ribbons, dominating wavelength is set at a pre-determined spacing and distribution. Examples of these may be seen in **Figure 1.8**.

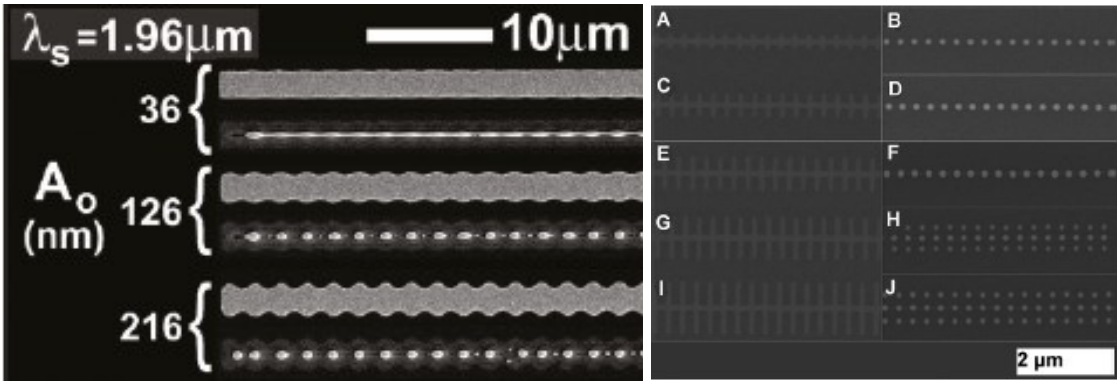

Figure 1.8: Manually defined instability wavelength using pre-patterned films. Adapted with permission from Fowlkes et al. Copyright 2011 American Chemical Society.[68] Adapted with permission from Roberts et al. Copyright 2013 American Chemical Society.[69]

1.3.3 Beam shape and interference patterning

Aside from pre-patterning the target film, some researchers have investigated shaping the beam itself as a means of directing dewetting. In a technique analogous to projection lithography, Kuznetsov, Koch, and Chichkov demonstrated the patterning of a 60 nm gold film using masked laser radiation and fluences on the order of 0.2 J/cm^2.[70] The authors employed a series of masks in the beam line of the 800 nm laser to block out only the desired areas of intensity. By taking this masked laser radiation and de-magnifying it down 100x, a variety of shapes were achieved – from basic shapes such as circles, to complex shapes such as letters. The authors also demonstrated that Au films tend to initially flow toward the center of the exposure, which was explained via a combination of thermal swelling and fluid flow down a composition gradient formed from impurities. Rather than using a mask, it has also been shown that interference is a

viable route for the patterning of thin films a number of different chemistries.[71,72] In this respect, it was shown that a set of two or three interfering beams will create periodic intensity patterns. When using a 10 ns pulsed, frequency-doubled (λ = 532 nm) Nd:YAG, exposure resulted in the formation of "bumps" in areas of relatively high intensity before eventually rupturing to make voids in the surface of the film. It was shown that these bumps are hollow on the inside; thus, they are formed through thermal expansion and delamination rather than melting. Certain chemistries, such as Si, Ge, or Bi films did not exhibit this bumping, which may be due to density changes that occur during melting combined with incredibly high quench rates. With fluences ranging from 100 mJ/cm^2 to 300 mJ/cm^2, feature resolution was on the order of 1 to 2 μm.

1.3.4 Focused beam dewetting

Dewetting has also been investigated using tightly focused radiation to induce thermocapillary flow and moving the beam relative and target relative to one another. Willis *et al* investigated the thermocapillary flow of chromium films under focused near-infrared laser radiation. The authors found that the movement of the molten surface was nearly entirely characterized by the surface tension effects created by the temperature gradient at the exposure site.[73] This type of localized thermocapillary dewetting has, thus far, been used to create direct-write structures in thin polystyrene films when deposited on silicon substrates.[74] It was demonstrated that there was minimal to no loss of polymer during the dewetting process. Linear features of varying line-to-line distances were realized using an X-Y computerized stage. The technique also took advantage of the differing absorption properties of the polymer/substrate interface. The authors provide evidence to the fact that the polymer acts as an anti-reflectivity layer, where

areas of exposed substrate no longer produce as much heat since the impingent laser radiation is transmitted to a higher degree. This ability to direct-write thin films using a dewetting mechanism rather than traditional scribing opens up new possibilities for creating micro-scale and nano-scale features without wasting time on masking or destroying large amounts of film. Before further investigation and improvement of this basic technique, a better understanding of the relevant forces and phenomena is warranted.

1.4 Wetting and Dewetting

1.4.1 Surface Energy and Tension

Surface energy refers to the work required to cleave a new surface or interface out of the bulk mass of material. Surface tension is one component of this energy. Its origins stem from the inherent imbalance of forces found at such surfaces and interfaces. **Figure 1.9** diagrams the general discrepancy in the force balance between molecules in the bulk of a material and molecules at a surface or interface. Within the bulk, the intermolecular bonds (ionic, covalent, or metallic) and forces (van der Waals, hydrogen bonding, etc…) that surround a single molecule are on average in equilibrium. At a surface, the lack of molecules in one direction induces a virtual force along the surface of the material. For interfaces, the mismatch of molecule arrangement manifests as an interfacial tension similar to surface tension.

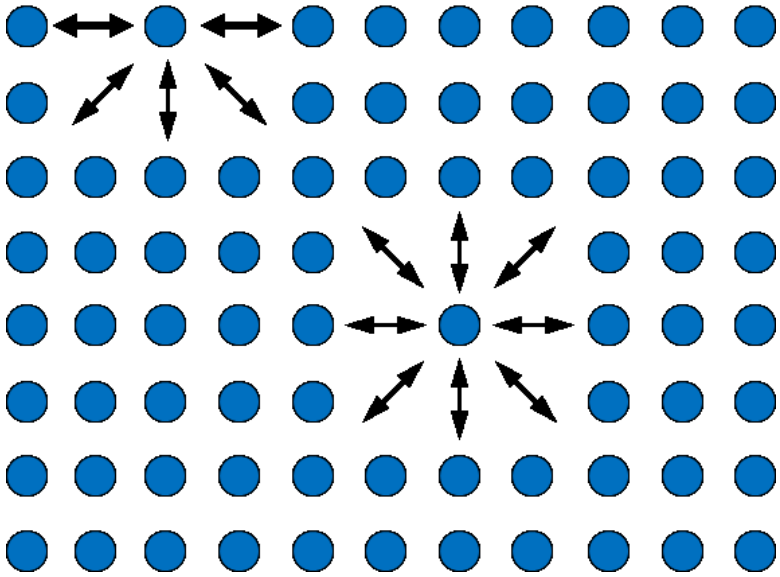

Figure 1.9: General diagram of the bond and intermolecular forces found at the surface and in the bulk.

1.4.2 General Surface Energy Trends

Because the surface tension is a result of a mismatch in the bonding state of molecules located at an interface, certain trends in surface energy may be observed that depend on the type of material in question. For example, materials such as organic polymers have chains of monomers connected by covalent bonds; however, these chains are themselves, held together in the bulk by forces such as van der Waals interactions and hydrogen bonding. Such materials will typically exhibit low surface energies on the order of 50 mJ/m^2. **Table 1.2** details the critical surface tension, as determined by Zisman theory, of a few common polymers.[75] The Zisman method of determining contact angle assumes that the surface energy of a solid substrate is equal to the highest surface tension that a liquid drop can exhibit while still completely wetting the solid.[76] This surface tension is termed the "critical surface tension." Generally, this

method only works for solids that do not exhibit a polar component in the surface energy due to a lack of polar molecules or branches. Thus, most non-polar polymers are very easily characterized using this method. It is also important to take into account the temperature at which surface energy is calculated/measured, since an increase in temperature is characterized by a weakening of the bonds within the bulk of a material. The mismatch between the bonding energies of the bulk and those at the interface are reduced, thus a decrease in the surface energy of the material is observed. **Table 1.3** provides a list of preferred values for the surface tensions of a variety of metals at their melting point. Tyson and Miller extrapolated, from grain boundary interfacial tension measurements, the ratio between the solid-vapor and liquid-vapor surface energies.[77] With this, they were able to calculate that at the melting point, the solid-vapor surface energy is approximately 1.18 times larger than the liquid-vapor surface tension. They assumed this relationship for all the elements, but noted that a more realistic scenario would see deviation from this relationship in non-metallic elements. For metals, however, the relationship is assumed valid.

Additionally, the magnitude of the molar solid-vapor surface energy is roughly proportional to the heat of sublimation at the material's melting point.[78] While the authors expressed a certain amount of uncertainty in the values, a generally positive trend is observed. As expected, the metals with the largest heats of sublimation, tungsten and tantalum, also exhibit the highest surface energies and are more refractory in nature. Low melting point metals, such as tin, exhibit a low heat of sublimation and therefore have relatively low surface energies compared to the other metals.

Table 1.2: List of polymer films and corresponding critical surface tension.[75]

Polymer Film	**Critical Surface Tension** [mJ/m^2]
Polyethylene terephthalate	43.0
1, 4-cyclohexylene dimethylene terephthalate	43.0
Polyvinylidene chloride	40.0
Polyvinyl chloride	40.0
Polyvinyl alcohol	37.0
Polystyrene	33.0
Polyvinyl fluoride	28.0
Polytetrafluoroethylene	18.5

Table 1.3: Solid and liquid surface energies at the melting points of selected metallic elements.[77]

	Metal	Calculated Solid/Vapor Surface Energy @ T_m [mJ/m^2]	Liquid/Vapor Surface Tension @ T_m [mJ/m^2]
Ag,	Silver	1086	920
Al,	Aluminum	1020	864
Au,	Gold	1333	1130
Be,	Beryllium	1298	1100
Bi,	Bismuth	446	378
Co,	Cobalt	2218	1880
Cr,	Chromium	2006	1700
Cu,	Copper	1566	1327
Fe (δ),	Iron	2123	1799
Ga,	Gallium	845	716
Hg,	Mercury	580	490
Mo,	Molybdenum	2510	2127
Nb,	Niobium	2313	1960
Ni,	Nickel	2080	1763
Pd,	Palladium	1743	1477
Pt,	Platinum	2203	1867
Sn,	Tin	661	560
Ta,	Tantalum	2493	2113
Ti,	Titanium	1749	1482
V,	Vanadium	2301	1950
W,	Tungsten	2765	2343
Zn,	Zinc	896	759

1.4.3 Sessile Drop

The surface tensions of materials in the liquid operate on the same basic principle as solids: there is a mismatch or lack of bond at the interface compared to the bulk. Liquids, however, may have a free-deformable surface, meaning that when a liquid drop is placed upon a solid, the liquid may change shape depending on thermodynamic balance of energies in the system. In this sessile drop configuration, there exists a triple point, where solid substrate, liquid drop, and ambient gas all meet as seen in **Figure 1.10**. It is this junction, where all three materials meet, that matters most. There are three interfaces which must be accounted for: the liquid-solid interface, the solid-vapor interface, and the liquid-vapor interface. **Equation 5** (Young's Equation) gives the relationship for the three surface energies at the triple point under thermal equilibrium conditions, where γ_{Lv}, γ_{SL}, and γ_{Sv}, are the liquid-vapor, solid-liquid, and solid-vapor interfaces respectively.[79]

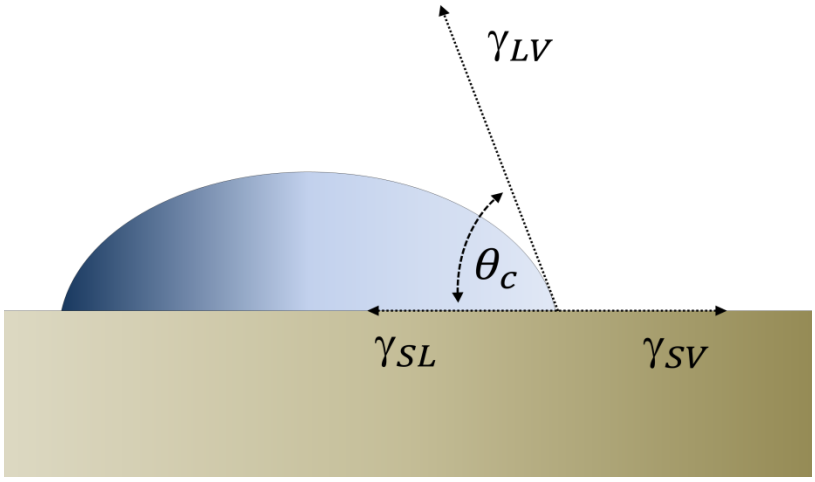

Figure 1.10: Diagram of triple point for sessile drop configuration.

$$\gamma_{SL} + \gamma_{LV} \cos \theta_c = \gamma_{SV} \quad (\mathbf{5})$$

Depending on the balances of these forces, the resulting morphology of the deposited sessile drop may be termed “completely wetting,” “partially wetting,” or “non-wetting.” To determine which of these configurations is thermodynamically favorable, it is useful to consider the spreading coefficient, S_{eq}, which takes the difference between the solid substrate’s surface energy and the combined surface energies of the other two interfaces (**Equation 6**). For $S_{eq} < 0$, the drop will take on a partial wetting shape with a contact angle between 0° and 180°. Largely negative spreading coefficients will exhibit very large contact angles. Conversely, for $S_{eq} \geq 0$, the equilibrium angle becomes zero and the liquid will tend to completely wet the solid once equilibrium is reached.

$$S_{eq} = \gamma_{SV} - (\gamma_{SL} + \gamma_{LV}) \quad (\mathbf{6})$$

1.4.4 Free Energy of Wetting

The stability of thin films on a solid surface depends on a variety of factors; surface tensions, intermolecular forces, and initial film thickness comprise the major influences for metallic films. For systems whose spreading coefficient is positive, i.e. the completely wetting regime, films of any thickness are stable. Systems within the partial wetting regime can be metastable or unstable when below a critical thickness as explained by **Equation 7**, where γ_{LV} is the liquid’s surface energy, ρ is the density of the liquid, and *g* is the acceleration due to gravity.[80] Under this thickness, a dewetting event may take place.

$$h_c = 2\sqrt{\gamma_{LV}/\rho g}\sin\theta_c/2 \quad (7)$$

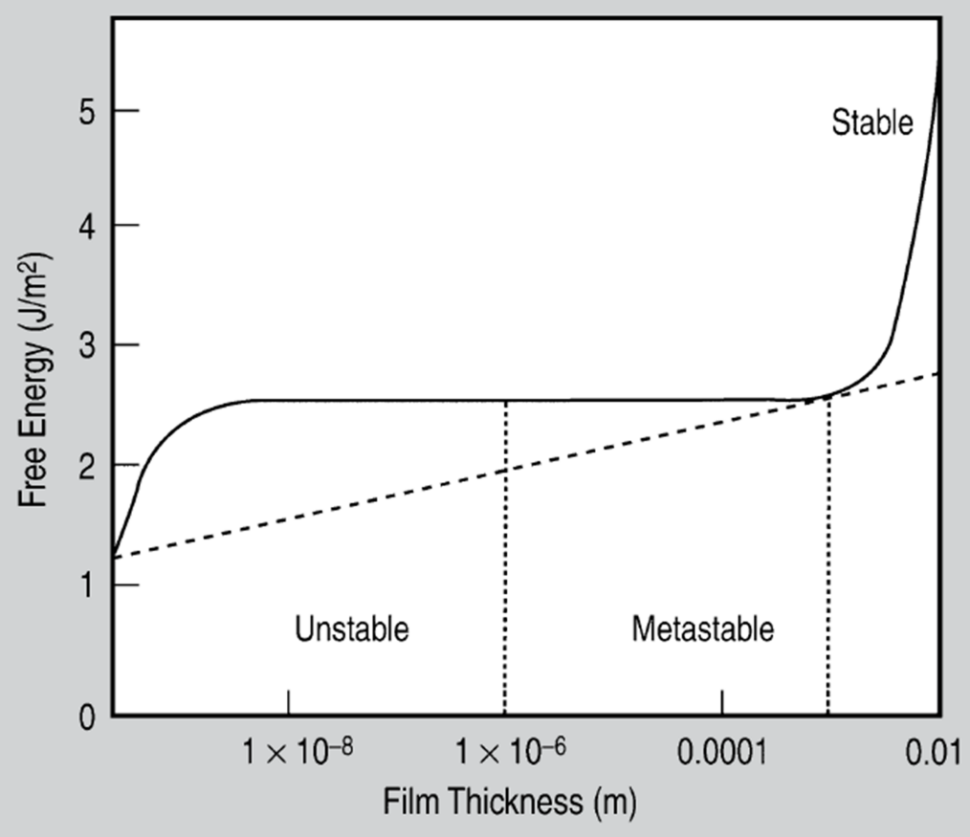

Figure 1.11: Free energy curve of a metal thin film versus thickness.[63]

For liquid metals, the typical thickness at which stability occurs is 1 mm. Below this, the film will be metastable or unstable. **Figure 1.11** provides a typical free energy curve for a film of metal versus thickness. For all heights, the change in free energy between wetting and non-wetting can be conceptualized as the difference between the existence of a film with height, h, versus film with height = 0. **Equation 8** describes this change in free energy, which takes into account the gravitational, intermolecular, and surface tension forces. In particular, the equation describes the free energy change of a wetting film – switching the sign would describe a dewetting condition.

$$\Delta F(h) = F(h) - F(0) \; = \; F_{Ext} + F_{Int} + F_{Surf} = \frac{1}{2}\rho g h^2 + \frac{A}{12\pi h^2} - S_{eq} \quad (\mathbf{8})$$

1.4.5 Morphological Effects on Wetting

When speaking of the contact angle of a liquid drop resting on a solid substrate, it is often understood that the system is at its thermodynamic equilibrium and that the solid is perfectly flat. Actual surfaces will have a quantifiable roughness that affects the apparent contact angle (θ_a) of a sessile drop. This is important for the engineering of surface with specific contact angles with respect to liquids such as water. In a 1936 paper, Wenzel describes the effect of roughness as a factor that increases the interfacial tension between the drop and the substrate.[81] **Equation 9** models the added factor to the triple point in the system. In this scenario, the drop will make contact with both the ridges and valleys of a rough surface, as diagramed in **Figure 1.12a**. This model, however, does not explain the effect of rough surfaces in which the liquid does not enter the grooves of the roughened material. Cassie and Baxtor developed a different model as diagramed in **Figure 1.12b**. For surfaces of this type, the composition of the surface can be thought of heterogeneous, where two different materials are present with two different equilibrium contact angles.[82] In this case, the weighted summation of the cosines of the different equilibrium angles equal the cosine of the apparent contact angle as shown in **Equation 10**. Superhydrophobic surfaces can be created when the 2nd component of the surface is air and the fraction percentage of the 1st component is small. Such surfaces exhibit a number of interesting characteristics, including self-cleaning properties. This is a commonly found in nature where the most notable instance is that of the lotus leaf, hence the popular term “lotus effect”. In 2003, Marmur developed a set of criteria to describe the transition between the Wenzel state

(homogenous wetting) and the Cassie-Baxtor state (heterogeneous wetting).[83] This criteria depends on the curvature of the free-energy curve of wetting, which for rough surfaces, is governed by the geometry and size of the peaks and valleys of the solid. A separate, but related phenomenon may be termed the "petal effect," which features a hierarchal morphology of long wavelength features that allow liquid contact, in addition to short wavelength ridges at the peaks that prevent full adhesion to the leaf.[84]

$$\cos\theta_a = r\cos\theta_c \quad (9)$$

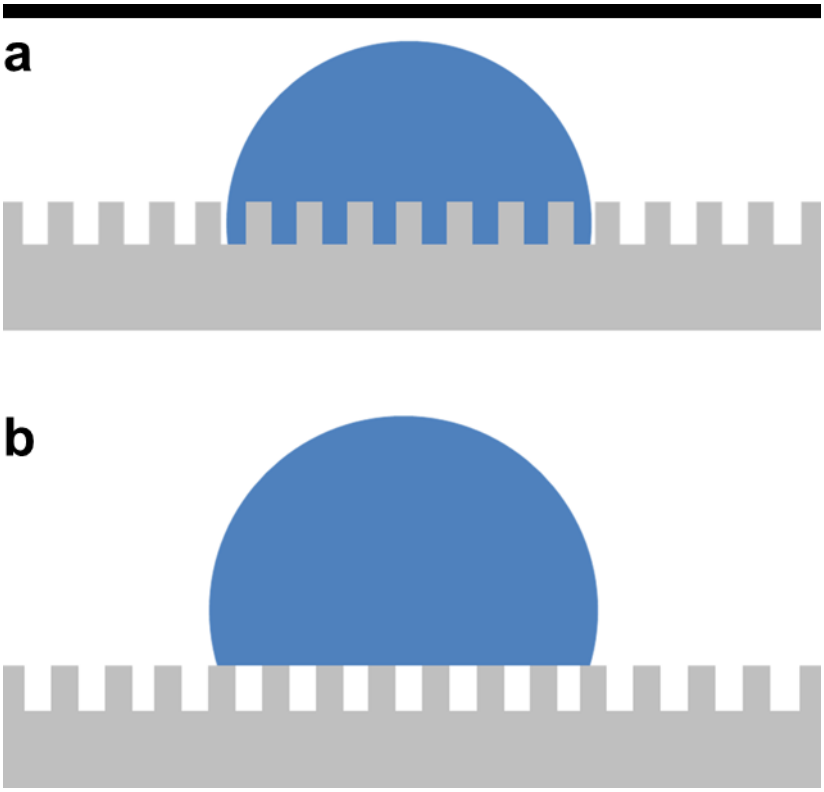

Figure 1.12: a) Wenzel wetting state, b) Cassie-Baxtor wetting state

$$\cos\theta_a = f_1\cos\theta_1 + f_2\cos\theta_2 \quad (10)$$

1.4.6 Electrowetting

The presence of an electric potential between the liquid and the solid substrate can modify the electrical condition of a surface and induce charging as well as other effects such as double layer capacitance. When this happens, the interfacial tension, and thus the contact angle, between the liquid and solid can be modified. The first demonstrations of this technique occurred in 1981 as a means to create a display whose opacity could be controlled via a change in voltage.[85] The authors were careful to differentiate between electrowetting and the similar technique of electrocapillarity. Where electrocapillarity looks to overcome the surface tension of a conducting liquid by imposing a voltage between it and an adjacent electrolyte solution, electrowetting will impose a voltage between the conducting liquid and the substrate. Electrowetting will often require much lower voltage potentials, which can be useful for a number of applications. Beyond displays, electrowetting has been investigated as a possible method for micro-actuation, namely a micropump.[86] The limitations of this technique with respect to decreasing the contact angle of water on hydrophobic polymers were investigated by Vallet, Vallade, and Berge. It was found that past a certain point, charge saturation occurs and large amounts of degradation will occur at the triple point of the surface tension system.[87] More recent progress has found many uses of electrowetting in the microfluidics field, where small potentials may allow manipulation of liquids at the micro-scale and has proven to be a viable method of system control for lab-on-chip applications.[88,89]

1.5 Laser/Material Interaction

1.5.1 Reflection, Transmission, Absorption

A material's interaction with electromagnetic (EM) radiation is essential to assessing its viability for laser processing. A solution to the wave equation describing the propagation of EM radiation along the Z-axis through a material can be seen in **Equation 11**, where A_0 is the amplitude, *n* is the index of refraction, *k* is the extinction coefficient, ω is the angular frequency, and *c* is the speed of light through a vacuum. The index of refraction and absorption coefficient may be calculated from the real and imaginary parts of the dielectric permittivity, ε_1 and ε_2 respectively (**Equation 12 and 13**).[90]

$$E(z,t) = A_0 e^{-i(\omega/c)kz} e^{(\omega/c)nz} e^{-i\omega t} \quad (11)$$

$$n^2 = (\varepsilon_1 + \sqrt{\varepsilon_1^2 + \varepsilon_2^2})/2 \quad (12)$$

$$k^2 = (-\varepsilon_1 + \sqrt{\varepsilon_1^2 + \varepsilon_2^2})/2 \quad (13)$$

With these materials constants, one can calculate the theoretical optical properties of a material. There are three basic interactions that can take place when speaking of material/EM radiation events: reflection, transmission, and absorption. For any material, the sum of the reflectivity, transmissivity, and absorptivity coefficients must equal unity as detailed in **Figure 1.13**.

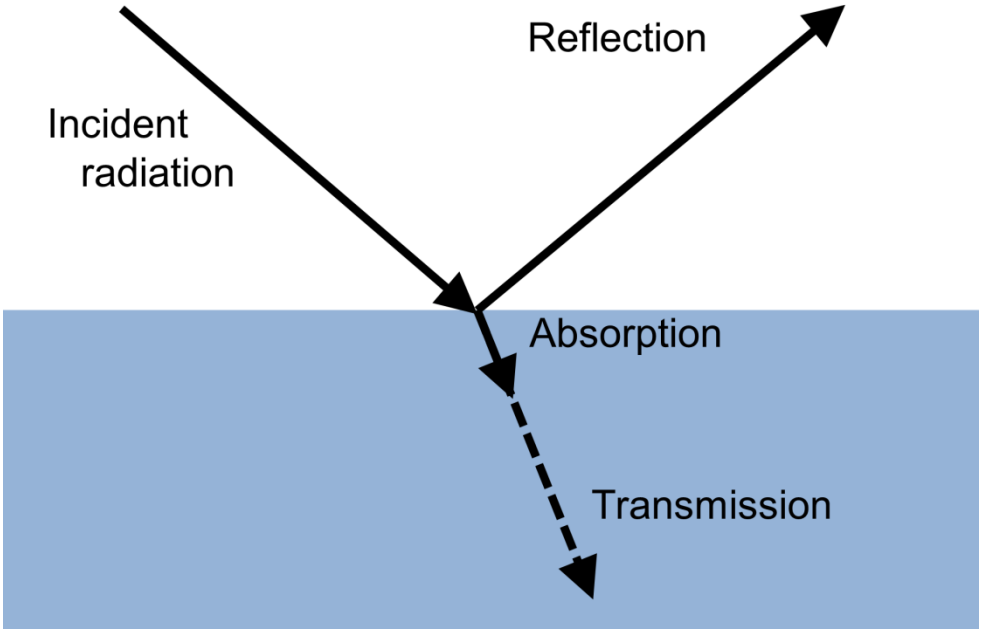

Figure 1.13: Diagram of reflection, absorption, and transmission.

Metallic materials exhibit very shallow penetration depths for EM radiation below the mid-UV range, with few exceptions. This depth is defined by the inverse of the absorption coefficient, α, that is found in the Beer Lambert law (**Equation 14**).[91]

$$I(z) = I_0 e^{-\alpha z} \quad (14)$$

This is due to the delocalization of electrons in a metal's structure. Typical values for the penetration depth of a metallic material are on the order of 50 nm, at which point the intensity of the beam has reached 1/e of the original value of the impinging beam. Such shallow optical depths imply that metal films above ~100 nm in thickness do now allow any transmission through the thickness. Thus, we may neglect transmissivity coefficient and set absorptivity coefficient equal to 1 minus the reflectivity coefficient. In doing so,

we may calculate the theoretical values of the absorptivity coefficient (A) at normal incidence solely using *n* and *k* values (**Equation 15**).

$$A(\theta = 0) = 4n/((n+1)^2 + k^2) \quad (\mathbf{15})$$

By using light at normal incidence, polarization does not affect absorption; however, both the index of refraction and absorption coefficient depend upon the wavelength of light. The oscillation of an incoming EM wave will drive a complementary oscillation in the dipole moment of an irradiated metallic atom. Lorentz modeled this as a simple, driven harmonic oscillator with damping effects caused by collision of the electrons with other electrons, phonons, and lattice imperfections. Thus, changes in the wavelength will affect the resulting speed of the EM radiation which then defines the index of refraction. **Figure 1.14** presents a graph detailing the varying theoretical absorptivity of a number of metals calculated from their optical constants.[92] Photon energies corresponding to common laser wavelengths (1064 nm, 532 nm, 266 nm, etc.) were chosen for calculation. Where the optical constants were not available, the complex dielectric constant was used to calculate the absorptivity. Note that the data presented for absorptivity does not depict the true spectra of the metals, but instead, provides a general trend between the calculated absorptivity points.

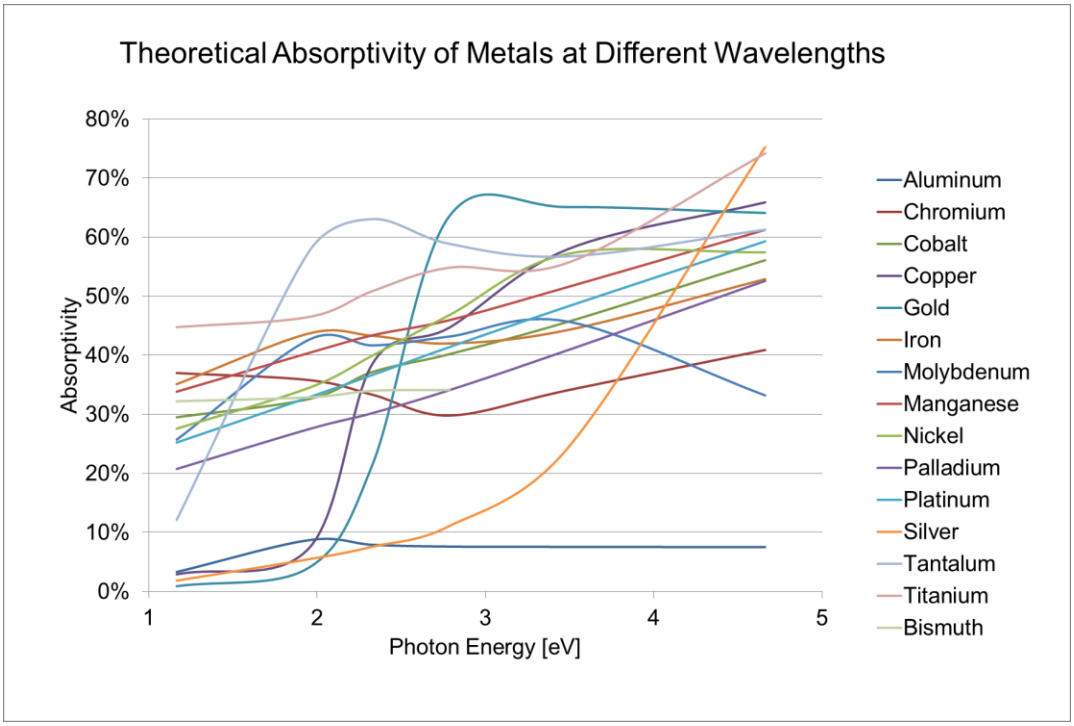

Figure 1.14: Theoretical absorptivity of various metals as calculated from n and k

1.5.2 Absorption and Heating

As stated before, the EM wave of a propagating light, such as from a laser, interacts with the electron structure of the illuminated material. For insulators and semiconductors, this usually means that an incoming photon must have enough energy to excite an electron into another energy band, such as the conduction band.[91] In the case of metallic materials, the delocalization of electrons allows for a larger range of energy photons to undergo absorption. The mechanism for their absorption is often a collision such as inverse-bremsstrahlung absorption where the momentum of an electron is shifted by the absorption of an incoming photon.[91,93] After this absorption, the excited electron may re-emit a photon or the energy may be transferred through to the lattice phonons. In the former case, the radiation is perceived to be reflected, while in the latter

case, collisions with phonons or lattice imperfections will generate heat and a rise in temperature within the material.

Whether or not a collision will take place, is dependent upon the plasma frequency, ω_p, of the metal (**Equation 16**).

$$\omega_p = \sqrt{N_e e^2 / m_e \varepsilon_0} \quad (\mathbf{16})$$

This plasma frequency is a function of the electron density, N_e, the mass of the electron, m_e, and the permittivity of free space, ε_0. When $\omega < \omega_p$, absorption and reflection dominate the behavior of the light/metal interaction. However, when the incident radiation has a $\omega > \omega_p$, transmission dominates the interaction. For most metals, this transition occurs in the mid-UV region. Once absorption and heat generation occurs, it is conducted through the material according to the heat equation, which describes the relationship between the time derivative of the temperature and the spatial distribution of the temperature field. **Equation 17** presents a version of the heat equation for a coordinate system fixed relative to the laser beam, where ρ is the density of the material, c_p is is the specific heat at constant pressure, v_s is the velocity of the substrate, and Q is the total amount of energy in the system.[91]

$$\rho(x,T)c_p(x,T)\frac{\partial T(x,t)}{\partial t} - \nabla[\kappa(x,T)\nabla T(x,t)] + \rho(x,T)c_p(x,T)v_s\nabla T(x,t) = Q(x,t) \quad (\mathbf{17})$$

From the equation, we can see that the thermal conductivity of the material will dictate how heat is distributed within the bulk of the material and therefore higher values of the thermal conductivity will allow quicker dissipation of concentrated areas of heat. For laser processing, this means that metals with high thermal conductivities will require higher input laser power for the same inherent absorptivity. **Table 1.4** lists the thermal conductivities of a number of metals along with their melting points for reference.[94] Copper, silver, gold, and aluminum are the most difficult to process using near-infrared radiation since these metals are highly reflective at that wavelength in addition to having high thermal conductivities. In most cases, heat is conducted away quickly and so little laser energy is absorbed in the first place that these metals do not experience sufficient rise in temperature to allow effective laser processing. There are external parameters that may have effects upon the absolute absorption of a particular film. These can include surface roughness, oxide layers, and impurities at the surface of the metal.

Table 1.4: Melting points and thermal conductivities of selected metals.[94]

	Metal	Melting Point [°C]	Thermal Conductivity @ 300K [W/(m·K)]
Ag,	Silver	962	429
Al,	Aluminum	660	237
Au,	Gold	1064	317
Bi,	Bismuth	271	7.97
Cr,	Chromium	1907	93.7
Cu,	Copper	1085	401
Fe (δ),	Iron	1538	80.2
Ni,	Nickel	1455	90.7
Pt,	Platinum	1768	71.6
Sn,	Tin	232	66.6
Ti,	Titanium	1668	21.9
W,	Tungsten	3422	174

1.5.3 Pulsing Effect

A benefit of using lasers to process metals lies in the variability of exposure regimens that the user may define. In general, lasers function in one of two different operating modes: continuous wave and pulsed mode. For applications at the micro-scale it is often beneficial to carefully modulate the energy incident on the work piece by pulsing the laser. According to the heat equation, any generated heat from laser exposure must be dissipated into the rest of the work piece or into the surrounding environment. Thus, pulsed beam operation takes advantage of this heat dissipation by activating the laser

with specific pulse durations, then allowing the piece to cool between pulses. The frequency with which the laser fires depends upon the type of laser being used, however typical values range from 1 Hz to 100 kHz. For a pulsed laser traveling in a particular direction, the heat will build up in overlapping sections. **Figures 1.15** and **1.16** display the temperature profiles generated out of simulation experiments conducted by Kalyon and Yilbas.[95] The authors ran a number of different tests that recreated the effects of different pulse lengths and thermal relaxation times. It was shown that there is a slow rise in average temperature from pulse to pulse. Additionally, the effects of two back-to-back pulses do not raise the temperature to the same degree as a single pulse of double the intensity. These simulations also highlight the value in creating computational models as a way to reduce optimization times for laser heating processes.

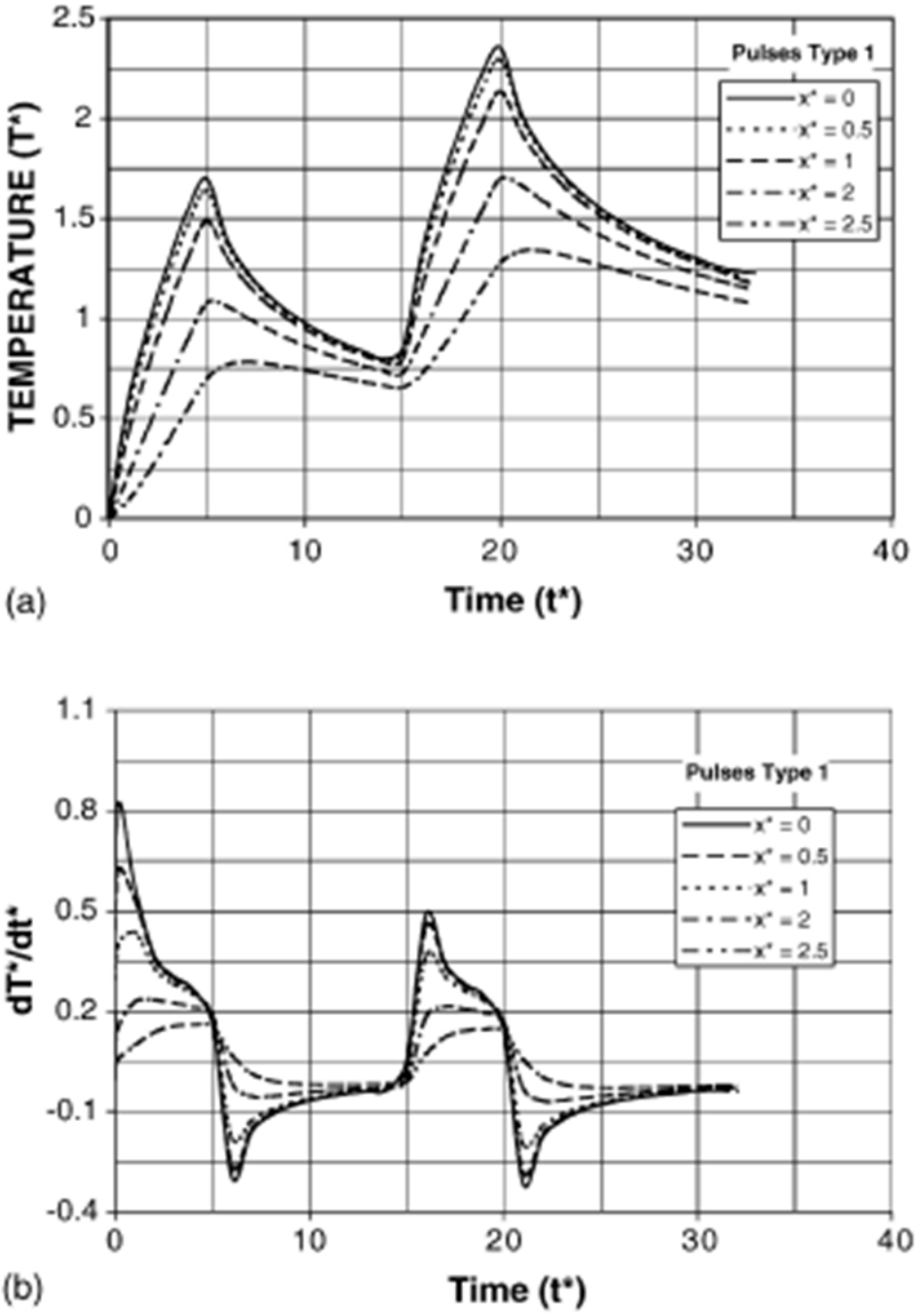

Figure 1.15: a) Dimension-less temperature contours of two pulses with pulse to relaxation ratios of 5 to 10 at different distances from the center of the beam. b) Contours of the time derivative of the calculated dimension-less temperature taken at different x-axis distances from the center. The pulse number indicates a particular pulsing regime chosen by the authors. Copyright 2006, with permission from Elsevier.[95]

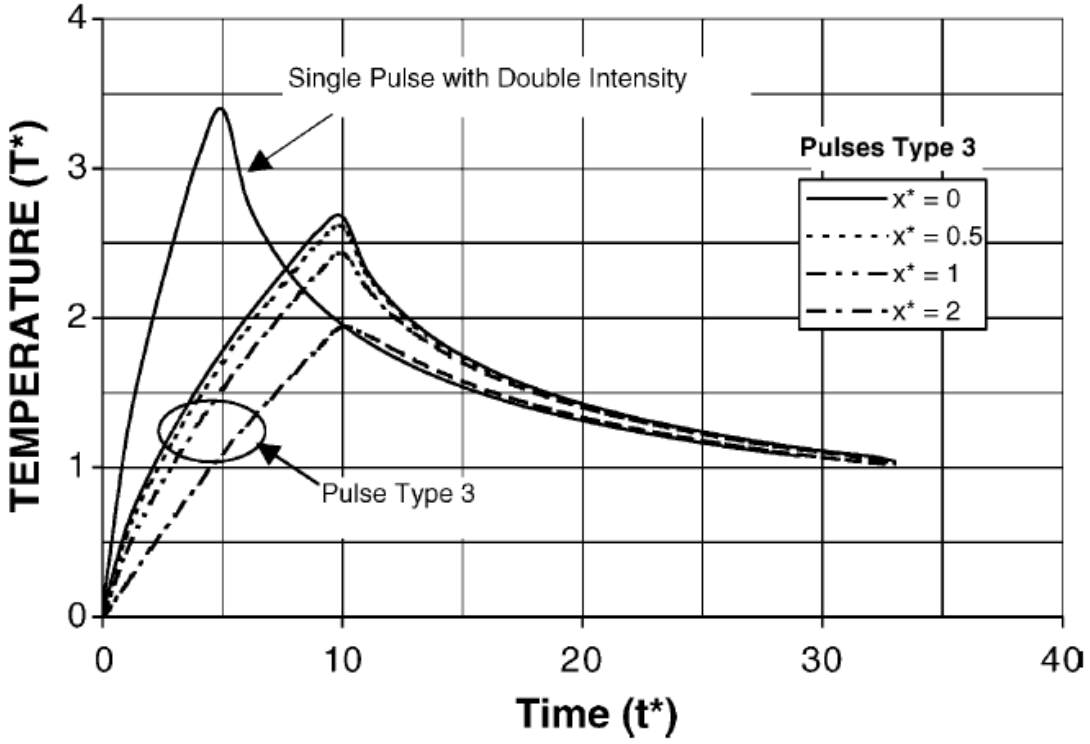

Figure 1.16: Dimension-less temperature contours versus a dimension-less time parameter of two pulses. Contours are shown for various x-axis distances from the center of the irradiated area. Also shown, is a single pulse at double intensity, which highlights the relative effects of intensity versus pulse duration. The pulse number indicates a particular pulsing regime chosen by the authors. Copyright 2006, with permission from Elsevier.[95]

1.5.4 Marangoni Flow

During laser processing, a thermal gradient forms within the metal with a peak at the center of the laser spot that decreases in magnitude as you measure at increasing radii. For lasers operating in a TEM_{00} single-mode fashion will have an enhanced gradient due to the Gaussian spatial distribution of the beam. After melting has taken place, thermocapillary movement will occur due to this thermal gradient as described by the Marangoni Effect. The source of this thermocapillary flow is the dependence of surface tension on temperature, where a material at higher temperatures will exhibit lower

surface tension. Therefore, at the outer edges of the gradient, there is a larger tension pulling fluid away from the center of the exposure area as described by **Equation 18**, where $\vec{\tau}$ is the surface tension tensor, $\nabla\gamma$ is the surface tension gradient, and ∇T is the temperature gradient.[74]

$$\vec{\tau}\cdot\hat{n} = \nabla\gamma = \frac{d\gamma}{dT}\nabla T \quad (\mathbf{18})$$

1.6 Thesis Structure

In light of work done in the field of laser-induced dewetting, it is clear that there is room for improvement as well as the introduction of new variations on the technique. The following thesis will hold the following structure. First, the various methods and equipment used in this work will be explored, with some general background theory as well as the specific models used. Reports on the successful direct-write dewetting of low-temperature metallic thin films on polymer substrates will be presented. The versatility and limitations of the technique will be examined. Success in the use of high melting point and high reflectivity metallic thin films in conjunction with this technique will be demonstrated. Finally, some conclusions from this work will be discussed, along with suggestions for future avenues of research.

1.7 References

1. Wang L, Wolf Jr. RA, Wang Y, et al. Design, fabrication, and measurement of high-sensitivity piezoelectric microelectromechanical systems accelerometers. *Journal of Microelectromechanical Systems*. 2003;12(4):433-439.
2. Maenaka K, Ioku S, Sawai N, Fujita T, Takayama Y. Design, fabrication, and operation of MEMS gimbal gyroscope. *Sensors and Actuators A: Physical*. 2005;A121(1):6-15.
3. Kim B, Kim S, Lee J, Shin S, Kim S. Dynamic characteristics of a piezoelectric driven inkjet printhead fabricated using MEMS technology. *Sens Actuators A Phys*. 2012;173:244-253.
4. Eaton WP, Smith JH. Micromachined pressure sensors: Review and recent developments. *Smart Mater Struct*. 1997;6(5):530-539.
5. Ma J. Advanced MEMS-based technologies and displays. *Displays*. 2014;In Press. doi: 10.1016/j.displa.2014.10.003.
6. Reichenbach RB, Zalalutdinov M, Parpia JM, Craighead HG. RF MEMS oscillator with integrated resistive transduction. *IEEE Electron Device Lett*. 2006;27(10):805-807.
7. Chin CD, Linder V, Sia SK. Commercialization of microfluidic point-of-care diagnostic devices. *Lab on a Chip*. 2012;12:2118-2134. doi: 10.1039/c2lc21204h.
8. Sackmann EK, Fulton AL, Beebe DJ. The present and future role of microfluidics in biomedical research. *Nature*. 2014;507(7491):181-189. http://www.nature.com/doifinder/10.1038/nature13118. doi: 10.1038/nature13118.
9. Nawaz AA, Mao X, Stratton ZS, Huang TJ. Unconventional microfluidics: Expanding the discipline. *Lab on a Chip*. 2013;13:1457-1463. doi: 10.1039/c3lc90023a.
10. Nathanson HC, Newell WE, Wickstrom RA, Davis Jr. JR. The resonant GateTransistor. *IEEE Transactions on Electron Devices*. 1967;14(3):133.
11. Mounier E. Future of MEMS: Market and technologies perspective. . 2014.
12. Eloy JC, Mounier E. Status of the MEMS industry. *MEMS/MOEMS Components and Their Applications II. ed.* 2004;5717. doi: 10.1117/12.594011.
13. Yazdi N, Ayazi F, Najafi K. Micromachined inertial sensors. *Proceedings of the IEEE*. 1998;86(8):1640-1659. http://ieeexplore.ieee.org/xpls/abs_all.jsp?arnumber=704269&tag=1. doi: 10.1109/5.704269.
14. Löfdahl L, Gad-el-Hak M. MEMS-based pressure and shear stress sensors for turbulent flows. *Measurement Science and Technology*. 1999;10(8):665-686. http://stacks.iop.org/0957-0233/10/i=8/a=302?key=crossref.24abba97d0e9755b523324ae694f2746. doi: 10.1088/0957-0233/10/8/302.
15. Chen P-, Rodger DC, Meng E, Humayun MS, Tai Y-. Implantable unpowered parylene MEMS intraocular pressure sensor. *2006 International Conference on Microtechnologies in Medicine and Biology*. May 2006:259. doi: 10.1109/MMB.2006.251543.
16. Neul R, Gomez U, Kehr K, et al. Micromachined angular rate sensors for automotive applications. *IEEE Sens J*. 2007;7(1-2):302-309.
17. Lifton VA, Simon S, Holmqvist J, Ebefors T, Jansson D, Svedin N. Design and fabrication of addressable microfluidic energy storage MEMS device. *Journal of Microelectromechanical Systems*. 2012;21(6):1401. http://ieeexplore.ieee.org/xpls/abs_all.jsp?arnumber=6256676. doi: 10.1109/JMEMS.2012.2208218.

18. Lam CS. A review of the recent development of MEMS and crystal oscillators and their impacts on the frequency control products industry. *IEEE Ultrasonics Symposium, 2008. IUS 2008*. November 2008:694-704. doi: 10.1109/ULTSYM.2008.0167.
19. Länge K, Rapp BE, Rapp M. Surface acoustic wave biosensors: A review. *Anal Bioanal Chem*. 2008;391(5):1509-19.
20. Gallagher DG, Manley RJ. Diver's full face mask head-up display system using waveguide optical display technology OSJ #x2014; 140214 #x2013;001. *Oceans - St. John's, 2014*. 2014:1-7. doi: 10.1109/OCEANS.2014.7002976.
21. Chun-da Liao, Jui-che Tsai. The evolution of MEMS displays. *IEEE Transactions on Industrial Electronics*. 2009;56(4):1057-1065. http://ieeexplore.ieee.org/xpls/abs_all.jsp?arnumber=4663691. doi: 10.1109/TIE.2008.2005684.
22. Jaehong Park, Shim ES, Wooyeol Choi, Youngmin Kim, Youngwoo Kwon, Dong-il Cho. A non-contact-type RF MEMS switch for 24-GHz radar applications. *Journal of Microelectromechanical Systems*. 2009;18(1):163-173. http://ieeexplore.ieee.org/xpls/abs_all.jsp?arnumber=4752736. doi: 10.1109/JMEMS.2008.2011124.
23. Yao JJ. RF MEMS from a device perspective. *Journal of Micromechanical Microengineering*. 2000;10:R38.
24. Dulski R, Bareła J, Trzaskawka P, Piątkowski T. Application of infrared uncooled cameras in surveillance systems. . 2013;8896. doi: 10.1117/12.2028507.
25. Lee BS, Lin SC, Wu WJ, Wang XY, Chang PZ, Lee CK. Piezoelectric MEMS generators fabricated with an aerosol deposition PZT thin film. *Journal of Micromechanical Microengineering*. 2009;19:065014.
26. Yamazaki, Yoshino, Yoshizawa, et al. Pattern formation of sputtered films by deposition through mask. *Japanese Journal of Applied Physics*. 1996;35(Part 1, No. 9A):4755-4759. http://stacks.iop.org/1347-4065/35/4755. doi: 10.1143/JJAP.35.4755.
27. Sopori BL, Chang WSC. Some investigations on deposition and etching profiles in masked rf sputtering. *Journal of Vacuum Science and Technology*. 1977;14:782-786. http://scitation.aip.org/content/avs/journal/jvst/14/3/10.1116/1.569267. doi: 10.1116/1.569267.
28. Yao SK. Theoretical model of thin-film deposition profile with shadow effect. *Journal of Applied Physics*. 1979;50(5):3390-3396. http://scitation.aip.org/content/aip/journal/jap/50/5/10.1063/1.326330. doi: 10.1063/1.326330.
29. Tixier A, Mita Y, Gouy JP, Fujita H. A silicon shadow mask for deposition on isolated areas. *Journal of Micromechanics and Microengineering*. 2000;10(2):162. http://stacks.iop.org/0960-1317/10/i=2/a=310?key=crossref.a132af2290fa5324ea79da2d297e0ee8. doi: 10.1088/0960-1317/10/2/310.
30. Vazquez-Mena, Sannomiya, Tosun, et al. High-resolution resistless nanopatterning on polymer and flexible substrates for plasmonic biosensing using stencil masks. *ACS Nano*. 2012;6(6):5474-5481. http://pubs.acs.org/doi/abs/10.1021/nn301358n. doi: 10.1021/nn301358n.
31. Switkes M, Rothschild M. Immersion lithography at 157 nm. *J VAC SCI TECHNOL B MICROELECTRON NANOMETER STRUCT*. 2001;19(6):2353-2356.
32. Kono T, Higashiki T, Ito S, et al. Implementation of immersion lithography to NAND/CMOS device manufacturing. *4th International Symposium on Immersion Lithography*. 2007.

33. French RH, Sewell H, Yang MK, et al. Imaging of 32-nm 1:1 lines and spaces using 193-nm immersion interference lithography with second-generation immersion fluids to achieve a numerical aperture of 1.5 and a k1 of 0.25. *Journal of Micro/Nanolithography*. 2005;4(3). http://nanolithography.spiedigitallibrary.org/article.aspx?articleid=1097761. doi: 10.1117/1.2039953.
34. O'Sullivan, Kilbane, D'Arcy. Recent progress in source development for extreme UV lithography. *Journal of Modern Optics*. 2012;59(10):855-872. http://www.tandfonline.com/doi/abs/10.1080/09500340.2012.678399. doi: 10.1080/09500340.2012.678399.
35. Pret, Gronheid, Engelen, Yan, Leeson, Younkin. Evidence of speckle in extreme-UV lithography. *Optics Express*. 2012;20(23):25970. http://www.opticsinfobase.org/abstract.cfm?URI=oe-20-23-25970. doi: 10.1364/OE.20.025970.
36. Wood O, Koay C, Petrillo K, et al. Integration of EUV lithography in the fabrication of 22-nm node devices. *Alternative Lithographic Technologies*. 2009:727104. http://proceedings.spiedigitallibrary.org/proceeding.aspx?articleid=1336313.
37. Bondur JA. Dry process technology (reactive ion etching). *Journal of Vacuum Science and Technology*. 1976;13(5):1023-1029. http://ieeexplore.ieee.org/xpl/freeabs_all.jsp?arnumber=4952466&abstractAccess=no&userType=inst. doi: 10.1116/1.569054.
38. Guo, Chou, Mu, Liu, Xiong. Fabrication of micro-trench structures with high aspect ratio based on DRIE process for MEMS device applications. *Microsystem Technologies*. 2013;19(7):1097-1103. http://link.springer.com/10.1007/s00542-012-1720-9http://link.springer.com/content/pdf/10.1007/s00542-012-1720-9. doi: 10.1007/s00542-012-1720-9.
39. Zhang X, Di Q, Zhu F, Sun G, Zhang H. Superhydrophobic micro/nano dual-scale structures. *Journal of Nanoscience and Nanotechnology*. 2013;13(2):1539-1542. http://openurl.ingenta.com/content/xref?genre=article&issn=1533-4880&volume=13&issue=2&spage=1539http://www.ingentaconnect.com/content/asp/jnn/2013/00000013/00000002/art00174. doi: 10.1166/jnn.2013.5986.
40. Rogner A, Eicher J, Munchmeyer D, Peters R-, Mohr J. The LIGA technique-what are the new opportunities. *Journal of Micromechanics and Microengineering*. 1992;2(3):133-140. http://stacks.iop.org/0960-1317/2/i=3/a=004?key=crossref.27e283d0dcec8f59698bd39d50912d5b. doi: 10.1088/0960-1317/2/3/004.
41. Jain A, Shekhar C, Gopal R. Fabrication of two-gimbal Ni–Fe torsional micro-gyroscope by SU-8 based UV-LIGA process. *Microsystem Technologies*. 2014. http://link.springer.com/10.1007/s00542-014-2268-7http://link.springer.com/content/pdf/10.1007/s00542-014-2268-7. doi: 10.1007/s00542-014-2268-7.
42. Champagne C, Weiss L. Simple and low cost method for metal-based micro-capillary channels for heat exchanger use. *Journal of Micromechanical Microengineering*. 2013;23:115013.
43. Chung CK, Sher KL, Syu YJ, Cheng CC. Fabrication of cone-like microstructure using UV LIGA-like for light guide plate application. *Microsystem Technologies*. 2010;16:1624. http://link.springer.com/10.1007/s00542-009-1012-1http://www.springerlink.com/index/pdf/10.1007/s00542-009-1012-1. doi: 10.1007/s00542-009-1012-1.

44. Piner RD, Zhu J, Xu F, Hong S, Mirkin CA. "Dip-pen" nanolithography. *Science*. 1999;283(5402):661-663. http://www.sciencemag.org/content/283/5402/661.full. doi: 10.1126/science.283.5402.661.
45. Jung I, Son JY, Koh Y-. Dip-pen lithography of BiFeO3 nanodots. *Journal of the American Ceramic Society*. 2012;95(12):3716-3718. http://eds.a.ebscohost.com/ehost/detail/detail?sid=f3300612-dd88-4eaf-998b-3f773e0c4fca%40sessionmgr4004&vid=0&hid=4108&bdata=JnNpdGU9ZWhvc3QtbGl2ZQ%3d%3d#db=aph&AN=83877486. doi: 10.1111/jace.12008.
46. Gilles S, Tuchscherer A, Lang H, Simon U. Dip-pen-based direct writing of conducting silver dots. *Journal of Colloid and Interface Science*. 2013;406:256-262. http://www.sciencedirect.com/science/article/pii/S0021979713004864. doi: 10.1016/j.jcis.2013.05.047.
47. Salaita K, Wang Y, Fragala J, Vega RA, Liu C, Mirkin CA. Massively parallel Dip–Pen nanolithography with 55 000-pen two-dimensional arrays. *Angewandte Chemie*. 2006;118(43):7378–7381. http://onlinelibrary.wiley.com/doi/10.1002/ange.200603142/full. doi: 10.1002/ange.200603142.
48. Zhou X, Liu Z, Xie Z, Liu X, Zheng Z. High-resolution, large-area, serial fabrication of 3D polymer brush structures by parallel dip-pen nanodisplacement lithography. *Small*. 2012;8(23):3568–3572. http://onlinelibrary.wiley.com/doi/10.1002/smll.201201544/abstract;jsessionid=A666EE0371AEA5992CD5CF0D67FA889E.f03t04. doi: 10.1002/smll.201201544.
49. Veiko VP, Shakhno EA, Smirnov VN, Miaskovski AM, Nikishin GD. Laser–induced film deposition by LIFT: Physical mechanisms and applications. *Laser and Particle Beams*. 2006;24(02). http://www.journals.cambridge.org/abstract_S0263034606060289. doi: 10.1017/S0263034606060289.
50. Esrom H, Zhang J, Kogelschatz U, Pedraza AJ. New approach of a laser-induced forward transfer for deposition of patterned thin metal films. *Applied Surface Science*. 1995;86(1–4):202-207. http://www.sciencedirect.com/science/article/pii/0169433294003858. doi: 10.1016/0169-4332(94)00385-8.
51. Baum, Kim, Alexeev, Piqué, Schmidt. Generation of transparent conductive electrodes by laser consolidation of LIFT printed ITO nanoparticle layers. *Applied Physics A*. 2013;111(3):799-805. http://link.springer.com/10.1007/s00339-013-7646-yhttp://link.springer.com/content/pdf/10.1007/s00339-013-7646-y. doi: 10.1007/s00339-013-7646-y.
52. Ballentine PH, Kadin AM, Fisher MA, Mallory DS, Donaldson WR. Microlithography of high-temperature superconducting films: Laser ablation vs. wet etching. *IEEE Transactions on Magnetics*. 1989;25(2):950-953. http://ieeexplore.ieee.org/xpls/abs_all.jsp?arnumber=92445&tag=1. doi: 10.1109/20.92445.
53. Bovatsek J, Tamhankar A, Patel RS, Bulgakova NM, Bonse J. Thin film removal mechanisms in ns-laser processing of photovoltaic materials. *Thin Solid Films*. 2010;518(10):2897-2904. http://www.sciencedirect.com/science/article/pii/S0040609009018094. doi: 10.1016/j.tsf.2009.10.135.
54. Heise G, Englmaier M, Hellwig C, Kuznicki T, Sarrach S, Huber HP. Laser ablation of thin molybdenum films on transparent substrates at low fluences. *Applied Physics A*. 2010;102(1):173-178. http://link.springer.com/10.1007/s00339-010-5993-

5http://www.springerlink.com/index/pdf/10.1007/s00339-010-5993-5. doi: 10.1007/s00339-010-5993-5.
55. Ehrhardt M, Wehrmann A, Lorenz P, Zimmer K. Patterning of CIGS thin films induced by rear-side laser ablation of polyimide carrier foil. *Applied Physics A*. 2013;113(2):309-313. http://link.springer.com/10.1007/s00339-013-7962-2http://link.springer.com/content/pdf/10.1007/s00339-013-7962-2. doi: 10.1007/s00339-013-7962-2.
56. Bischof J, Scherer D, Herminghaus S, Leiderer P. Dewetting modes of thin metallic films: Nucleation of holes and spinodal dewetting. *Phys Rev Lett*. 1996;77(8):1536-1539.
57. Wyart, Daillant. Drying of solids wetted by thin liquid films. *Canadian Journal of Physics*. 1990;68(9):1084-1088. http://www.nrcresearchpress.com/doi/abs/10.1139/p90-151. doi: 10.1139/p90-151.
58. Reiter. Dewetting of thin polymer films. *Physical Review Letters*. 1992;68(1):75-78. http://link.aps.org/doi/10.1103/PhysRevLett.68.75. doi: 10.1103/PhysRevLett.68.75.
59. Redon, Brzoska, Brochard-Wyart. Dewetting and slippage of microscopic polymer films. *Macromolecules*. 1994;27(2):468-471. http://pubs.acs.org/doi/abs/10.1021/ma00080a021. doi: 10.1021/ma00080a021.
60. Sharma A, Reiter G. Instability of thin polymer films on coated substrates: Rupture, dewetting, and drop formation. *Journal of Colloid and Interface Science*. 1996;178(2):383-399. http://www.sciencedirect.com/science/article/pii/S0021979796901332. doi: 10.1006/jcis.1996.0133.
61. Favazza C, Kalyanaraman R, Sureshkumar R. Robust nanopatterning by laser-induced dewetting of metal nanofilms. *Nanotechnology*. 2006;17:4234.
62. Trice, Thomas, Favazza, Sureshkumar, Kalyanaraman. Pulsed-laser-induced dewetting in nanoscopic metal films: Theory and experiments. *Physical Review B*. 2007;75(235439). http://link.aps.org/doi/10.1103/PhysRevB.75.235439. doi: 10.1103/PhysRevB.75.235439.
63. Krishna, Favazza, Gangopadhyay, Kalyanaraman. Functional nanostructures through nanosecond laser dewetting of thin metal films. *JOM*. 2008;60(9):37-42. http://link.springer.com/10.1007/s11837-008-0115-y.
64. Trice, Favazza, Thomas, Garcia, Kalyanaraman, Sureshkumar. Novel self-organization mechanism in ultrathin liquid films: Theory and experiment. *Physical Review Letters*. 2008;101(1). http://link.aps.org/doi/10.1103/PhysRevLett.101.017802. doi: 10.1103/PhysRevLett.101.017802.
65. Krishna H, Sachan R, Strader J, Favazza C, Khenner M, Kalyanaraman R. Thickness-dependent spontaneous dewetting morphology of ultrathin ag films. *Nanotechnology*. 2010;21:155601.
66. McKeown, Roberts, Fowlkes, et al. Real-time observation of nanosecond liquid-phase assembly of nickel nanoparticles via pulsed-laser heating. *Langmuir*. 2012;28(49):17168-17175. http://pubs.acs.org/doi/abs/10.1021/la303657e. doi: 10.1021/la303657e.
67. Rack PD, Guan Y, Fowlkes JD, Melechko AV, Simpson ML. Pulsed laser dewetting of patterned thin metal films: A means of directed assembly. *Appl Phys Lett*. 2008;92:223108.
68. Fowlkes JD, Kondic L, Diez J, Wu Y, Rack PD. Self-assembly versus directed assembly of nanoparticles via pulsed laser induced dewetting of patterned metal films. *Nano Lett*. 2011;11:2478-2485.

69. Roberts NA, Fowlkes JD, Mahady K, Afkhami S, Kondic L, Rack PD. Directed assembly of one- and two-dimensional nanoparticle arrays from pulsed laser induced dewetting of square waveforms. *ACS Applied Materials & Interfaces*. 2013;5:4450-4456. doi: 10.1021/am400925h.
70. Kuznetsov A, Koch J, Chichkov B. Nanostructuring of thin gold films by femtosecond lasers. *Appl Phys A*. 2009;94:221-230.
71. Riedel S, Schmotz M, Leiderer P, Boneberg J. Nanostructuring of thin films by ns pulsed laser interference. *Appl Phys A*. 2010;101(2):309-312.
72. Riedel S, Leiderer P, Scheer E, Boneberg J. Pulsed laser interference patterning of metallic thin films. *Acta Physica Polonica A*. 2012;121(2):385-387.
73. Willis DA, Xu X, Poon CC, Tam AC. Laser-assisted surface modification of thin chromium films. *Optical Engineering*. 1998;37(3):1033-1041. http://opticalengineering.spiedigitallibrary.org/article.aspx?doi=10.1117/1.601938. doi: 10.1117/1.601938.
74. Singer JP, Lin P, Kooi SE, Kimerling LC, Michel J, Thomas EL. Direct-write thermocapillary dewetting of polymer thin films by a laser-induced thermal gradient. *Advanced Materials*. 2013;25:6100-6105. doi: 10.1002/adma.201302777.
75. Levine M, Ilkka G, Weiss P. Relation of the critical surface tension of polymers to adhesion. *Journal of Polymer Science Part B: Polymer Letters*. 1964;2(9):915–919. http://onlinelibrary.wiley.com/doi/10.1002/pol.1964.110020918/abstract. doi: 10.1002/pol.1964.110020918.
76. Fox HW, Zisman WA. The spreading of liquids on low energy surfaces. I. polytetrafluoroethylene. *Journal of Colloid Science*. 1950;5(6):531. http://www.sciencedirect.com/science/article/pii/0095852250900444. doi: 10.1016/0095-8522(50)90044-4.
77. Tyson WR, Miller WA. Surface free energies of solid metals: Estimation from liquid surface tension measurements. *Surface Science*. 1977;62(1):267-276. http://www.sciencedirect.com/science/article/pii/0039602877904423. doi: 10.1016/0039-6028(77)90442-3.
78. Jones H. The surface energy of solid metals. *Metal Science and Technology*. 1971;5(1):15-18. http://www.maneyonline.com/doi/abs/10.1179/030634571790439342http://www.ingentaconnect.com/content/maney/msc/1971/00000005/00000001/art00004. doi: 10.1179/030634571790439342.
79. Young T. An essay on the cohesion of fluids. *Philosophical Transactions of the Royal Society of London*. 1805;95:65-87. http://www.jstor.org/stable/107159?seq=1#page_scan_tab_contents.
80. Sharma A, Ruckenstein E. Energetic criteria for the breakup of liquid films on nonwetting solid surfaces. *Journal of Colloid and Interface Science*. 1990.
81. Wenzel RN. Resistance of solid surfaces to wetting by water. *Industrial & Engineering Chemistry*. 1936;28(8):988-994. http://pubs.acs.org/doi/abs/10.1021/ie50320a024. doi: 10.1021/ie50320a024.
82. Cassie ABD, Baxter S. Wettability of porous surfaces. *Transactions of the Faraday Society*. 1944;40. http://xlink.rsc.org/?DOI=tf9444000546. doi: 10.1039/tf9444000546.
83. Marmur. Wetting on hydrophobic rough surfaces: To be heterogeneous or not to be? *Langmuir*. 2003;19(20):8343-8348. http://pubs.acs.org/doi/abs/10.1021/la0344682. doi: 10.1021/la0344682.
84. Feng, Zhang, Xi, et al. Petal effect: A superhydrophobic state with high adhesive force. *Langmuir*. 2008;24(8):4114-4119. http://pubs.acs.org/doi/abs/10.1021/la703821h. doi: 10.1021/la703821h.

85. Beni G, Hackwood S. Electro-wetting displays. *Applied Physics Letters*. 1981;38(4):207. http://scitation.aip.org/content/aip/journal/apl/38/4/10.1063/1.92322. doi: 10.1063/1.92322.
86. Colgate E, Matsumoto H. An investigation of electrowetting-based microactuation. *Journal of Vacuum Science & Technology A: Vacuum, Surfaces, and Films*. 1990;8(4):3625. http://scitation.aip.org/content/avs/journal/jvsta/8/4/10.1116/1.576516. doi: 10.1116/1.576516.
87. Vallet, Vallade, Berge. Limiting phenomena for the spreading of water on polymer films by electrowetting. *The European Physical Journal B*. 1999;11(4):583-591. http://link.springer.com/10.1007/s100510051186http://www.springerlink.com/index/pdf/10.1007/s100510051186. doi: 10.1007/s100510051186.
88. Rival A, Jary D, Delattre C, et al. An EWOD-based microfluidic chip for single-cell isolation, mRNA purification and subsequent multiplex qPCR. *Lab on a Chip*. 2014;14(19). http://xlink.rsc.org/?DOI=C4LC00592A. doi: 10.1039/C4LC00592A.
89. Brown CV, McHale G, Trabi CL. Dielectrophoresis-driven spreading of immersed liquid droplets. *Langmuir*. 2015;31(3):1011-1016. http://pubs.acs.org/doi/abs/10.1021/la503931phttp://pubs.acs.org/doi/pdf/10.1021/la503931p. doi: 10.1021/la503931p.
90. Wooten F. *Optical properties of solids.* New York City, NY: Academic Press; 1972.
91. Brown MS, Arnold CB. Fundamentals of laser-material interaction and application to multiscale surface modification. In: Sugioka K, Meunier M, Piqué A, eds. *Laser precision microfabrication.* Springer Berlin Heidelberg; 2010:91-120. 10.1007/978-3-642-10523-4_4.
92. Weaver JH, Frederikse HPR. Optical properties of selected elements. In: Haynes WM, ed. *Handbook of chemistry and physics.* ; 2013.
93. Schlessinger, Wright. Inverse-bremsstrahlung absorption rate in an intense laser field. *Physical Review A*. 1979;20(5):1934-1945. http://link.aps.org/doi/10.1103/PhysRevA.20.1934. doi: 10.1103/PhysRevA.20.1934.
94. Thermal conductivity of metals and semiconductors as a function of temperature. In: Haynes WM, ed. *CRC handbook of chemistry and physics.* ; 2015.
95. Kalyon M, Yilbas BS. Repetitive laser pulse heating analysis: Pulse parameter variation effects on closed form solution. *Applied Surface Science*. 2006;252:2242-2250. doi: 10.1016/j.apsusc.2005.04.032.

2 Experimental

2.1 Introduction

In the course of developing the direct-write dewetting technique, various components for the laser/scanner system were considered, however, specific models were chosen due to their compatibility and versatility. With respect to the patterned films, a number of characterization techniques were used to describe the capabilities of the patterning system and the characteristics of the created features. From the initial creation of the films, to the patterns created out of those films, the techniques used in this work will be discussed and explored in the following section.

2.2 Deposition of Materials

All the films were created using some form of high-vacuum deposition on to a number borosilicate glass slides. These slides provided the mechanical support for the polymer substrate. Parylene-C was chosen as a high melting point polymer substrate with low surface energy. Its molecular structure is displayed in **Figure 2.1**.[1] Deposition is carried out by a chemical vapor deposition process where the dimer version of molecule first is vaporized into the system. This vapor is then pyrolyzed at high temperature, after which it deposits onto all surfaces of the chamber by a polymerization reaction.

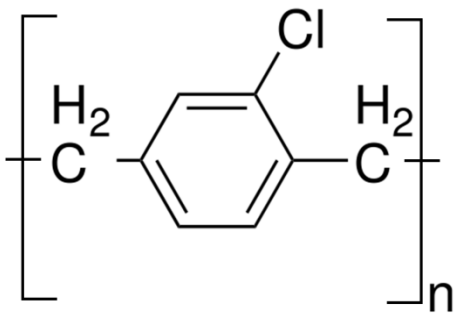

Figure 2.1: The general chemical structure of parylene-C.

The metal films were deposited using physical vapor deposition techniques. Bismuth, tin, and silver were all created using a PVD products thermal evaporator. This particular system was connected to an argon-filled glove box to reduce the possibility of oxygen or water contamination of the films. Thermal evaporation is conducted using a high vacuum system, where a target is heated to its vaporization point. This creates a flux of target atoms that move through the vacuum chamber and eventually condensate onto the desired substrate.[2] In this manner, films that are normally not stable may be formed via the large change in the free energy of the metal when colliding with such a relatively cold surface. Nickel films were created using sputter deposition. Rather than heating up a target material, the chamber is placed under high voltage. An ionized sputtering gas is flowed into the system, where it is accelerated towards the sputtering target, where portions of the target are knocked off onto the desired substrate.[3]

2.3 Laser and Galvanometer system

Laser stands for “Light Amplification by Stimulated Emission of Radiation.”[4] As the acronym suggests, lasers operate by a pump/stimulation mechanism. The basic parts of a laser device consist of the following: the energy pump, the laser gain medium, and the

resonator cavity. The essential mechanism relies on the transition states of electron orbitals. By pumping light into the resonator cavity, electrons inside the gain medium are excited into higher energy states. While some electrons will decay spontaneously, other electrons will decay after interacting with more excitation energy, thus releasing another photon. When this occurs, the emitted photons are said to be the result of stimulated emission, and will be coherent and monochromatic. Thus, in this manner, the emitted light builds up and is amplified.

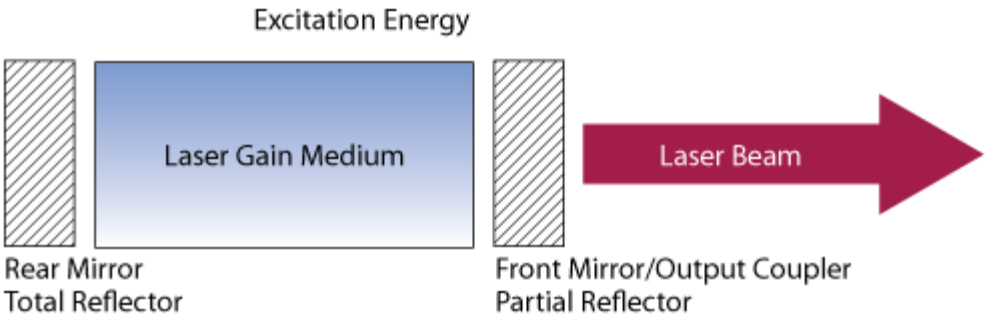

Figure 2.2: Typical solid-state laser configuration.[5]

The most common industrial lasers use solid-state media, such as Nd:YAG or a CO_2 gas mixture. These types of lasing media operate in the near-IR (1064 nm) and far-IR (10600 nm) range respectively. In order for the laser to function properly, mirrors must be placed at each end of the laser cavity to reflect emitted photons back into the structure, and thus amplify the stimulating photon energy. Alignment of these mirrors is essential for the proper functioning of the laser, as even a slight misalignment will cause a drop in lasing efficiency.

Fiber lasers offer an effective way to forgo the need for complicated mirror construction by taking a fiber optic cable and using it as the gain medium itself. In this way, the fiber's total internal reflection phenomenon may be taken advantage of to

create a long laser cavity without needing complicated mirror alignment. Ball and Glenn detailed the design of such a fiber laser using an erbium doped silica fiber.[6] In substitution of the mirrors found in solid-state or gas lasers, Bragg reflectors were embedded into the fiber to ensure that the majority of the emitted photons were reflected back into the system to further fuel the amplification. A diagram of their system can be found in **Figure 2.3**.

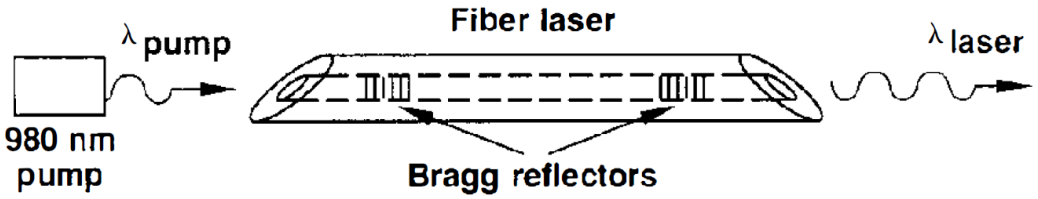

Figure 2.3: Diagram of a fiber laser with Bragg reflectors. © 1992 IEEE[6]

While Ball and Glenn used an erbium doped fiber, other groups have investigated the usefulness of different dopants. Ytterbium has been shown to be a useful dopant in silica fiber lasers due to its large absorption and emission bands. The relevant electronic structure is depicted in **Figure 2.4**. Effective pumping wavelengths for Yb-doped fibers can range from ~ 800 nm to ~1064 nm, which opens up the possibility of using a second laser as the pump source, though it has been shown that a wavelength of 975 nm accesses the largest absorption cross-section for the material.[7] Additionally, one must also take into consideration that the pump radiation must be of shorter wavelength and higher energy than the desired lasing wavelength.

For this work, a high-powered, Yb-doped fiber laser was chosen. The redPOWER R4 HS laser (SPI Laser, UK) has a maximum average power of 100 W exhibited a TEM_{00} beam quality. Both continuous wave and modulated operation was possible. For

highly reflective metals, continuous wave operation was used at a power 25 W. All other processing was conducted at the lowest setting of 10 W. Modulation was controlled via computer software and control board. Typical settings had the laser pulse at a frequency of 50 kHz with pulse durations of 5 μs. This corresponds to a 25% work load.

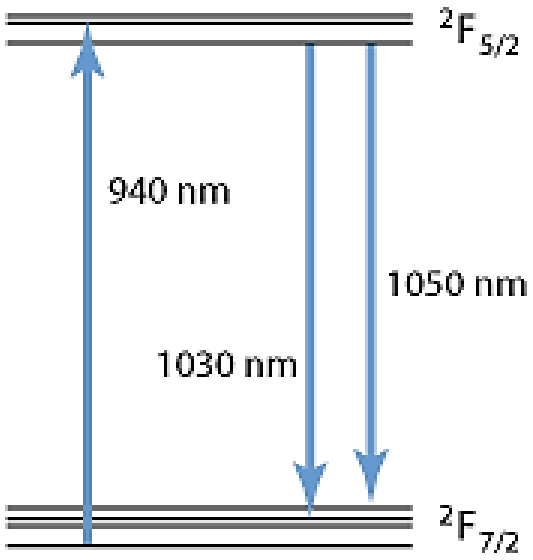

Figure 2.4: Electronic band structure of Yb doped silica fibers.

Beam positioning was achieved using a pair of galvanometer driven mirrors. Galvanometers use electric currents to create magnetic fields around a permanent magnet, which for the most basic designs are connected to springs to impeded movement. By altering the strength and direction of the current, the permanent magnet will experience a magnetic force and a movement. This movement can be controlled to a high degree and at a very rapid pace to allow fast turnings of the mirror, thus allowing very fast laser positioning.[8] A photograph of the intelliSCAN 20, scanner system purchased from Scanlab along with the in-line camera and beam delivery optics can be seen in **Figure 2.5**. Also, a photograph of the entire system may be seen in **Figure 2.6**,

which shows the laser exposure area, Class 1 light-tight enclosure, power supply box, and the fiber laser.

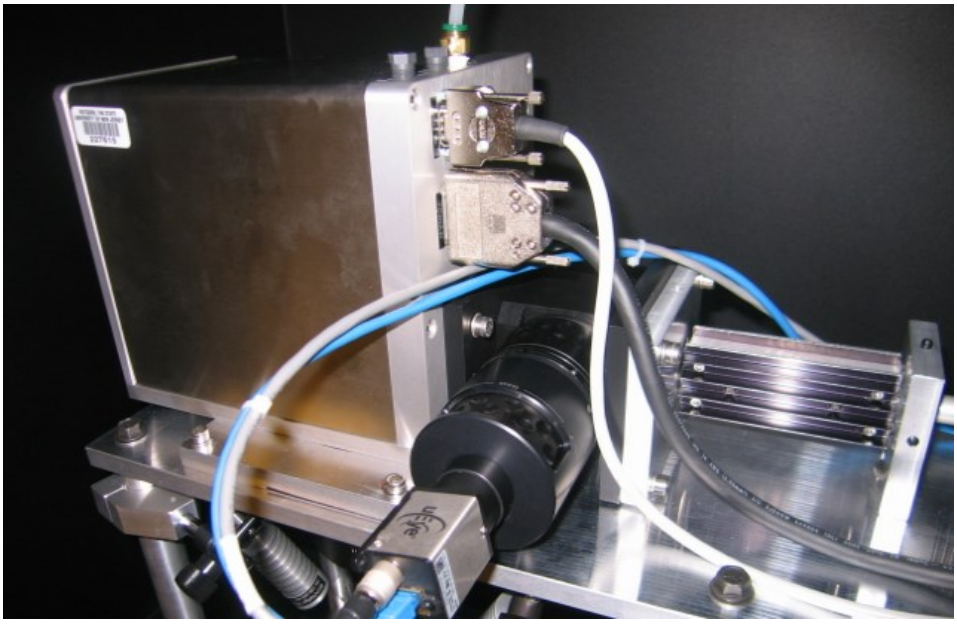

Figure 2.5: Scanlab intelliSCAN 20 scan system

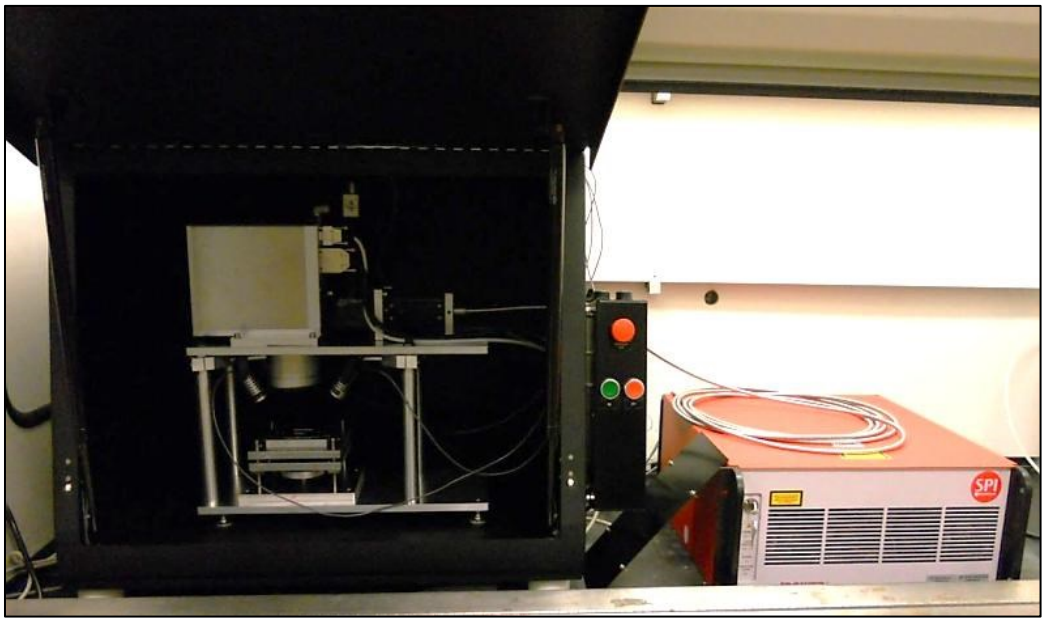

Figure 2.6: Photograph of entire system.

2.4 Characterization

Profilometry measurements were carried out using a VEECO Dektak 150 system. All profile recordings were performed using at 2.5 μm diameter stylus tip at 0.5 mg of force. Sampling rates ranged from 1 μm/sample down to 0.050 μm/sample. Three-dimensional models of the surfaces were created using serial and adjacent 2D scans of the surface. These scans featured a spatial resolution of 1 μm/sample in both directions. **Figure 2.7** displays the profilometer, within its enclosure. Post-processing of the 3D scans was carried out using Vision software.

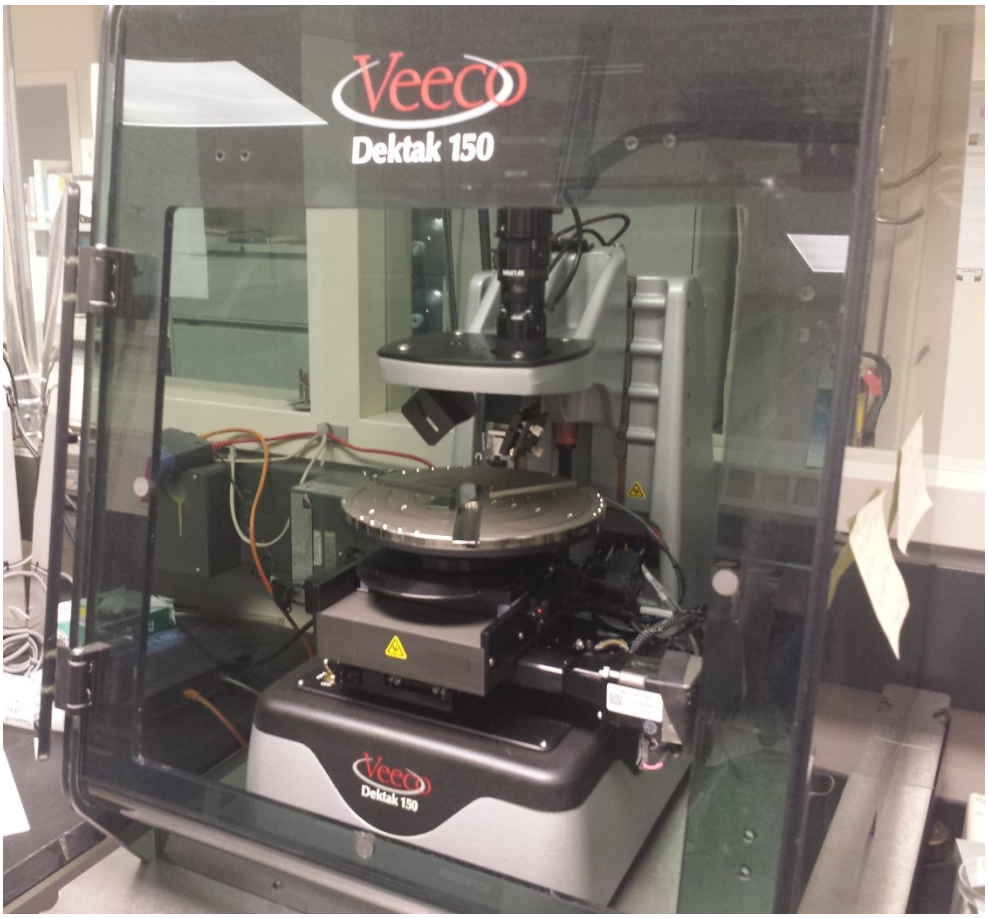

Figure 2.7: Dektak 150 profilometer system with a 2.5 μm stylus tip.

2.5 References

1. Pruden KG, Sinclair K, Beaudoin S. Characterization of parylene-N and parylene-C photooxidation. *Journal of Polymer Science Part A: Polymer Chemistry*. 2003;41(10):1486–1496. http://onlinelibrary.wiley.com/doi/10.1002/pola.10681/full. doi: 10.1002/pola.10681.
2. Mahan JE. *Physical vapor deposition of thin films.* New York, NY: John Wiley & Sons, Inc.; 2000.
3. Yamazaki, Yoshino, Yoshizawa, et al. Pattern formation of sputtered films by deposition through mask. *Japanese Journal of Applied Physics*. 1996;35(Part 1, No. 9A):4755-4759. http://stacks.iop.org/1347-4065/35/4755. doi: 10.1143/JJAP.35.4755.
4. Gould RG. The LASER, light amplification by stimulated emission of radiation. *The Ann Arbor conference on optical pumping*. 1959.
5. Steen WM. *Laser material processing.* 3rd ed. London: Springer; 2003.
6. Ball GA, Glenn WH. Design of a single-mode linear-cavity erbium fiber laser utilizing bragg reflectors. *Journal of Lightwave Technology*. 1992;10(10):1338-1343. http://ieeexplore.ieee.org/xpls/abs_all.jsp?arnumber=166773&tag=1. doi: 10.1109/50.166773.
7. Pask HM, Carman RJ, Hanna DC, et al. Ytterbium-doped silica fiber lasers: Versatile sources for the 1-1.2 um region. *IEEE Journal of Selected Topics in Quantum Electronics*. 1995;1(1):13.
8. Brosens P. Scanning accuracy of the moving-iron galvanometer scanner. *Optical Engineering*. 1976;15(2):95-98.

3 Micro-patterning of Metallic Film Structures through Direct-Write Dewetting

3.1 Introduction

Thin film patterning is an essential technology that has enabled the miniaturization of many technologies in both the electronics and biomedical fields. Patterned thin films can be found in a variety of electronics applications including batteries, solar cells, transistors, microfluidics, patch antennas, and touch panels.[1-5] The biomedical field has developed a great need for such thin electrode arrays as well, particularly for point-of-care applications. Concepts such as the "lab-on-chip," implantable sensors, and ingestible probes rely on the biotech industry's ability to accurately and reproducibly create microscopic electrical conduits on increasingly thin substrates.[6,7] Additionally, the use of organic, flexible substrates will allow implementation of such electrodes into a wider range of products that can provide users and researchers with highly adaptable geometries for consumer and industrial electronics. If devices are to progressively occupy less space and continually exhibit higher functionality, all while remaining relatively low cost, then industrial processes must match this demand by developing innovative ways of patterning deposited thin films.

Two of the most prevalent modes of patterning thin films are shadow masked deposition and photolithography.[8] The former technique requires the creation of multiple yet expensive masks, which make changing designs, even slightly, both costly and time-consuming. The latter technique also uses masks for the purposes of patterning the area of exposure and incorporates various photoresists and chemical development steps leading to highly accurate features. In turn, the process is complicated and introduces

the need for a number of extra environmental engineering controls to deal with such potentially harmful chemicals. Some drawbacks are mitigated by using directed energy techniques to scribe out the negative space of a film through ablation, precluding the need for masks or etching steps. Such processes can use focused e-beams or laser radiation coupled with a scanning system to reduce production time, however, these techniques are still primarily subtractive in nature, result in the vaporization of a great deal of material that cannot be recovered, and are not well suited for temperature sensitive substrates. Other techniques – including those that are additive in nature (e.g. ink jet printing) – have their own drawbacks that must be overcome during implementation into current manufacturing processes.[9] An alternative to current patterning techniques resides in the use of dewetting to build patterned structures from an initially uniform target layer.

The shape of liquids on solid surfaces is dictated by the contact angle (**Figure 3.1a**). The latter is related to the materials' surface energy by the Young's Equation (**Equation 1**), where θ_c is the contact angle in thermodynamic equilibrium. Liquids that completely wet the solid correspond to $\theta_c = 0°$. Angles between 0° and 90° can be considered partially wetting, while angles greater than 90° are formed by non-wetting liquids. The wetting nature of a material can be described by the change in free energy with respect to the standard state, i.e. complete wetting of the solid by the liquid.[10] **Equation 2** details this free energy value as a combination of three components: gravitational forces ($\frac{1}{2}\rho g h^2$), intermolecular forces ($\frac{A}{12\pi h^2}$), and surface tension (S) . Surface topography will affect the apparent contact angle and by consequence the measured surface energy; however, materials will exhibit trends in surface energy values that are intrinsic to material classification. For example, metals tend to lie in the highest range of surface energy values, while materials such as polymers tend to have the lowest values.

Interfacial force influences the dewetting of metallic films deposited on substrates such as glass or polymeric compounds and can be measured by the spreading coefficient *S* (**Equation 3**). A film will spontaneously dewet when the change in free energy *S*<0 and has a thickness less than a critical height. In turn, this critical height is a function of capillary length and equilibrium contact angle and provides the basis for determining energetic stability of the film with respect to the substrate.[11] Studies on polymer films have shown that dewetting can occur by a number of mechanisms, including nucleation and growth of holes within the film and spontaneous spinodal dewetting.[12,13] Researchers have also initiated dewetting in films that would not do so independently. A number of mechanical methods have been employed, rather than relying on random impurities to serve as nucleation points and some control is established over the dewetting geometry and progression of a film on non-wetting surfaces.[14,15]

$$\gamma_{SL} + \gamma_{LG} \cos\theta_c = \gamma_{SG} \quad (\mathbf{1})$$

$$\Delta F(h) = \frac{1}{2}\rho g h^2 - S + \frac{A}{12\pi h^2} \quad (\mathbf{2})$$

$$S = \gamma_{SG} - (\gamma_{SL} + \gamma_{LG}) \quad (\mathbf{3})$$

This paper presents a novel variation on induced dewetting allowing rapid, directed patterning though the use of a high speed scanning laser. By taking a relatively low-powered Yb doped fiber laser and scanning it across the surface of a metallic thin-film, we demonstrate targeted melting and dewetting of the target film without damaging the integrity of the underlying polymer substrate. There is some precedent for induced

dewetting of metallic, thin film targets under a variety of non-scanning laser radiation conditions. In 1996, Bischof et. al. studied the dewetting modes of thin films after exposure from frequency doubled Nd:YAG radiation.[16] The authors demonstrate that deposited Au, Cu, and Ni thin films, which are metastable in nature, will dewet upon induced melting and will do so by nucleation of holes or by a spontaneous, spinodal fashion. Other researchers have built upon this dewetting phenomenon to create self-assembled features on Co and Au nano-films by using defocused laser light and pulses in the nanosecond regime.[17,18] It was shown that characteristic length scales developed as functions of the number pulses used, which allowed some control over the final dimensions of the pattern. Splitting a laser source into two or three beams to create interference has enabled the creation of periodic patterns on a variety of thin-film species, including Bi, Ge, Ni, Au, Cu, and Ta. Changing the arrangement and number of beams allows even more control over pattern design; however, such techniques are limited to lines, hexagonal patterns, and other geometry associated with intensity interference.[19,20] Placing masks along the beam path, which are then focused down to a smaller scale, offered additional freedom in shape patterning similar to photoresist methods, but suffer from similar drawbacks.[21] Pre-patterning of the thin film, followed by laser exposure imposes constraints on the acting surface tension in the melt and allowed a “directed assembly” of the dewetted material.[22,23] The techniques still requires the creation of masks for electron lithography and the subsequent use of lift-off processes, which hinders the speed of implementation, but offers much freedom for feature design. Our processing technique presented here-in relies on a number of system features, namely the high speed scanning system that affords the user a great deal of freedom in rapid direct scribe dewetting programs, while eliminating the need for costly lithographic masks and time-consuming pre-patterning steps. We will demonstrate the advantage of

using a focused laser to initiate dewetting at artificial nucleation points and create precise patterns on metallic films.

Choice of system materials is crucial to the exploration of this new technique as a number of attributes can affect both the dewetting behavior of the metal as well as its interaction with the laser radiation. Our first demonstration of this technique focuses primarily on bismuth depositions as the metal has a relatively low melting-point with a much higher vaporization-point, and a large liquid surface tension value. Additionally, bismuth absorbs a relatively large percentage of incident near-infrared (NIR) radiation, compared to metals such as copper, gold, or silver, which will reflect a much larger percentage of incident radiation at the utilized wavelength. The combination of low melting temperature and higher absorption makes it particularly applicable to polymer substrates. Tin presents as another viable candidate, as it also has a low melting point, high vaporization point, high surface tension, and exhibits relatively high absorption of NIR light. Suitable substrates exhibit lower surface energy than a metal, are electronically insulating, and have very low absorption of NIR light to avoid damage during laser processing. Reduced absorption also allows “backside” dewetting by laser transmission through the substrate. Both borosilicate glass and parylene, particularly parylene-C (par-C) meet these criteria. Where glass is highly transparent to NIR light, the surface energy is relatively high compared to most polymers. Par-C boasts a surface energy comparable to PTFE polymers, making it relatively easy for deposited metal to dewet from the surface. The polymer was deposited upon a borosilicate glass slide, which provides the necessary rigidity during processing, but still allows subsequent removal from the substrate. Thermal evaporation deposition of the target metal onto the substrate enables extremely fast cooling rates that result in a kinetic stabilization of metal films and a metastable, uniform wetting of the substrate.

3.2 Experimental

3.2.1 Laser System

The laser system consisted of a single-mode, Yb-doped, 100 W Fiber Laser (SPI redPOWER R4-HS) operating at 1070 nm. A computerized scan system (Scanlab IntelliSCAN 20) fitted with copper mirrors that are mounted on galvanometer scan motors. A camera system (uEye GigE) for in-situ monitoring of the scribing/dewetting process is placed along the beam path. Optics for the scan system consisted of an f-theta, telecentric lens with an effective focal length (EFL) of 115 mm, which provides a marking field of approximately 60 mm by 60 mm. The construction of the lens allows for a relatively flat focal plane and consistent laser intensity to all parts of the work piece. The substrate holder consisted of a custom designed, manual 2-axis tilt stage with Z-axis adjustment.

3.2.2 Substrate Preparation

Pre-cleaned borosilicate glass slides (25.4 mm x 76.2 mm x 1.0 mm, VWR) provided the underlying substrate for all samples. Average surface roughness (Ra) was measured at 7 nm $\pm$ 5 nm with a waviness factor (Wa) of 20 nm $\pm$ 5 nm. Parylene-C (Specialty Deposition Systems, PDS 2010) was deposited on the slides at a nominal thickness of 22 um $\pm$ 1 um. Ra values of deposited par-C were measured at 15 nm $\pm$ 5 nm with Wa values of 60 nm $\pm$ 5 nm. Unmasked metal deposition upon both glass and par-C substrates was carried out using high vacuum thermal evaporation. Samples were kept under an inert Ar atmosphere until immediately prior to laser exposure and are

stored in an inert atmosphere immediately following exposure until characterization is performed.

3.2.3 General Laser Parameters

Laser power was held at its lowest operating limit of 10 W for all target metals and substrates, to minimize thermal degradation. At the focal plane of the lens, the beam spot's diameter (D_s) is calculated using **Equation 4**, where *f* is the focal length of the lens, λ is the laser wavelength, D_B is the full-width, half-maximum (FWHM) beam diameter measured as it enters the lens, and M^2 is the beam quality factor describing the shape of the intensity distribution (where M=1 for perfect Gaussian distributions).

$$D_s = 1.27 * f * \lambda * {M^2}/{D_B} \quad (4)$$

Our laser system operates in a single-mode (TEM_{00}) fashion, with $M^2 < 1.1$ and produces a 5 mm $\pm$ 0.5 mm wide beam at its exit aperture. The beam has a divergence < 0.4 mrad and enters the lens aperture with a diameter of approximately 5.07 mm. Calculation of the spot diameter yields 33 um. Measurement of the width of the dewetted area resultant from a single pass of the beam confirms the diameter calculation. Exposures of larger areas were carried out by scanning the beam across the surface of the target metal. The top-down edge profile of a single, dewetting pass depends on a number of variables, including laser absorbance, thermal conductivity, solidification rate and thickness of the target metal. Pulse overlap will also influence the edge profile of the dewetted area as viewed from a top-down angle, where low overlap percentage will produce a scalloped edge. The overlap parameter is calculated using **Equation 5**,

where V is the scan speed, *f* is the pulse frequency, *T* is the pulse length, and *S* is the spot size.[24] On bismuth targets measuring 1.6 um in thickness, an overlap exceeding 75% was found to avoid a scalloped edge profile along the dewetted area. Pulse frequency and length are kept constant at 50 kHz and 5 us respectively, while the beam is scanned at 240 mm/s. Under the described conditions, the calculated overlap is 86%.

$$O_f = \left[1 - \left(V/f\right)\Big/(S + VT)\right] X\ 100 \qquad (\mathbf{5})$$

Tin targets measuring 1.6 um in thickness require a greater degree of overlap to avoid a scalloped top-down edge profile. Laser pulse frequency and length are held constant at 50 kHz and 5 μs respectively, while scan speed is conducted at 100 mm/s to achieve a calculated overlap of 94%. To prevent significant amounts of oxidation within the dewetted material, an argon gas blanket flowed at 80 standard cubic feet per hour (SCFH) over the sample during dewetting cycles. Pulse shaping corrections were enabled to prevent the spike in delivered power that is characteristic of the laser's first pulse. For dewetting geometries consisting of multiple passes or segments, the scanner's positioning speed was set equal to the marking speed designated for that metallic target.

3.2.4 Basic Laser Directed Dewetting

Bismuth metal was deposited in a dot-array pattern using a masked, vapor deposition technique. Deposited 130 um dots were centered 2.15 mm apart in a 9 x 13 dot array. Two such arrays were deposited upon each substrate. Substrates consisted

of uncoated borosilicate glass microscope slides, as well as slides with a 22 um thick deposited layer of par-C. Dots were deposited at three different thicknesses: 1000 nm, 2000 nm, and 4000 nm. As a result of shadowing effects from the masked deposition, each dot exhibited excess deposited material outside of the 130 um diameter. This excess material tapered down in thickness and extended out to a maximum diameter of 170 um $\pm$ 20 um. Exposure of the deposited dots proceeded in an Archimedean spiral pattern starting at a radius of 150 um and decreasing by 20 um with each turn. The center of the spiral pattern and the center of the deposited dot were aligned to within 10 um. Laser settings were set at the standard laser parameters for bismuth.

3.2.5 Line arrays

A number of various processing geometries were explored using both bismuth and tin films on par-C coated borosilicate glass. Bismuth films measuring 1.6 um thick were exposed to laser radiation in a set of line arrays. Exposure conditions mirrored the general laser parameters for bismuth films under focused conditions (pulse frequency = 50 kHz; pulse length = 5 us; power = 10 W; scan speed = 240 mm/s; positioning speed = 240 mm/s; Ar gas flow = 80 SCFH). The substrate was oriented with the metallic film facing the scan lens, which is characterized as a “front-side” dewetting condition. Each array of lines encompassed the area of a 2 mm x 2 mm square. Within the array, single lines of exposed substrate were formed via one pass of the laser each across the surface of the metal film. The scan lines were set at pitches as large as 200 um and were incrementally decreased down to a pitch of 55 um for bismuth films. Tin films, which measured 1.6 um thick, were exposed to line array patterns of a similar fashion. The pitch of the linear array features ranged from 200 um to 75 um. Exposure settings mirrored the general laser parameters for tin films, which were identical to those for

bismuth films, with the exception of the scan and positioning speeds. For tin films, scanning and positioning speed were set at 100 mm/s. Line arrays with a pitch of 100 um were chosen for further processing under defocused laser conditions. A defocused beam spot approximately 150 um in diameter – as measured by marks made on target films – was created by lowering the target stage 10 mm below the focal plane of the lens. The laser operated at 10 W, 10 kHz, with pulse durations of 40 us. The beam scanned at 1400 mm/s, which resulted in a pulse overlap calculated at 34%. Overlap was minimized to prevent over exposure and uncontrolled, random dewetting of the film.

3.2.6 Back-side Exposure

"Front-side" dewetting of thin films refers to the exposure of the bismuth layer through the argon gas blanket. In studies assessing the waveguide properties of par-C, transmission in the 1000 nm to 1500 nm range through a 15 um thick sample was cited as 85%; the rest of the radiation is either absorbed or reflected.[25] Literature values for borosilicate glass compositions similar to that of the microscope slide substrates indicate a transmittance of at least 88% in the near-IR range.[26] Exposure of bismuth samples proceeded in a "back-side" configuration, where laser light was directed through the substrate before interacting with the metallic layer. Under this configuration, exposure of the bismuth layer proceeded in a simple line-array pattern with a pitch of 200 um. The target stage was adjusted to compensate for the thickness of the glass substrate and ensure that the metal layer lied within the focal plane of the lens. Laser settings were set to match the general laser parameters for bismuth samples. A shallow relief milled into the target stage prevented unwanted transfer of the dewetted material onto the underlying support. The relief also ensured that the exposed bismuth had sufficient room to dewet and accumulate on the par-C/bismuth interface in an unhindered manner.

3.2.7 Accumulated Structures

To explore the accumulation behavior of dewetting-metal when deposited on par-C, multiple, closely-spaced scanner passes were used to successively melt an ever growing amount of material in a chosen direction. The overall shape of the accumulated structure was designed as a single, linear, thick bead of dewetted bismuth. The initial film used was a 1.6 um thick film of Bi deposited upon a 22 um par-C/1mm borosilicate glass substrate. The scan program proceeded as a linear array at a set pitch of 20 um. At such a small pitch, the dewetting metal preferentially accumulated in the direction of the advancing line front. In total, the accumulated line structure consisted of 36 scanner passes – 18 passes on each side of the line with converging line fronts. With each pass, laser energy "pushed" material towards the middle, where it combined to create one structure. General laser parameters for bismuth samples were used for each scanner pass. Alternate geometries of dewetted Bi were realized in the form of a spiral. The laser spot was scanned in an Archimedean spiral pattern, which started at a 1 mm radius and continued towards the center until the path reached a radius of 100 um. The separation distance between turns was set at 20 um to ensure preferential dewetting towards the center of the spiral. Profilometry was used for volumetric analysis of the accumulated material at the center of the spiral. An identical accumulated structure was created from a 1.6 um tin film using the general laser parameters for tin films.

3.2.8 Periodic Shapes

Periodic shapes were realized on 1.6 um thick bismuth targets deposited upon 22 um par-C/1mm borosilicate substrates. Laser settings matched the general laser

parameters for bismuth films. Within the confines of a 1 mm by 1 mm square, dewetting scanner passes were conducted with a pitch of 100 um in both the X- and Y-directions. The resulting square structures were then dewet along the diagonals to create triangular structures.

3.2.9 Polygonal and Circular Accumulated Structures

Accumulation processing techniques were used to create non-functional polygonal and circular structures. In total, three shapes were attempted: a triangle, a circle, and a square. Each side of each shape was constructed from 18 adjacent scanner passes – 9 from each side – which pushed together the dewetted metal to form the intended geometry. The successive passes were set at a pitch of 20 um. Additionally, an application-oriented design was attempted. Inter-digit electrodes (IDEs) were dewet from a 1.6 um Bi film using general laser parameters. Such IDEs can be constructed with variable spacing, variable electrode width, variable height, and lends itself well to defocused laser processing to normalize the height of the dewetted beads. The IDE scan program consisted of a linear array set at a pitch of 110 um to create the individual inter-digits. A single pass of the laser isolated the structure of the IDE from the surrounding metal film whilst also forming the electrode pads. In total, each electrode pad was designed with 45 inter-digits each. Small areas at the end of each inter-digit were “pushed” clear to ensure isolation from the opposite electrode pad. Together, the IDE filled an area 14 mm by 10 mm.

3.2.10 Complex Structures

As example of the level of complexity possible with the scan system and dewetting technique beyond simple polygonal or circular shapes, the letters “R” and “U” were designed using the presented techniques. Both letters were constructed using general laser settings. The attempted “R” was pushed together from 18 beam passes – 9 passes on each side – with a 20 um spacing. The attempted “U” was designed as an IDE with two inter-digits per electrode pad. Each digit is 70 um wide and spaced 30 um apart from each other. Each letter created was designed to fit within a 2.3 mm x 2.3 mm square.

3.2.11 Physical and Electronic Characterization

Samples were characterized using an optical microscope (Leitz) and a field-emission scanning electron microscope (FESEM) operating at 5kV. Samples were encased in a silver-containing, conductive epoxy to limit charging effects during characterization. A diamond band saw running at 250 rpm and an ion cross-polishing system (JEOL) running at 5.5 kV, were used to cut and polish cross-sectional samples of the constructed features. Contact angle images were created with a custom goniometer apparatus constructed with a precision optics table from Newport Corporation and a Wild Heerbrugg – MarkZoom lens mounted on its side. The analysis of the images was conducted using ImageJ software combined with the DropSnake plug-in.[27] Singular profilometry scans were conducted with a Dektak 150 profilometer with a lateral resolution of 0.050 um per sample. An accounting of the displaced volume of a dewetted line array was conducted using the profilometer and the accompanying Veeco

“Vision” software. A 3.9 mm x 2.5 mm area encompassing a 100 um pitched line array was scanned using the profilometer to create a 3D map. The line array itself measured 2 mm x 2 mm. Height sampling of the array was set such that individual readings were spaced one micron apart in both the X and Y directions. Electronic characterization proceeded with an Agilent 34410A Multimeter in a 2-wire configuration. Resistance measurements for inter-digit electrodes were carried out to ensure electrical isolation between the electrode pads as well as isolation of each pad from the rest of metallic layer. Any reading above the instrument’s gigaohm limit is taken as an indication of electronic isolation.

3.3 Results

3.3.1 Basic Laser Directed Dewetting

To explore the basic, laser-induced dewetting properties of a metal deposited upon a polymeric surface, arrays of 150 μm diameter bismuth dots were deposited on uncoated glass slides and parylene-C coated glass slides. Starting at a distance of 150 μm from the center of the dot, the laser beam was scanned in an Archimedean spiral pattern along the surface of the deposited metal. Each complete turn along the spiral path brought the beam 20 μm closer to the center of the dot until the center of the beam reached a radius of 35 μm. With a beam diameter of 33 μm, laser energy reached as far in as 18.5 μm from the center of the spiral. As the laser spot progressed along the preprogrammed path, the metal melted and retracted into a single dewetted mass located at the center of the spiral (**Figure 3.1b, 3.1c**). Attempts to end the spiral path of the beam at smaller radiuses were unsuccessful and resulted in complete detachment of

the dewetted mass. A side-view of the dewetted masses revealed an almost-spherical geometry, with contact angles between 117 to 130 degrees. The contact angle results from the difference in surface energies between the metal and the substrate, where the laser energy acts to accelerate the kinetics of the dewetting. Further work into the fundamentals and theory behind the basic directed-dewetting phenomena is currently under way and will be presented in future publications.

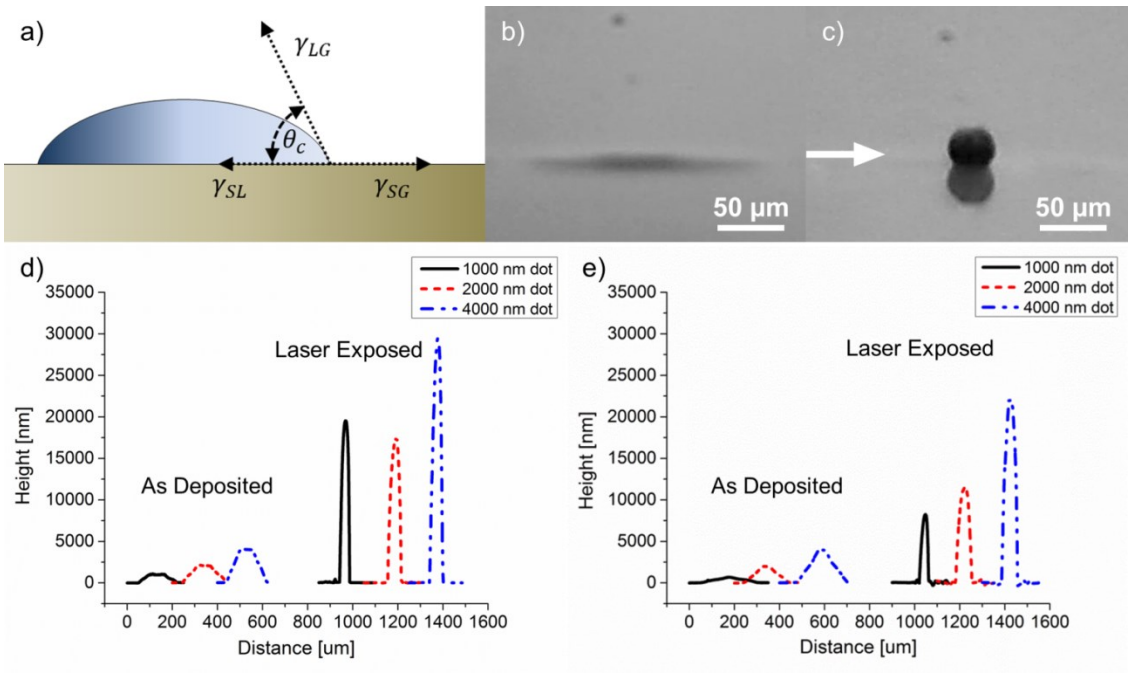

Figure 3.1: Under equilibrium conditions, the surface forces of each of each interface are balanced according to a) Young's Equation. A side view comparison of b) an as-deposited, 4000 nm thick Bi dot and c) a laser exposed Bi dot on a parylene-C coated borosilicate glass slide. d) Before and after laser exposure of dots deposited on borosilicate glass and e) par-C.

Profilometry measurements of the dewetted features revealed the extent of dewetting via the difference in height between the "as deposited" and the "laser exposed" conditions of the dots. For dots deposited upon uncoated borosilicate glass, the resulting heights in the dewetted feature increased significantly. Dots deposited at

1000 nm, 2000 nm, and 4000 nm dewetted to heights of 19500 nm (representing a 1850% increase), 17500 nm (775%), and 29250 nm (631%), respectively (**Figure 3.1d**). When deposited on par-C coated slides, the measured heights held a systematic, positive correlation with volume increase. Dots deposited at 1000 nm, 2000 nm, and 4000 nm dewetted on par-C to heights of 8750 nm (775%), 11500 nm (475%), and 22000 nm (450%), respectively (**Figure 3.1e**).

3.3.2 Simple Dewetting Geometry

3.3.2.1 Line Arrays

Features organized into parallel lines represent a fundamental geometry in modern electrode and electronics design. Viable patterning techniques must be able to accurately and reproducibly create such structures out of the target material. To this end, an array of isolated, parallel lines were dewetted from a single 1.6 μm Bi thin film. Substrates consisted of a borosilicate glass slide coated with 27 μm $\pm$ 3 μm of par-C. Each pass of the laser created an area of exposed substrate. Dewetted metal gathered along the edges of the exposed area, to create a dewetted bead. Height measurements of the dewetted bead show a marked increase in the metal thickness compared to the original layer thickness. Profilometry measurements place the height of the dewetted bead at 3.4 μm as measured from the substrate, which represents a 113% increase in the local thickness of the film. Both bismuth and tin were used to create line arrays but most of the work focused upon the behavior of the Bi films. The arrays were designed at various pitches, leading to changing widths of features, yet the areas of exposed substrate remained the same widths due to a consistent beam spot diameter. For a

single laser pass, we assumed an equal distribution of dewetted material to both sides. Thus, each bead was comprised of half the material dewetted from an individual laser pass. Dimensions of the dewetted beads remained relatively constant until line pitch decreased down to 75 μm. Profilometry data and optical analysis (**Figure 3.2a, 3.2b**) showed that when line pitch is set at 75 μm on a bismuth film, the dewetted beads made from adjacent laser passes combined into a single 3.85 μm thick, 35 μm wide bead. Further reduction in pitch down to 55 μm resulted in a single 6.67 μm thick, 17 μm wide bead (**Figure 3.2d-3.2f**). Aspect ratios of the 75 μm and the 55 μm spaced line arrays were 0.11:1 and 0.40:1 respectively. Further characterizations of the line arrays by FESEM confirmed these measurements and are highlighted in **Figure 3.2c** and **3.2f**. Within these two images, one can see the difference in aspect ratio between the two different pitch settings.

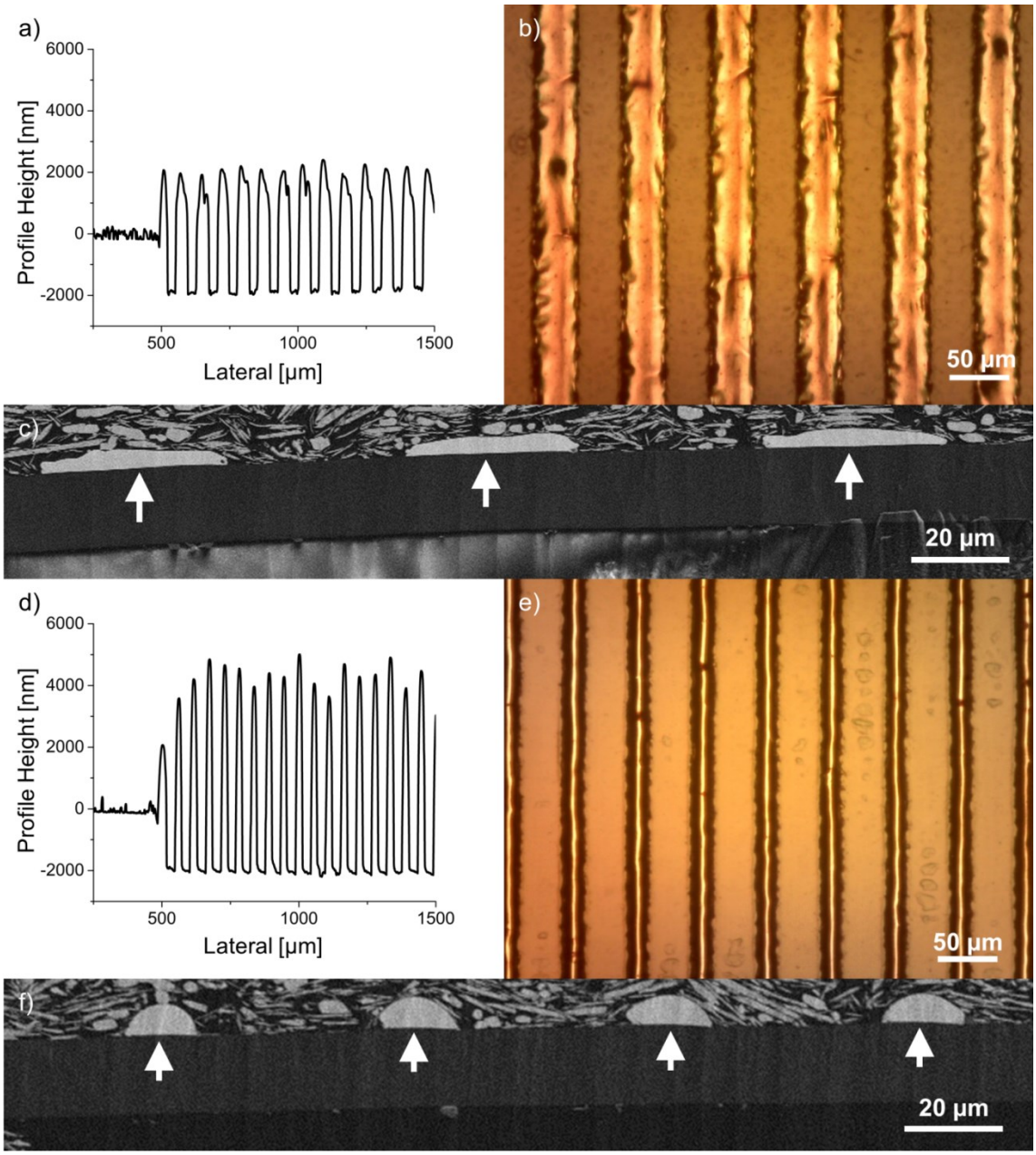

Figure 3.2: Line arrays dewetted from 1.6 μm thick bismuth under focused conditions. Lines are set at a pitch of 75 μm and 55 μm, measured center to center. For lines set at a pitch of 75 μm, features measured an average 3.85 μm in thickness. Characterization was conducted using a) profilometry, b) optical microscopy, and c) cross-sectional FESEM. Platelet structures are Ag from the conductive epoxy used for FESEM preparation. Dewetted Bi is demarked by the white arrows. Lines that are set at a pitch of 55 μm apart, center to center, showed an average height of 6.67 μm. Characterization of these lines was conducted using d) profilometry, e) optical microscopy, and f) cross-sectional FESEM. Again, dewetted Bi is demarked by the white arrows.

When the lines were set to pitches greater than 75 μm, the dewetted material of adjacent passes did not meld together as seen in arrays with pitches lower than 75 μm. Instead, these long-pitched arrays (**Figure 3.3**), presented as areas of exposed substrate bordered on both sides by two dewetted beads of greater thickness than that of the original film. Areas of unexposed, as-deposited film exist between the raised, dewetted material and remain unaltered by the heat generated by the laser. **Figure 3.3b** showcases a cross-section of such an array, where the dewetted material exists on the borders of the exposed substrate and is clearly thicker than the original film. In the image, white dash-lines are used to emphasize equivalent structures as seen from both a top-down perspective taken using an optical microscope and a cross-sectional perspective as seen by FESEM microscopy. In this respect, the raised, dewetted beads and the as-deposited film form pathways, which could be useful in microfluidics applications as they in effect, form micro-channels of conductive material.

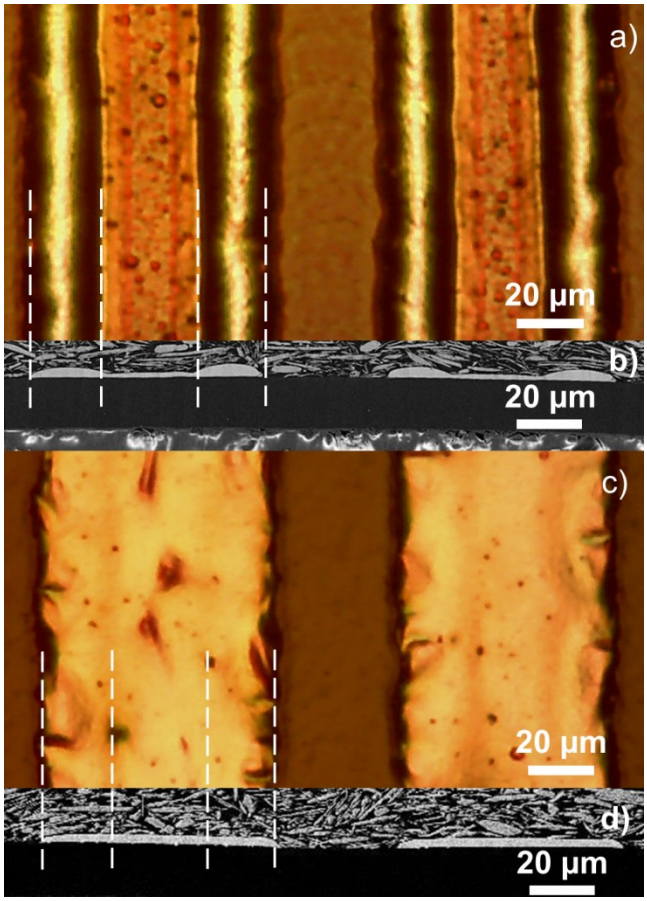

Figure 3.3: a) Optical images and b) FESEM cross-sections show the dewetted edges of a line array created with a 100 µm pitch distance. Dotted lines highlight the raised, dewetted beads and the connecting film in between. Platelet structures are Ag from the conductive epoxy used in sample preparation. c) Defocused exposure re-processing of the 100 µm pitch features, line arrays results in a uniform height profile as shown by d) FESEM. Dotted lines mark where dewetted beads previously existed.

If, however, a smooth cross-section is desired, it is possible to re-melt and flow the upper most layer of the unexposed area. Defocused reprocessing conditions led to an annealing effect on the dewetted beads. Initially, beads measured 3.4 µm in thickness. As the beads melted, they recombined with each other by flowing over and combining with the as-deposited section of film that connected them. In direct comparison to the cross-sections in **Figure 3.3b**, the re-melted features in **Figure 3.3d** exhibit a uniform cross-sectional height. White dash-lines demark the former locations of the raised, dewetted features. Inspection of the re-processed features will show a decreased

thickness in the former locations of the dewetted beads with a corresponding increase in thickness in the former as-deposited area. Profilometry scans reveal that the 3.4 μm thick beads were melted and reflowed over the 1.6 μm connecting film-section to form wide, relatively uniform lines that measured 2.6 μm thick.

3.3.2.2 Analysis of Material Retention

Profilometry was used to establish an accounting of the material volume before and after analysis and thus establish whether significant metal ablation occurred. Baseline is taken as the film surface, with measurements above and below baseline accounted as positive and negative respectively. Ideally, a process that conserves the material completely would result in positive and negative volume measurements cancelling out (**Figure 3.4d**). An isolated array of lines was scanned into a 1.6 μm thick Bi film deposited upon a par-C coated borosilicate glass slide. The par-C layer measured 25 μm thick. General lasing parameters for Bi were used. The entire array measured 2 mm x 2 mm and had a line pitch of 100 μm. Using successive, adjacent profilometer scans, a 3D model of the area was formed and analyzed. It was determined that a total of 4.52 X 10^6 μm^3 of material was displaced from the baseline. Of this volume, only 2.45 X 10^4 μm^3 or 0.5% of the displaced volume remains unaccounted for. This amount of unaccounted material falls within the measurement error of the profilometer and indicates minimal loss of the material into the vapor stream. Of note, the entire line array featured in **Figure 3.4** took only 0.316 seconds to complete, though much of this time is spent on timing delays between marking and mirror-positioning steps.

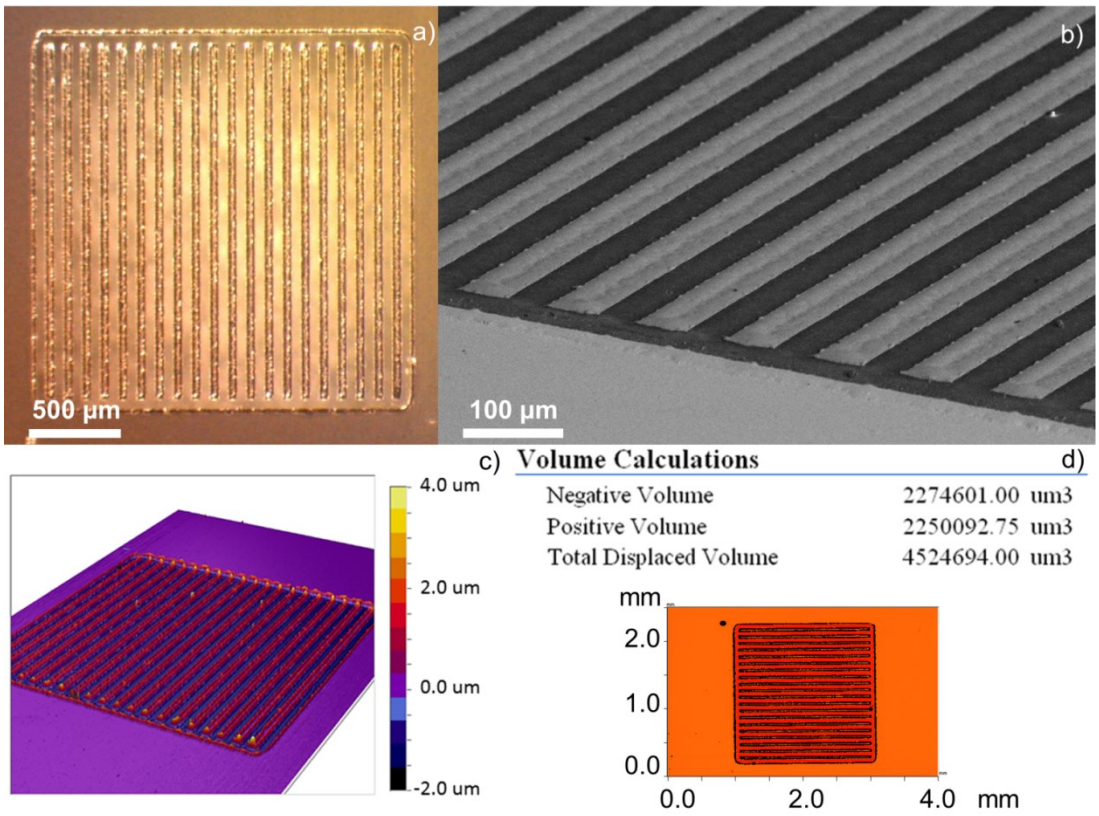

Figure 3.4: a) Optical and b) FESEM images of a self-contained line array measuring 2 mm x 2 mm. c) Profilometer scans were used to create a 3D height map of a dewetted line array. d) Volumetric analysis performed on the data reveals a 0.7 % discrepancy between the displaced positive and negative volumes, suggesting minimal material loss.

3.3.2.3 Back-Side Exposure

Choosing substrates with minimal absorption of NIR laser radiation allows for "back-side" processing of the target by transmission of the laser through the substrate. Minimal differences appear in the exposed areas of substrate created by front-side dewetting when compared to back-side dewetted samples. Profilometry on each set of samples reveals no significant difference in resulting cross-sectional thickness of the dewetted materials. Measurements made under optical microscopy reveal a consistent width of 30 µm for the dewetted areas regardless of exposure side. There was no considerable difference between the samples with respect to beam damage of the

substrates, nor was there any need to adjust laser exposure settings. The role of gravity in bismuth dewetting appears negligible at these length scales, as there was no significant increase to the average height under back-side dewetting. Conversely, gravity should play a much more significant role in the formation and shape of larger accumulations.

3.3.2.4 Accumulated Structures

Because the target material, in this case bismuth, melts and dewets from the substrate rather than ablating away, it can be directed and "pushed" into larger and larger out of plane structures. **Figure 3.5** presents a single line that was formed by scanning the laser across the surface of a 1.6 μm Bi film deposited upon a par-C covered surface. Pitch was set at 20 μm. At such a small pitch, the dewetting metal preferentially accumulated on the same side as the direction of advancing laser passes. For this example an initial set of 18 lines were dewetted with the lines advancing left to right. A second set of 18 lines were dewetted with the lines advancing from right to left. The second set of lines was placed in such a position so that the end of the final line would be positioned parallel to the end of the first set of lines. This caused the accumulated metal to combine and form one thick structure. The formed structure was itself a linear feature and measured 29.9 μm high – nearly 1900% as thick as the original 1.6 μm thick Bi film. With a width measurement of 56 um, the feature had an aspect ratio of 0.53:1.

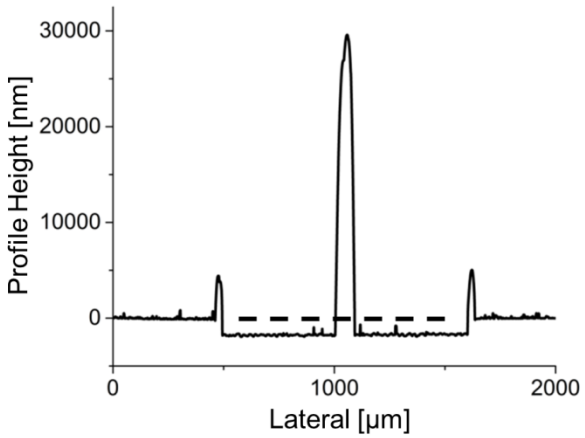

Figure 3.5: Profilometry of a built structure using successive laser passes. The dotted line provides a reference for the original height of the deposited film's surface relative to the substrate and is not a part of the measured profile.

Spiral dewetting of a 1.6 μm thick Bi film produced a single, large, near-spherical accumulation in the center of the spiral. The spiral pattern began at a radius of 1 mm, where every 360 degrees along the spiral path brought the laser spot 20 μm closer to the center. Marking along the spiral path stopped once the laser reached a radius of 150 μm. The resulting feature measured 79 μm tall – a total 4900% thicker than the original 1.6 μm thick film. The diameter of the accumulation was measured at 160 um, which gave an aspect ratio of 0.49:1. Total time for formation was 0.669 seconds. In total, the spiral pattern had 42.5 full rotations of dewetting passes combined into one large accumulation. Volumetric analysis was performed on this spiral dewet pattern. **Figure 3.6** shows the computed displaced volume as 9.6 X 10^6 um^3 with a total of 2.6 X 10^5 um^3 of unaccounted negative volume. With only a 2.8% discrepancy, this indicates that multiple laser exposure passes during the material "push" did not introduce significant amounts of ablation. Tin was also found to dewet easily under a spiral exposure. After laser exposure, the agglomerate at the center of the spiral measured 131 μm thick with a diameter of 200 um, which translates to an aspect ratio of 0.66:1and

a 8088% increase in thickness from the original 1.6 um thick film. Aspect ratios as high as 1.00:1 have been achieved via spiral geometry, however, such features were inconsistent in their adhesion and were prone to detachment from the substrate.

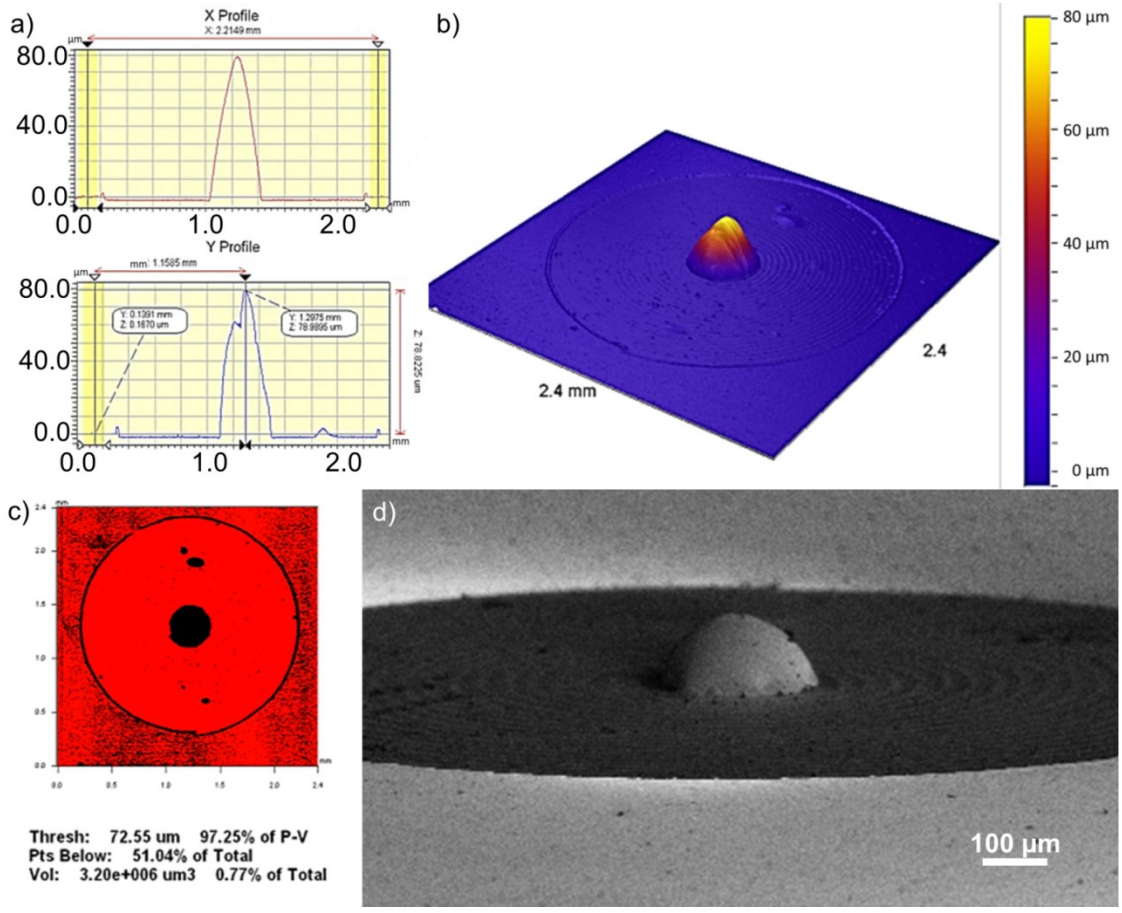

Figure 3.6: Profilometry data on a built mound of dewetted material. Successive passes constituted a spiral path. Scan data allowed for a) 2D and b) 3D height measurement. c) Volumetric analysis reveals a 2.8% discrepancy between positive and negative displaced material. d) FESEM tilted view of the dewetted mass confirming its three dimensional shape.

3.3.3 Complex Dewetting Geometry

3.3.3.1 Periodic Shapes

The galvanometer scanner system allows for much more detailed and complex patterning of the film. Measurements of the features formed from a 1.6 μm thick Bi film revealed triangular dimensions of 70 μm x 70 μm by 100 μm. At the designed dimensions, the features agglomerated together to make a continuous structure without any residual as-deposited film visible (**Figure 3.7a, 3.7b**). The thickness of the features was measured as 3.2 μm from a 1.6 μm film. Each feature remains disconnected from one another and exhibits very little variation in dimensions. Decreasing the feature size may be achieved by lower intensity beams or smaller diameter beams, where the area of high intensity laser energy is smaller than the current experimental setup. Additionally, lasers that operate at shorter wavelengths could be used to achieve smaller spot diameters than what is capable with the current laser.

3.3.3.2 Polygonal and Circular Accumulated Structures

Angles and corners could present a particular challenge for dewetting especially when building structures in height. Three basic geometrical shapes, triangle, circle, and square were fabricated and characterized. From a 1.6 μm bismuth film, features as high as 17 μm and as low as 10 μm were dewetted (**Figure 3.7c, 3.7d**). All shapes were formed with clean lines and excellent uniformity of width. An artifact from the geometry of the multiple passes causes a variation in the accumulated height along the length of the shapes parallel to the substrate. The highest areas of accumulation occur near vertices,

as the laser passes needed to create them converge and gather a greater amount of material than at the edges of the shape. In contrast, the circle remained consistent in height throughout the length. In theory, these height irregularities could be resolved by the aforementioned reflow technique where the material is exposed to low-intensity, defocused laser radiation.

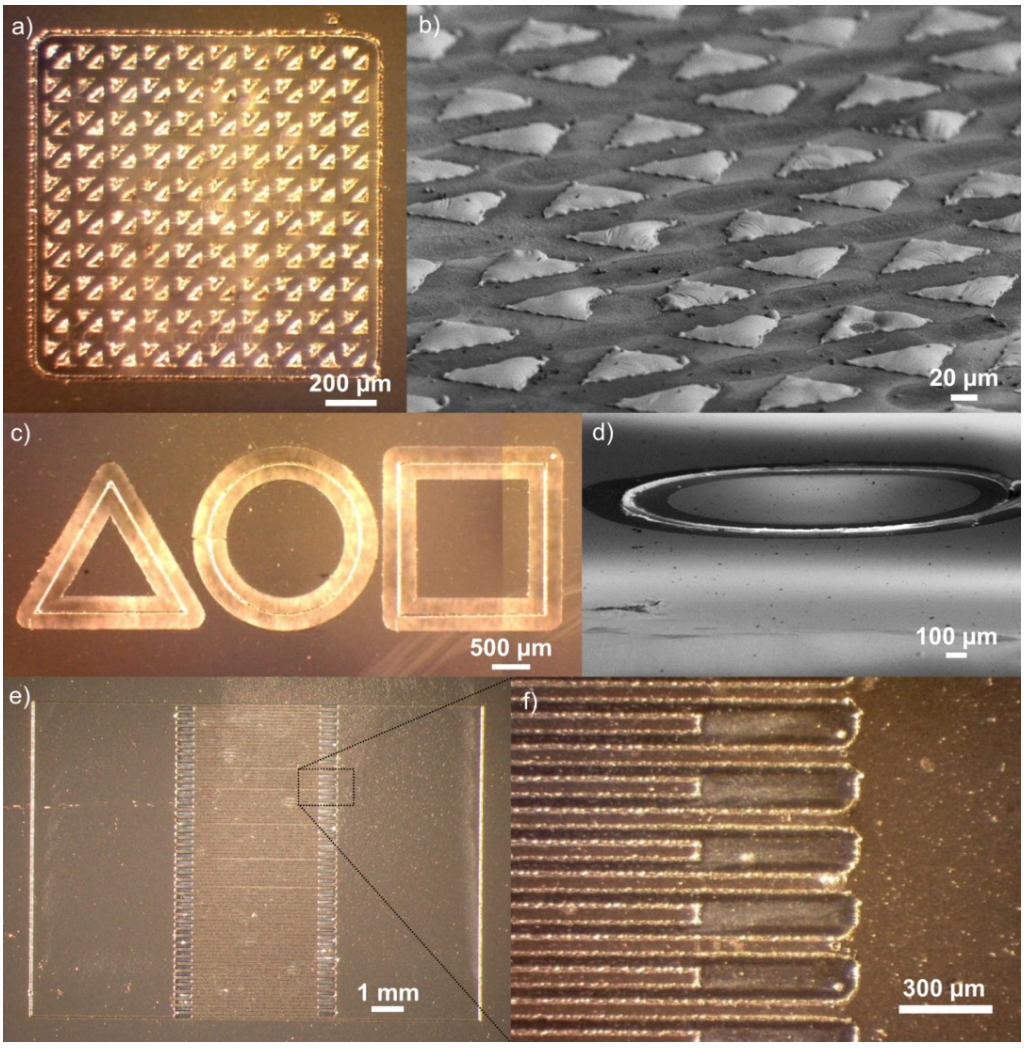

Figure 3.7: a) Periodic triangular structures dewetted from bismuth deposited onto a par-C covered glass slide. b) Triangular structures measured 70 µm x 70 µm x 100 µm. Each pass of the beam left a spacing of 30 µm of exposed par-C. c) Top-down view of polygonal and circular built structures. d) Tilted FESEM scans illustrate the height contrast between the deposited target film and the constructed features. e) An example of a possible inter-digit electrode system. f) Only one pass of the beam was necessary between each pair of electrode digits.

3.3.3.3 Electrically Isolated IDE

A large IDE array with a set pitch of 110 μm was dewetted from a 1.6 μm Bi film on a par-C coated borosilicate slide. The IDE had two electrode pads, each with 45 inter-digits. At the set pitch, the inter-digits measured 80 μm wide and had a space of 30 μm in between adjacent inter-digits and were used to explore the completeness of the dewetting process by electrical isolation tests (**Figure 3.7e, 3.7f**). A two point resistance test between the two electrode pads produces a resistance values exceeding the gigaohm capacity of the ohmmeter. Such isolation despite the relatively large interface length of each electrode pad indicates that each pass of the laser reliably initiates dewetting of the Bi film and that the dewetting action occurs to completion with no residual conductive material in the exposed space. Additionally, each electrode pad exhibited electronic isolation from the surrounding as-deposited film. For this example, each inter-digit is constructed with only one pass of the beam, indicating that complete dewetting occurs under the described general laser parameters. Alternative design geometries may allow further increase of the spacing in between each inter-digit by introducing additional laser passes between digits.

3.3.3.4 Complex Structures

To further evaluate the capabilities of the direct-write dewetting process two letters were chosen for further exploration and to combine elements of the individual techniques explored above. For the first letter – a capital “R” –a “push” approach was utilized. To this end, nine successive passes of the laser with a pitch of 20 μm were used to push material from the 1.6 μm Bi film outside of the “R” to create the general shape of the

letter. Nine passes from within the closed section of the “R” pushed material outward to finish the shape of the letter. The second letter chosen was a “U” and was designed as a small IDE. Each electrode pad boasted only two inter-digits – each curved to make the body of the letter. Cross-sectional views of the constructed features highlight the magnitude of the features in light of the deposited film. Despite the complex shape, electronic isolation is maintained. The resistance values measured across the electrodes exceeded the capacity of the gigaohm range of the ohmmeter, which indicates that neither the shape of “pushed” structures nor the shape of IDEs have an effect on the completeness of dewetting. Height values for the accumulated “R” structure measured at 10 μm in most locations, but rose to 17 μm in certain areas of the letter, most notably in the serifs of the “R.” The “U” IDE exhibited typical heights for beads created form a single laser pass and measured 3.2 μm high from the par-C substrate (**Figure 3.8**).

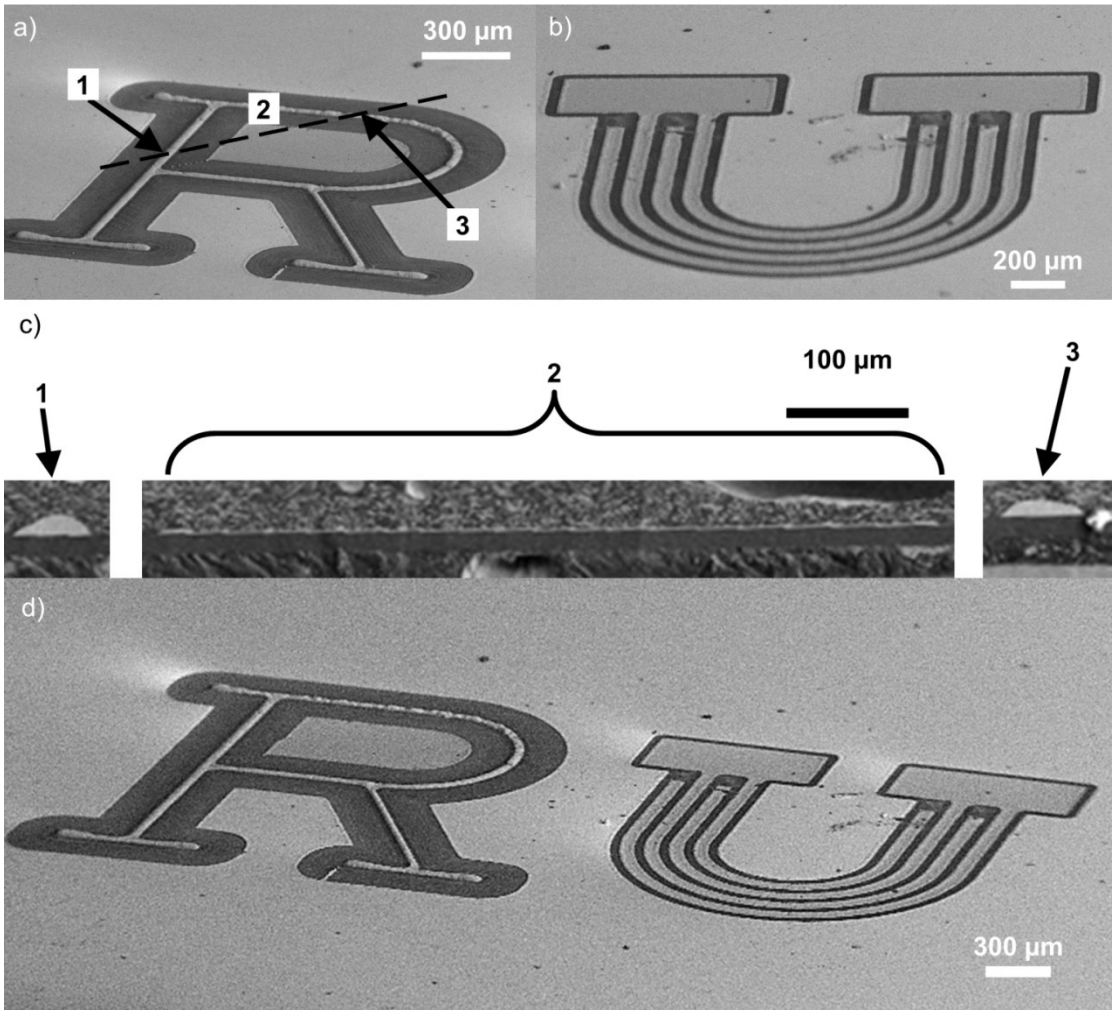

Figure 3.8: The complex shapes a) “R” and b) “U” are formed out of the target material. The dotted line demarks the approximate location of the cross-sectional cut; (1) and (3) identify the areas of accumulation; and (2) highlights an area of as-deposited bismuth. c) Within the cross-sectional image, (1) and (3) exhibit the thick accumulation that was created out of the thin film (2). d) Angled FESEM image of the dewetted features.

For reference, after preparing the target and drawing the scanner program, dewetting the bismuth into the “R” and the “U” feature only took 0.66 and 0.23 seconds to complete, respectively. While the general laser parameters for bismuth targets were adequate for demonstration purposes, scan timings and laser operation may be further optimized for faster through put of any particular geometry. This process easily lends itself to integration into existing industrial processes as only a simple gas blanket is needed to prevent oxidation and ensure proper dewetting of the target material.

3.4 Discussion

This manuscript presents evidence that a new technique based on directed-dewetting can result in rapid (ms) fabrication of complex metal features in and out of plane with no residual material. The technique shows equal viability when laser energy is transmitted through the substrate thus enabling scenarios where encapsulation can be performed before structures are formed. Limitations to this technique depend on the choice of substrate, laser, and target material. Inorganic substrates of appropriate surface energies and absorption behavior will enable the application of this technique to higher melting temperature metals such as Pt without substrate damage. More efficient coupling of the laser energy to metallic films can be induced by the use of shorter wavelength lasers; however, the higher energies of these lasers present additional challenges to prevent selective ablation of material due to difference in intrinsic absorption. The range of processing parameters conducive to directed-dewetting of metallic films is narrow and is affected not only by the fundamental properties of the target material, but also by the quality and size of the film itself. Alternative methodologies such as surface modification are well known processes that can increase laser absorption considerably and can also lead to significant modification of the apparent surface energies. Feature size can be reduced considerably with the use of finer spot sizes enabled by the use of shorter wavelength laser radiation. The use of thinner films may allow smaller-scale features; however theoretical limits do exist and will be discussed in a forthcoming manuscript.

While the technology introduced here is by no means perfected, such methods may represent an alternative fabrication pathway for complex metal structures on flexible substrates. In addition, the technique offers a unique additive pathway to form structures

of considerable height from thin films without the waste of material and complex mask formation.

3.5 References

1. Yagi I, Tsukagoshi K, Aoyagi Y. Direct observation of contact and channel resistance in pentacene four-terminal thin-film transistor patterned by laser ablation method. *Appl Phys Lett*. 2004;84:815. doi: 10.1063/1.1645316.
2. Cho G, Noh J, Sung H, et al. Patterned si thin film electrodes for enhancing structural stability. *Nanoscale Research Letters*. 2012;7(20):5. doi: 10.1186/1556-276X-7-20.
3. Tseng S, Hsiao W, Huang K, Chiang D, Chen M, Chou C. Laser scribing of indium tin oxide (ITO) thin films deposited on various substrates for touch panels. . 2010;257:1487-1494. doi: 10.1016/j.apsusc.2010.08.080.
4. Gecys P, Raciukaitis G, Miltenis E, Braun A, Ragnow S. Scribing of thin-film solar cells with picosecond laser pulses. *Physics Procedia*. 2011;12:148. doi: 10.1016/j.phpro.2011.03.116.
5. Ruthe D, Zimmer K, Hoche T. Etching of CuInSe2 thin films - comparison of femtosecond and picosecond laser ablation. *Appl Surf Sci*. 2005;247:452.
6. Henderson RD, Guijt RM, Andrewartha L, et al. Lab-on-a-chip device with laser-patterned polymer electrodes for high voltage application and contactless conductivity detection. *Chemical Communications*. 2012;48:9287-9289.
7. Chin CD, Linder V, Sia SK. Commercialization of microfluidic point-of-care diagnostic devices. *Lab on a Chip*. 2012;12:2118-2134. doi: 10.1039/c2lc21204h.
8. Glang R, Gregor LV. Generation of patterns in thin films. In: Maissel LI, Glang R, eds. *Handbook of thin film technology.* Hopewell Junction, NY: IBM Corporation Components Division; 1970:7.66.
9. Levy DH, Ellinger CR, Nelson SF. Metal-oxide thin-film transistors patterned by printing. *Applied Physics Letters*. 2013;103:043505. doi: 10.1116/1.3670748.
10. Gentili D, Foschi G, Valle F, Cavallini M, Biscarini F. Applications of dewetting in micro and nano technology. *The Royal Society of Chemistry*. 2012;41:4430-4443. doi: 10.1039/c2cs35040h.
11. Sharma A, Ruckenstein E. Energetic criteria for the breakup of liquid films on nonwetting solid surfaces. *Journal of Colloid and Interface Science*. 1990.
12. Stange TG, Evans DF. Nucleation and growth of defects leading to dewetting of thin polymer films. *Langmuir*. 1997;13(16):4459-4465.
13. Xie R, Karim A, Douglas JF, Han CC, Weiss RA. Spinodal dewetting of thin polymer films. *Physical Review Letters*. 1998;81(6):1251-1254.
14. Pandit AB, Davidson JF. Hydrodynamics of the rupture of thin liquid films. *Journal of Fluid Mechanics*. 1990;212:11-24.
15. Redon C, Brochard-Wyart F, Rondelez F. Dynamics of dewetting. *Physical Review Letters*. 1991;66(6):715-719.
16. Bischof J, Scherer D, Herminghaus S, Leiderer P. Dewetting modes of thin metallic films: Nucleation of holes and spinodal dewetting. *Phys Rev Lett*. 1996;77(8):1536-1539.
17. Favazza C, Kalyanaraman R, Sureshkumar R. Robust nanopatterning by laser-induced dewetting of metal nanofilms. *Nanotechnology*. 2006;17:4234.
18. Krishna H, Sachan R, Strader J, Favazza C, Khenner M, Kalyanaraman R. Thickness-dependent spontaneous dewetting morphology of ultrathin ag films. *Nanotechnology*. 2010;21:155601.
19. Riedel S, Schmotz M, Leiderer P, Boneberg J. Nanostructuring of thin films by ns pulsed laser interference. *Appl Phys A*. 2010;101(2):309-312.

20. Riedel S, Leiderer P, Scheer E, Boneberg J. Pulsed laser interference patterning of metallic thin films. *Acta Physica Polonica A*. 2012;121(2):385-387.
21. Kuznetsov A, Koch J, Chichkov B. Nanostructuring of thin gold films by femtosecond lasers. *Appl Phys A*. 2009;94:221-230.
22. Rack PD, Guan Y, Fowlkes JD, Melechko AV, Simpson ML. Pulsed laser dewetting of patterned thin metal films: A means of directed assembly. *Appl Phys Lett*. 2008;92:223108.
23. Fowlkes JD, Kondic L, Diez J, Wu Y, Rack PD. Self-assembly versus directed assembly of nanoparticles via pulsed laser induced dewetting of patterned metal films. *Nano Lett*. 2011;11:2478-2485.
24. Torkamany MJ, Hamedi MJ, Malek F, Sabbaghzadeh J. The effect of process parameters on keyhole welding with a 400 W nd : YAG pulsed laser. *Journal of Physics D: Applied Physics*. 2006;39:4563-4567.
25. Jeong YS, Ratier B, Moliton A, Guyard L. UV-visible and infrared characterization of poly(p-xylylene) films for waveguide applications and OLED encapsulation. *Synth Met*. 2002;127:193.
26. Gusarov A, Doyle D, Glebov L, Berghmans F. Radiation-induced transmission degradation of borosilicate crown optical glass from four different manufacturers. *Optical Engineering*. 2007;46(4):043004. doi: 10.1117/1.2722322.
27. Stalder AF, Kulik G, Sage D, Barbieri L, Hoffmann P. A snake-based approach to accurate determination of both contact points and contact angles. *Colloids Surf Physicochem Eng Aspects*. 2006;286:92-103.

4 Direct-Write Dewetting of High Melting Temperature Metals on Flexible Substrates

4.1 Introduction

Unlike traditional integrated circuit devices, MEMS and microfluidic devices encompass a greater variety of physical designs and purposes. To enable the wide range of designs, the patterning processes used in MEMS construction must be equally as varied and versatile. A great deal of research has been conducted regarding the dewetting of micro-, meso-, and nano-scale thin films because of technique's potential to create periodic and free-form film structures without the need for complicated deposition, masking, and etching protocols. Along with the basic, randomized dewetting regimes that exhibit thickness-dependent periodicities[1-4], a number of researchers have conducted studies on methods to impose user-defined length scales and spatial ordering to the dewetting events. Such imposed spatial ordering can be achieved via probe-assisted perturbations[5], stamp generated dewetting[6-8], pre-patterned surfaces[9,10], and a number of other methods.

Dewetting of a liquid film occurs when the spreading pressure of a film (as determined by the surface tensions in the system) is overcome by the long range intermolecular forces. The point at which a thin liquid film is may spontaneously dewet is designated the critical height as shown in **Equation 1**, where λ is the capillary length and θ_e is the equilibrium contact angle of the liquid on the solid. In this regime, films may be metastable or unstable.[11] Dewetting proceeds via two mechanisms: nucleation and growth of holes, or spinodal dewetting. The former case may be triggered by defects in the substrate while the latter case is characterized by the increased amplitude of

capillary waves within the film. Solid metallic thin films are metastable as well, especially when deposited upon low surface energy substrates, but will often require additional energetic input before dewetting is observed. This can involve raising the system temperature past the melting point of the metal; however, dewetting may be observed in films while in the solid phase.[12-14] Past studies have shown that dewetting of metallic films can be induced by use of laser input from both defocused and focused sources.[15-17]

$$h_c = 2\lambda \sin {}^{\theta_e}/_{2} \quad (\mathbf{1})$$

Singer, et al., recently demonstrated that focused 532 nm laser radiation can be used in conjunction with an X-Y movement stage to create dewetted structures of polystyrene films deposited upon silicon substrate.[18] Direct-write patterning and structure formation of low melting temperature metal films on polymer substrates through the use of a high speed scanning laser has been recently demonstrated by our group.[19] More specifically, bismuth and tin films deposited upon parylene-C (Par-C) coated glass slides were patterned using a focused 1070 nm laser and high-speed galvanometer scan system. During the irradiation process, the films experienced a localized dewetting event that was initiated by melting and thermocapillary flow in the heated area. As the laser heats the target area, a thermal gradient is formed beginning at the center of the focal point and radiating outward. A concurrent and parallel surface tension gradient forms in this area due to the variation of surface tension with temperature, which results in an overall Marangoni flow away from the center and outward. **Equation 2** details the tangential thermocapillary force balance when a temperature gradient is present. The process is diagramed by **Figure 4.1**, where the dewetting event is separated into three main regions: heating, thermocapillary flow, and hole growth. Choice of laser

wavelength, target material, and substrate material all play a large role in the viability of this technique to effectively create dewetted structures without damaging the underlying substrate. This is of particular importance when using polymer substrates with metal targets since the melting point of the metal film is so high.

$$\frac{d\gamma}{dT}\nabla T = \nabla\gamma = \vec{\tau}\cdot\hat{n} \qquad (2)$$

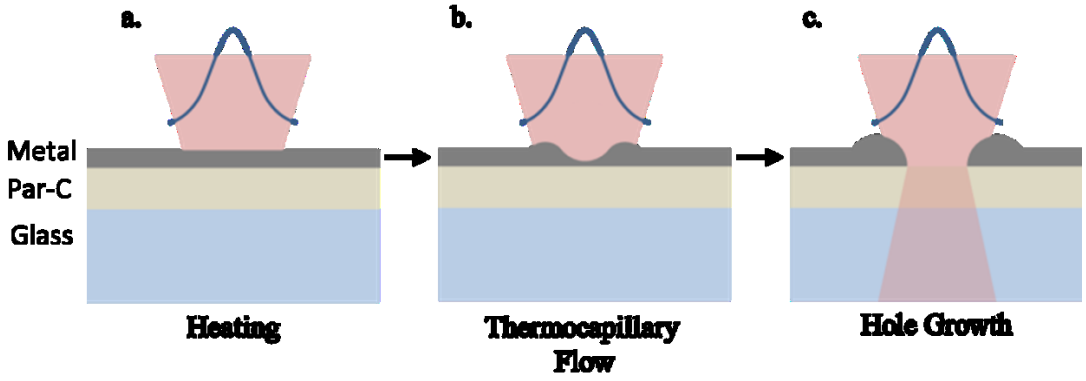

Figure 4.1: Mechanism for direct-write dewetting using focused NIR laser radiation

In the previous examples of thermocapillary dewetting of metals, the film targets were characterized by relatively high absorptivity in the near-infrared range and melting points comparable to the softening/degradation points of polymers such as polytetrafluoroethylene (PTFE), polyimide (PI), and parylene-C (Par-C). Many of these polymers are used in the micro-electronics and MEMS industries for their mechanical flexibility, high temperature thresholds, and their barrier properties[20-22]. Bismuth, tin, and their alloys are used in thin film configurations in similar applications such as sensors, electrochemical cells, and micro-soldering. For applications that require a greater degree of thermal conductivity, electrical conductivity, or heat resistance, it is more practical to use thin film compositions involving transition metals such as nickel, gold,

silver, or chromium. Therefore, it is advantageous to explore and develop alternative processing techniques for patterning high melting point metals – especially for use on polymer substrates. With a melting point of 1455°C, nickel's thermal, electrical, and optical properties (**Table 4.1**) are typical of the Group VIIIB elements. Nickel thin films have been used in sensors[23] and electrochemical cells[24], and have the property of being relatively absorptive in the NIR range. Conversely, Group IB elements, such as silver, are characterized by high reflectivity in the NIR range, while boasting the highest thermal and electrical conductivities of the transition metals. To expand the capabilities of the directed scan dewetting technique past bismuth and tin, both nickel and silver thin films were created as the most challenging examples and subsequently patterned on polymer Par-C substrates. The effects of the higher melting temperatures were investigated with respect to any possible damage to the underlying substrate. Additionally, layered films were studied as a means to enhance the effects of NIR laser radiation and bypass the high reflectivity of the silver thin films.

Table 4.1: List of relevant materials properties

Material	M.P. [°C]	Surface Energy/Tension [mJ/m^2] Solid	Liquid	Inherent Absorptivity at 1064 nm [%]	Thermal Conductivity [W/(m*K)]	Electrical Resistivity [Ω*m]
Borosilicate Glass	821 [33] (soften)	253.0 [37]	-	<3 [38]	1.05	$8x10^{8}$
Parylene-C	290 [34]	19.6 [34]	-	<15 [36]	0.082	$1x10^{15}$
Polyimide (Kapton)	400 (soften)	53	-	<10 [35]	0.15	$1.5x10^{15}$
PTFE (Teflon)	327	20	-	<10 [35]	0.26 [25]	$1x10^{23}$ x)
Bismuth	271.5 [25]	446 [32]	378 [32]	32 a)	7.87 [25]	107 $x10^{-8}$ [25]
Tin	231.93 [25]	661 [32]	560 [32]	54 a)	66.6 [25]	11.5 $x10^{-8}$ [25]
Nickel	1455 [25]	2080 [32]	1763 [32]	28 a)	90.7 [25]	6.93 $x10^{-8}$ [25]
Silver	962 [25]	1086 [32]	920 [32]	< 5 a)	429 [25]	1.587 $x10^{-8}$ [25]

a) Calculated from optical constants

4.2 Experimental

Pre-cleaned borosilicate glass microscope slides were coated with a 22 μm thick layer of par-C via CVD methods. These coated slides served as substrates for a number of single and multi-layered metal films. Nickel films were sputtered at thicknesses of 320 nm and 640 nm. Silver films were evaporated onto the described substrates at a thickness of 405 nm. Multi-layered films were created by evaporating 45

nm of bismuth onto 405 nm of silver. Additional multi-layered films were created by sputtering 45 nm of nickel onto 405 nm of silver.

All film processing was conducted with an integrated laser processing system consisting of a near-infrared (NIR) laser (SPI redPOWER R4-HS), an in-line camera system (uEye GigE), a galvanometer-driven scanner (Scanlab IntelliSCAN 20) with an f-theta telecentric lens (115 mm effective focal length) and a custom-made sample stage. The sample stage allowed for manual adjustment of the z-axis as well as tilt-leveling about the x- and y-axis. The telecentric optics ensured consistent laser intensity via a flat focal plane. Laser exposure was conducted in both pulsed-mode and in continuous-wave exposure, depending on the chemistry of the target film and substrate. While in pulsed-mode, the laser ran at 10 W with pulse lengths of 2.5 μs and an exposure frequency of 100 kHz. The beam waist measured ~34 μm in diameter under these conditions as determined by **Equation 3**, where M^2 is the beam quality factor (< 1.1), λ is the wavelength (1070 nm), f is the effective focal length (115 mm), r_i is beam radius as it enters the lens (2.535 mm), and r_0 is the radius of the beam at the focal point.

$$r_0 = \frac{M^2 \lambda f}{\pi r_i} \quad (3)$$

With this beam spot, the processing parameters resulted in a pulse fluence of 2.75 J/cm^2. At speeds of 0.2 m/s, the normalized scan energy was calculated to be 12.5 J per meter scanned. Under continuous wave (CW) operation, scan speeds were increased an order of magnitude to 2.0 m/s to compensate for the lack of cooling between pulses. With an output power of 25 W, the normalized scan energy remained 12.5 J per meter scanned for CW operation, but retained higher laser intensities to overcome high reflectivity barriers, such as the case for silver films. Layered films were

dewetted with a laser power of 10 W and speeds of 1 m/s and 3 m/s, which resulted in scan energies of 10 and 3.33 J per meter scanned respectively.

4.3 Results

4.3.1 Directed-Dewetting

A typical set of metallic lines fabricated from 640 nm nickel thin films on Par-C substrates are pictured in **Figure 4.2**. 40 and 100 μm pitch lengths were scanned into the films revealing dewetted trenches and bordering ridges as a result of the movement of the molten metal along the polymer surface. Associated profilometry scans of the two sets of lines reveal the characteristic film-ridge-trench-ridge-film profile similar to that observed in earlier studies focused on low melting temperature bismuth and tin films[19]. The low trenches represent the surface of Par-C exposed after laser induced dewetting of the molten Ni. Morphology on the border of the trenches created by the displaced material is, in large part, uniform; however, there are signs of decomposition of the ridge into a series of beads.

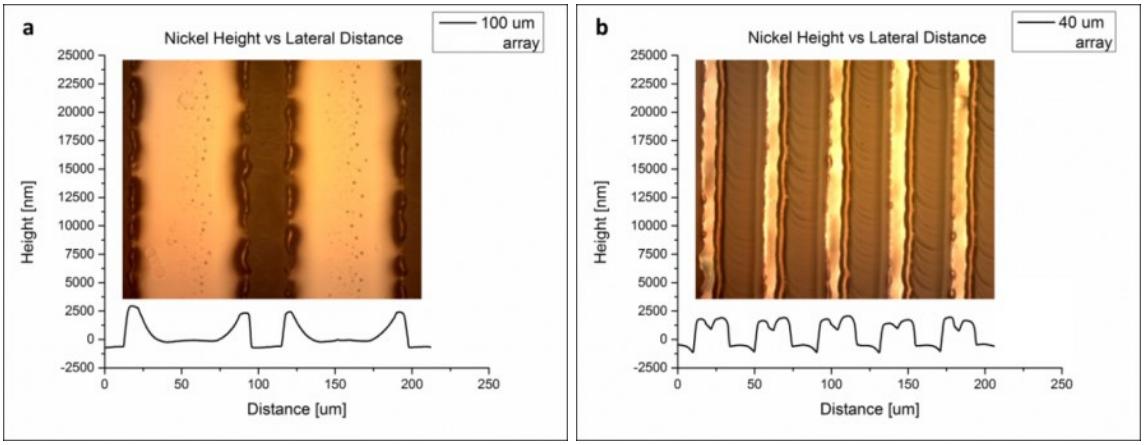

Figure 4.2: Arrays of dewetted ridges and profilometry data for pitch lengths of a) 100 μm and b) 40 μm. Optical micrographs have been aligned with the profiles for comparison.

Three-dimensional maps (**Figure 4.3**) give evidence that the nickel melts and dewets from the surface rather than experiencing an ablation event. Any "positive" volume displaced above the baseline surface of the nickel film is compared to the "negative" volume displaced below it. For the 100 μm pitched array, only 6.1% of the negative volume remained unaccounted for, suggesting that the vast majority of the nickel film is conserved.

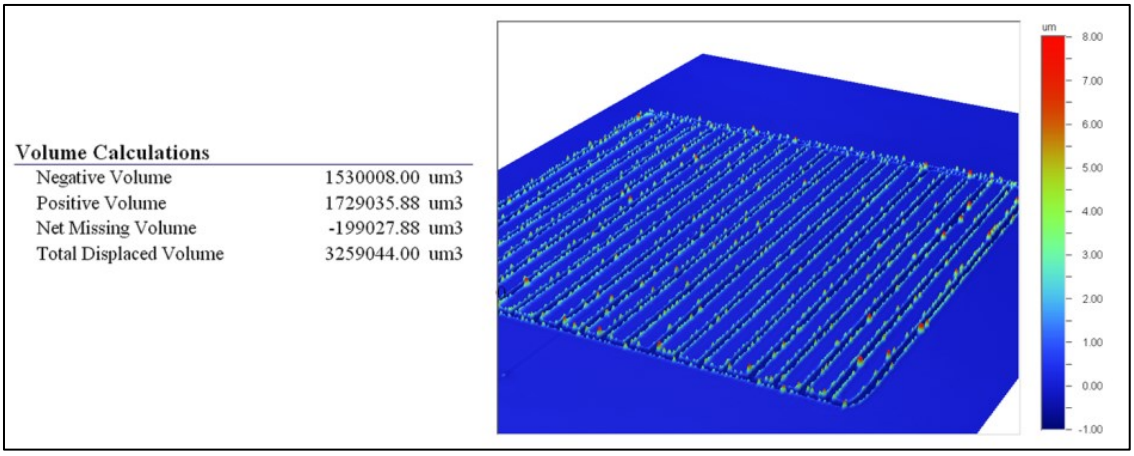

Figure 4.3: 3D mapping of nickel linear array with a spacing of 100 μm. Of the accounted volume, 6.1% negative space remains unaccounted for.

Cross-sectional samples of the lines are analyzed using field emission scanning electron microscopy (FESEM) in **Figure 4.4**. The 100 μm array reveals the true shape of the nickel films after the dewetting action. Each FESEM image displays an area of exposed substrate surrounded by an accumulation of material. The polymer substrate takes on a dark contrast below the film features. The reader is directed back to **Figure 4.1c** for a general schematic of the created structure. Nickel films appear to undergo a delamination event before melting. Thus, as the nickel melts and dewets away from the center of the beam spot, the metal will solidify underneath a section of delaminated film, rather than sitting on top. This is in sharp contrast to the morphology of other dewetting thin film examples.[19,26] As the pitch is lowered to 40 μm in **Figure 4.4b**, the accumulation becomes symmetrical around the non-melted film to form a "dumbbell" cross-section created out of two adjacent laser scans. Both cross-sections exhibit porosity in the dewetted ridges. Such porosity is seen for both sets of linear arrays and most likely arises from slight degradation or outgassing of the polymer at the interface. An additional source may be present in impurities found at the surface of the parylene that are vaporized during the dewetting. Indeed, the parylene may be preserved from the intense heat of melting Ni by the presence of a thermally insulating gas, similar in consequence as the Leidenfrost effect.[27] Indeed such an effect may be responsible for the prior mentioned "delamination" of the film from the surface prior to melting. Furthermore, the observed delamination of the dewetting Ni ensures that conduction down into the polymer from the hottest processed areas is limited.

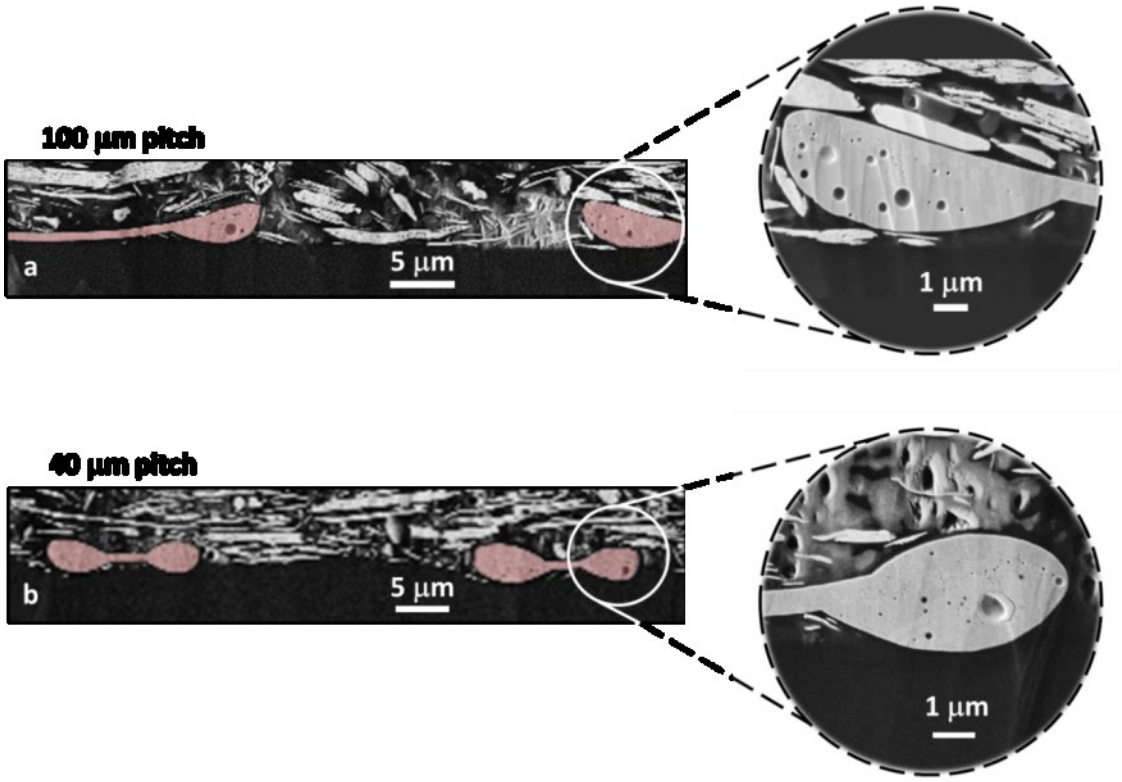

Figure 4.4: Red color-enhanced, cross-sectional images of nickel dewetted arrays for a) 100 μm and b) 40 μm pitched arrays. The conductive epoxy used to pot the samples contained flakes of silver, which appear above and around the film structures.

Preservation of the underlying polymer substrate emerges as one of the major hurdles in achieving well defined dewetted structures on metals deposited on polymer substrates. This is especially true of metal films of high melting point since Par-C has a relatively low degradation temperature of 290 °C compared to the 1455 °C melting point of nickel; therefore, there is a large risk of substrate degradation during the dewetting process. While optical micrographs do not show any apparent charring or degradation within the exposed polymer, some deformation of the substrate surface may be expected due to the polymer's thermoplastic behavior, and evidence of some vaporization has been noted above. Profilometry scans on the 40 μm pitched array (**Figure 4.2b**) demonstrate deformation of the polymer surface as evidenced by a

noticeable dip in the trench areas between the dewetted nickel ridges. The same sharp dip in the parylene is observed in the cross-section of the same array (**Figure 4.4b**). Similar deformations are not observed in the profiles of the 100 μm pitched array (**Figure 4.2a**); however the small amounts of delamination near the dewetted ridge contribute to the positive/negative volume discrepancy cited earlier. As the laser spot is scanned across the surface of the nickel, a portion of the generated heat is transferred down to the polymer substrate locally, but is dissipated by conduction into the bulk of the Par-C and neighboring Ni film. In cases where the laser is scanned in tighter pitches, higher concentrations of heat accumulate, which ultimately exposes the Par-C to higher peak temperatures. Increasing the wait time between laser passes, or alternating scans may provide a greater amount of cooling; however, a more effective solution would be to use a power setting lower than the minimum allowed by the present laser system. These effects of thermal transport could easily be modeled to optimize processes.

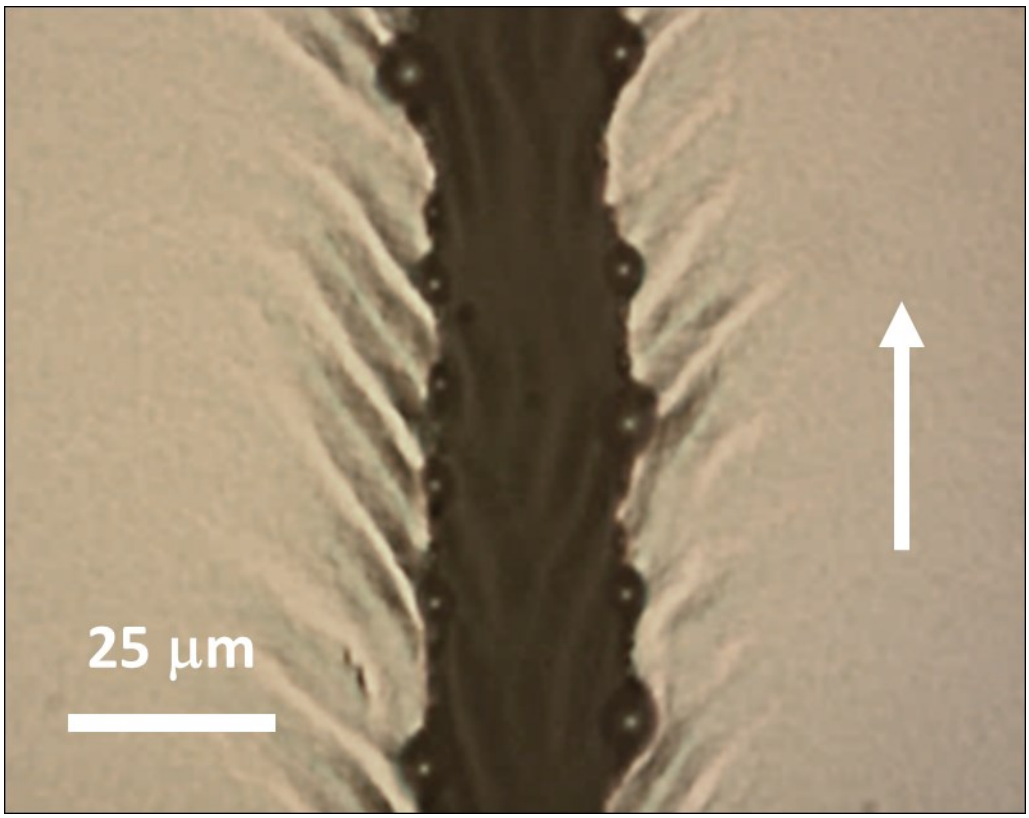

Figure 4.5: Optical microscopy of Ag film on the Par-C polymer substrate. The laser scan of the dewetted Par-C surface appears along the dark center with ridges of dewetted metal along the edge. The beam was scanned in the direction of the arrow. Dewetted silver ridges exhibit instability and degrade into discrete beads.

Exposing silver films in similar fashion lead to an equivalent melt and dewet event. While silver has a relatively high melting point in relation to the Par-C substrate, these films also exhibit higher inherent reflectivity (> 95%) at the incident laser wavelength versus nickel (< 75 %). In addition Ag exhibits the highest thermal conductivity of all the metals. To compensate, the laser operates in continuous wave mode at a power of 25 W, which delivers higher incident intensity on the target film. The intensity overcomes the reflectivity and allows melting and dewetting to take place. High speed scanning prevents destruction of the polymer substrate after the dewetting event, the result of which is displayed in **Figure 4.5**. The beading seen along the trench's bordering ridge is indicative of instability within the ridge that grows before solidification of the film. Similar

instabilities have been observed in the rims of dewetting polymer films and are analogous to the Plateau-Rayleigh instability describing the break-up of columns of liquid into individual drops.[28-30] In this scenario, the dewetted ridges may be modeled as half of a column of liquid that experiences capillary fluctuations in the surface of the liquid. As Choi and Newby pointed out in their investigations, the growth rate of the rim instability can be described using **Equation 4**.

$$q = \frac{\gamma_m}{6R_0\mu_l} \quad (\mathbf{4})$$

Where γ_m is the surface tension of the liquid, R_0 is the radius of the hole formed, and μ_l is the viscosity of the liquid. From this, they were able to deduce a positive correlation between the dynamic contact angle of the receding film and the growth rate of the perturbations. Contact angles of the dewetted silver ridges range between 130° and 155°. This agrees with the high surface tension of silver as described in **Table 4.1**. A similar Rayleigh analysis would suggest that the growth rate of perturbations within the silver ridges is larger than the rate exhibited by bismuth or tin films deposited upon Par-C.[19] The large thermal conductivity of the silver may provide a secondary explanation. As the beam travels, there exists a thermal gradient both perpendicular and parallel to the direction of scanning. This trailing gradient is most pronounced in the silver, as the heat quickly conducts throughout the unaffected film and solidifies behind the beam. Such gradients have been observed and studied in macro scale, high-speed welding of metal plates using laser with beam qualities on par with the current system.[31]

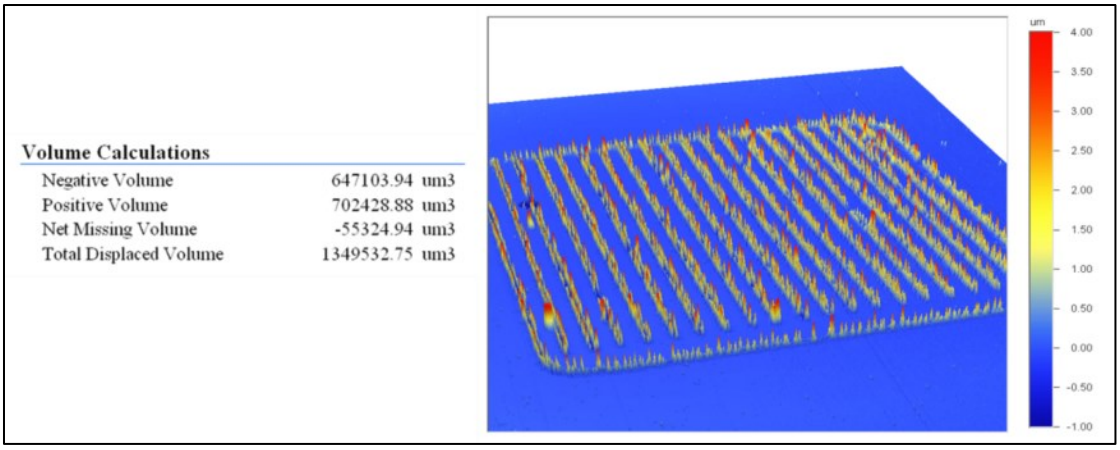

Figure 4.6: Accumulation of silver film ridges around laser exposed trenches. Accounting of the displaced volume reveals 4.1% of the negative space remains unaccounted.

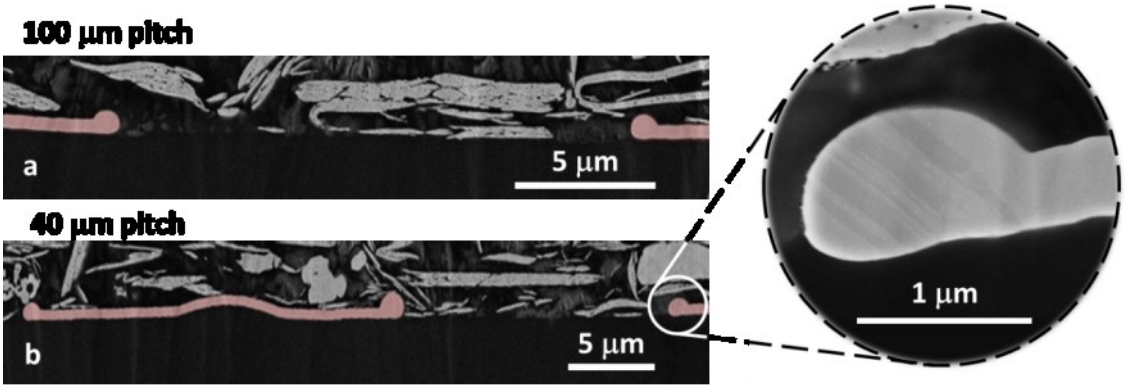

Figure 4.7: Red color-enhanced, cross-sectional images of dewetted ridges of Ag for a) 100 μm and b) 40 μm pitched arrays.

Accounting of the volume displacement (**Figure 4.6**) reveals that only 4.1% of the negatively displaced volume is left unaccounted but can be explained by small shadowing effects created by the spherical accumulations that are observed along the dewetted silver ridges as well as measurement variation of the profilometer. Cross sections of the silver are presented in **Figure 4.7**. Unlike the previous film, the dewetted ridges show no signs of porosity or underlying delamination. The absence of the pores may be a result of the lowered melting point and higher thermal conductivity of the silver,

thus reducing the heat load on the underlying substrate and eliminating any vaporization at the metal-polymer interface. Furthermore, the increased thermal conductivity quickly dissipates the high heat concentration at the exposure point, leading to less substrate degradation. In similar fashion to the pure nickel films, there is no visible destruction of the Par-C substrate – even in the face of much higher laser intensity.

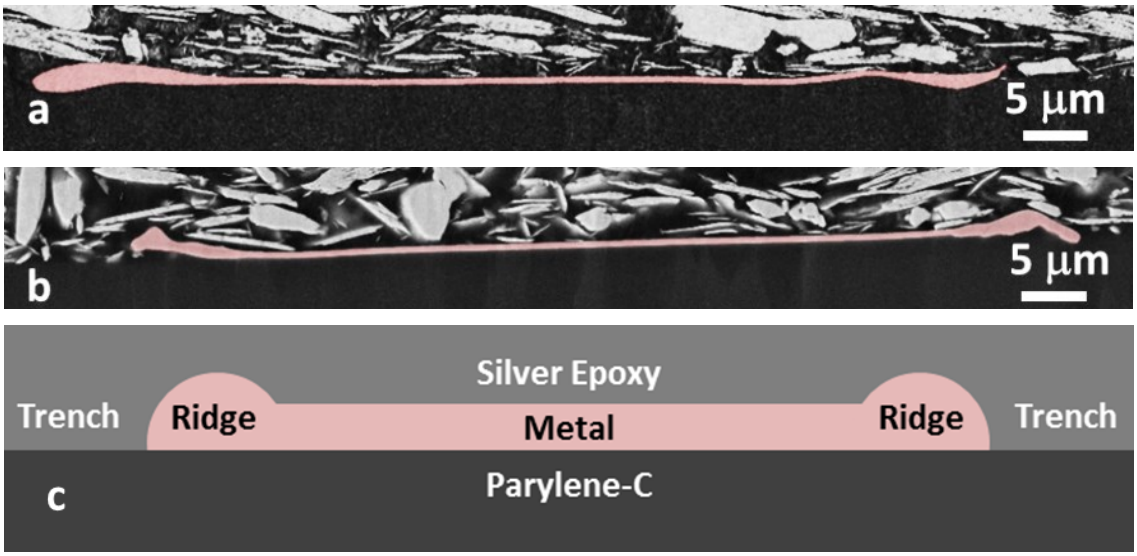

Figure 4.8: Color enhanced, dewetted ridge profiles of 100 μm pitched line arrays in a) Bi-Ag and b) Ni-Ag layered target films. A diagram of the c) film structure has been provided for clarity.

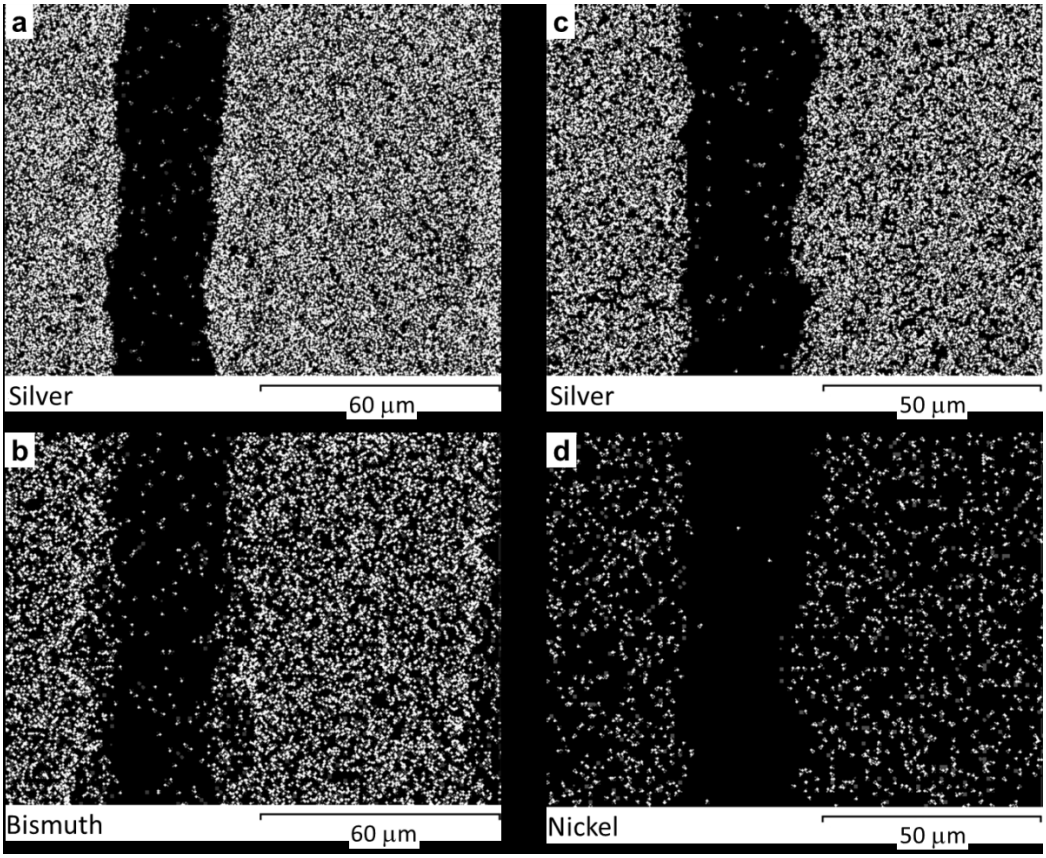

Figure 4.9: Elemental maps created from multi-layered a) bismuth and b) silver films compared to elemental maps created from multi-layered c) nickel and d) silver films.

To avoid the need for high intensity operation required by the poor absorption of the Ag films to the laser energy, some silver films were coated with a 45 nm absorption layer of bismuth or nickel to lower their reflectivity. Adsorption layers were kept to 10% of the thickness of the base silver film. Line arrays with a pitch of 100 μm were dewetted into both types of layered films. Cross-sectional FESEM images can be seen in **Figure 4.8**. Similarities can be seen between the two types of layered films. Ridge formations appear to flatten and widen to a greater degree, but still exhibit larger cross-sectional heights compared to the original film height. Using energy dispersive x-ray spectroscopy (EDS), elemental maps of the metal films are conducted. **Figure 4.9** displays top-down views of both varieties of multi-layered films. For the Bi-Ag films, there is a clear bismuth

deficiency alongside the trenches, within the ridges. Conversely, the Ni-Ag films show no nickel deficiency near the exposed areas. This is explained via the difference in melting temperature of the two absorption layers. Bismuth would tend to melt and undergo thermocapillary action before the underlying silver melts. Additionally, some of the bismuth may be vaporized, however, this is unlikely since a good deal of the heat generated in the bismuth and conducted down into the underlying silver film. For the nickel absorption layer, the underlying silver will tend to melt prior to any thermocapillary action of the nickel. Thus, we expect movement of the silver film without mixing of the nickel film.

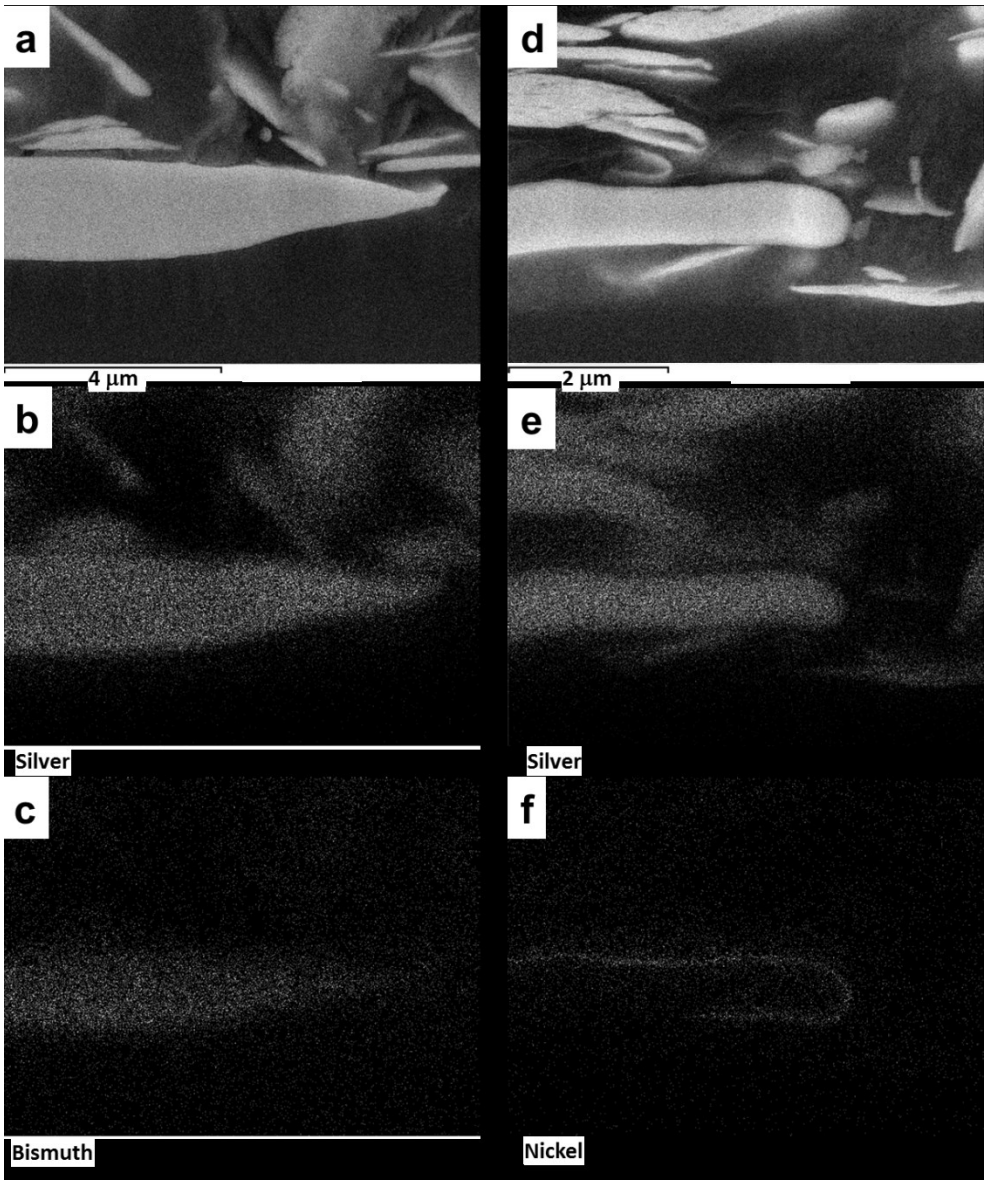

Figure 4.10: EDS maps of a,b,c) Bi-Ag layered films and d,e,f) Ni-Ag layered films.

EDS of the ridge cross-sections confirm our expectations where we see a general mixing of Bi and Ag in **Figure 4.10c**, but significant phase segregation in **Figure 4.10f**, where Ni is seen nearly encapsulating the delaminated Ag ridge structure. In both cases, the absorption film was successful in lowering the 12.5 J/m scan line energy required to dewet the highly reflective Ag films. Addition of the bismuth NIR absorption film enables a decrease to 10 J/m while addition of a nickel NIR absorption film enables

a decrease to 3.33 J/m. NIR absorption layers could enable 1070 nm processing of other highly reflective metals such as gold, aluminum, or copper with minimal change in base composition. Alternatively, the results suggest a coating of a high absorption film with a near matching T_m of the high reflectance film would be the most optimal.

The ridge profiles of the layered films exhibit low height to width aspect ratios on the order of 0.2:1. Furthermore, the receding dynamic contact angles for the bismuth-silver ridges vary between 66° and 120° depending on the level of delamination near the edge. These ridges are highly irregular in height and are indicative of unequal melting and solidification rates throughout the film. This may be a result of heterogeneous absorption at the film surface from the existence of impurities or local defects in the surface roughness. Such defects could also manifest as irregular heat conduction within the bulk of the film during laser processing. To explore in more detail, a homogenizing anneal step was carried out on a set of Bi-Ag films. Films were annealed at 250 °C for two hours under a flowing Ar-gas environment, after which a line array with a 100 μm pitch was scanned into the film. The ridge morphology observed in the processed films appeared much more uniform with lower instability growth rates (**Figure 4.11a**). Variation in the receding contact angle reduced significantly to a narrow range between 40° and 45°. EDS mapping of the elements show a large amount of phase segregation in the dewetted ridge, which indicates a change in the rate and direction of the cooling. The reduction in the receding contact angle also reduces the growth rate of instabilities in the ridge.[28] Thus, such instabilities do not appear with the same frequency or amplitude as observed in the un-annealed films. In summary, internal stresses and defects that are present in the as-deposited film contribute in a significant manner to the irregularities observed in the dewetted films. A short anneal improves the uniformity of the film and the dewetted ridge significantly.

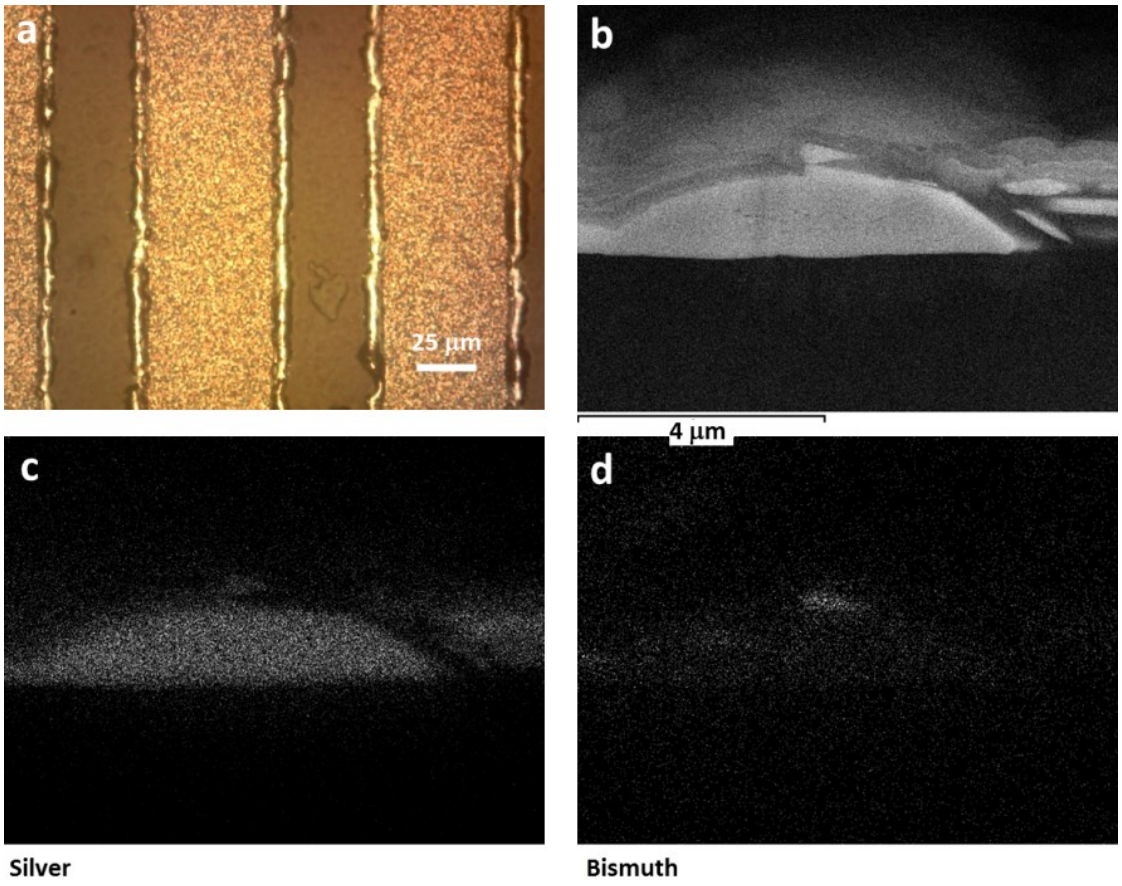

Figure 4.11: Pre-annealed Bi-Ag film under a) optical microscopy. Lines scans were set at a 100 μm pitch length. Cross-sections under b) FESEM imaging allowed for EDS maps of c) silver and d) bismuth distribution.

4.3.2 Complex/Push Dewetting

Ultimately, the advantages of using the scan-system manifest in the ability to quickly make complicated and free-form shapes. Inter-digit electrode pairs were patterned into both single-layer sets of films. By measuring the resistivity between the two electrodes, we are able to characterize the extent to which dewetting occurs as well as demonstrating a moderately complex pattern design. **Figure 4.12** presents an example of such an IDE created in silver films. Two-wire resistance measurements on both sets of IDEs generate values beyond the giga-ohm capabilities of the multi-meter. Therefore

it is concluded that the dewetting action proceeds completely and does not leave any percolated conductive metal or by-products in either type of IDE. The EDS maps presented in **Figure 4.9** also confirm the lack of any significant amount of residual metal within the trench area. Lift-off of the Par-C from the glass slide backbone is carried out, thus producing an IDE patterned onto a flexible, free-standing polymer as seen in **Figure 4.12b**.

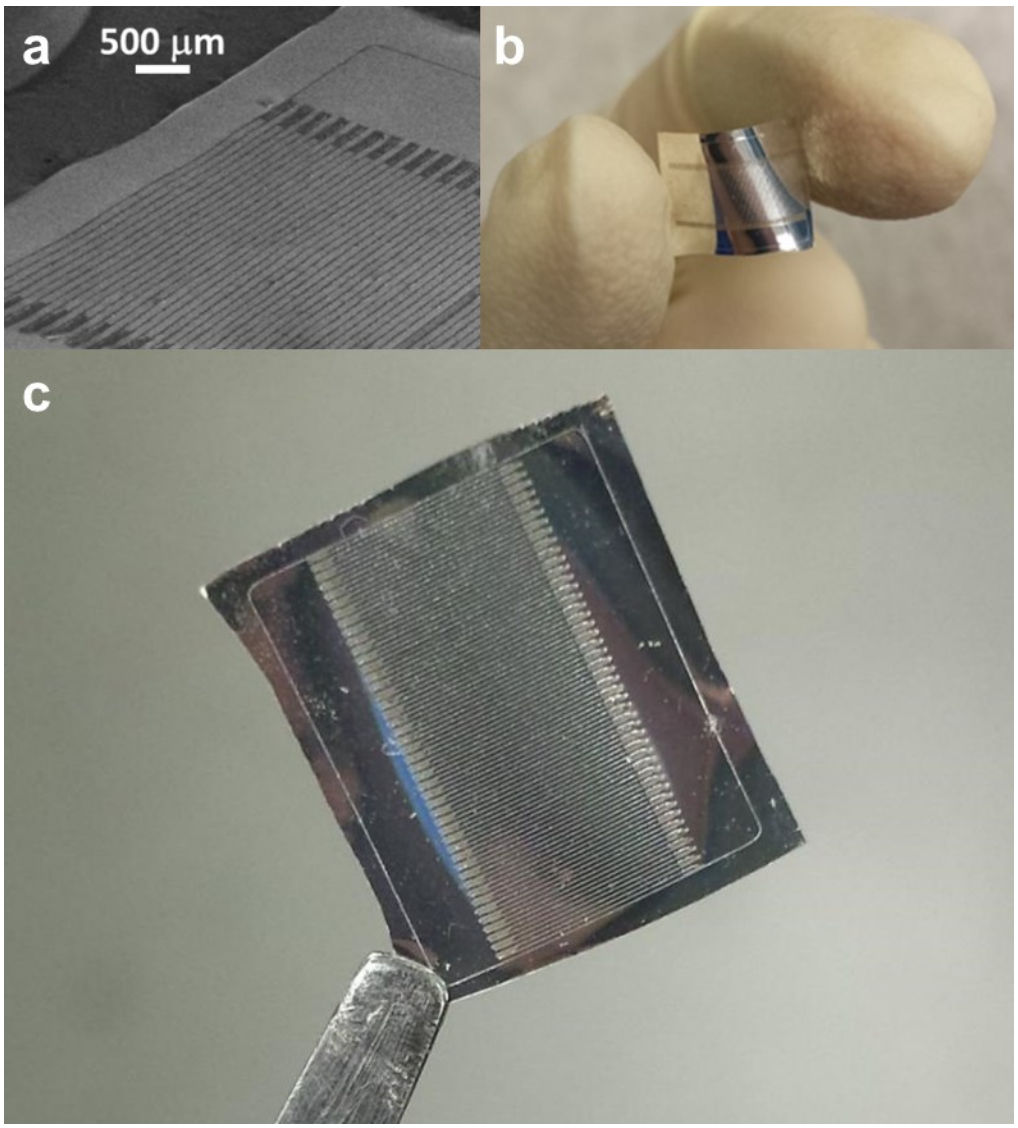

Figure 4.12: An inter-digit electrode dewetted from a silver film deposited upon parylene-C, imaged using a) FESEM. The IDE can be removed from the glass slide as b,c) a flexible and free-standing film.

Use of the scanner allowed successive, overlapping passes of the laser beam within a single pattern. This type of scanning induces a build up along dewetting front edge. Previous work on bismuth and tin thin films demonstrated that this build up can be manipulated via different scanning geometries to produce structures many times thicker than the original deposited film[19]. Attempts to perform such "push" dewetting on nickel films were realized but within certain limitations. Height measurements (**Figure 4.13a**) demonstrate a preferential dewetting to one side of the exposure trenches, which confirms that the dewetting material is indeed favoring the side of advancing exposure scans. **Figure 4.13b** diagrams the scanning procedure, where three scans are carried out with partial overlap in numerical order. A side effect of the pushing procedure manifests as a smoothing of the slightly scalloped edge profile of the trench/ridge interface. This is most pronounced in **Figure 4.13b** where the non-pushed edge appears ragged, while the built up edge at the end of the dewetting front presents as relatively smooth.

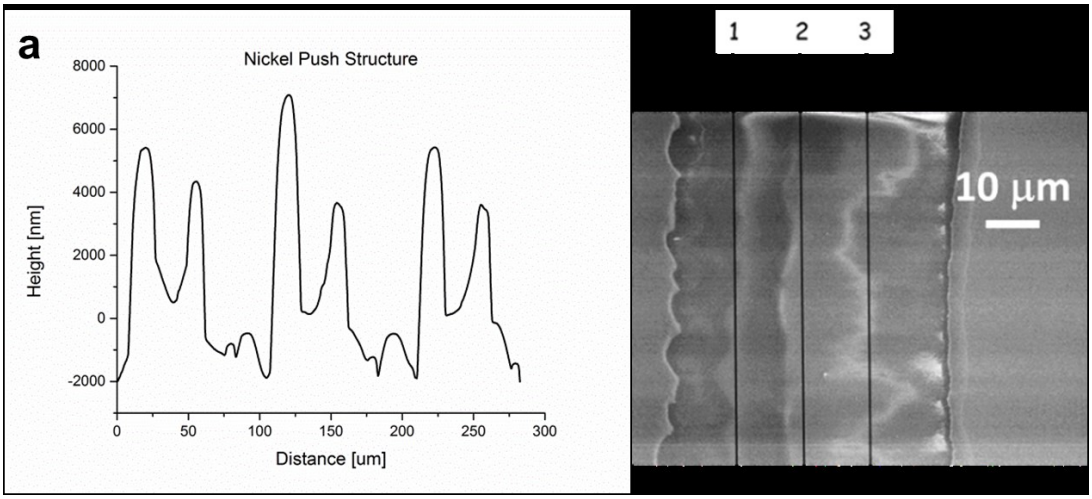

Figure 4.13: Example of a push structure using nickel films on Par-C substrates as seen via a) profilometry and b) FESEM. Successive, overlapping laser scans induce a progressive and directional dewetting front in the nickel film that produces thicker, smoother ridges without the need for additional depositions.

4.4. Discussion

The results have shown that it is possible to extend the thermocapillary directed dewetting technique beyond the previously demonstrated low melting point metals to metals exhibit very high melting points and laser energy reflection. Despite the high melting temperature of nickel and high reflectivity of silver, dewetted features are possible under scanned, near-infrared laser heating. Use of a powerful laser with high-beam quality remains essential for successful patterning as the Gaussian spatial distribution of intensity drives the flow.

Herein, absorption layers are shown to decrease the need for such high average power output for highly reflective films such as Ag; however, use of visible or ultraviolet laser radiation may offer another avenue for approach. Silver experiences an increase in theoretical absorptivity for wavelengths at the near-UV range to nearly 24% - a stark difference from the < 5% observed in the near-IR range. Wavelengths in the mid-UV range, such as those from a frequency quadrupled Nd:YAG laser (266 nm), are absorbed at a theoretical 75% and therefore would not require the high average power exerted by the current laser system. Shorter wavelength lasers would also allow for smaller ultimate spot sizes and thus higher resolution features with more effective dewetting on thinner films. One drawback to using a UV laser source may manifest in the absorption properties of the polymer substrate. Parylene-C sees an increase in absorption in the UV range and may experience destruction during laser exposure. There are alternatives, however, such as polydimethylsiloxane (PDMS) or certain polyvinylidene fluoride (PVDF) variations that will pass UV radiation to a higher degree, but still have the benefit of exhibiting a low surface energy.

The use of a large surface energy differences between the target metal film and polymer substrate allows the thermodynamically favorable dewetting to occur quickly

once heated, but as observed in the plain Ni films, problems with adhesion may develop. These adhesion problems were not observed in the other tested films to the same extent, so it may be inferred that there exists a certain range of target/substrate surface energy disparity beyond which dewetting becomes impractical. Modification of the polymer surface to increase the surface energy prior to metal deposition may prove useful in avoiding delamination while still allowing laser-directed dewetting. This becomes especially important for flexible electronics that must withstand certain amounts of strain and deformation without delamination of the constituent layers.

In summary, it has been demonstrated that high melting point, high reflectivity metals may be dewetted into patterns via a scanning laser beam. High average powers are used to quickly heat the target films to their melting point, after which the spatial variation of the laser beam will induce a thermocapillary flow away from the center point of exposure. Substrate destruction is avoided by using a polymer with high transmittance at the laser operating wavelength. Metals with elevated reflectivity rates can be patterned using high laser intensities or by depositing thin absorption layers. Annealing procedures ensure that dewetted features are uniform with minimal instability growth. Use of the scan system allows for complex shapes to be dewetted into the metallic target layer which may be cut out to form stand-alone films on flexible substrates. Resistance measurements ensure that a single pass of the laser leaves no connecting conductive material in the exposed area, thus ensuring electrically isolated features. Finally, by making partially overlapping passes, the dewetting high temperature metal is able to be “pushed” in a directional manner, which gives rise to thicker features without the need for additional deposition steps.

4.5. References

1. Krishna H, Sachan R, Strader J, Favazza C, Khenner M, Kalyanaraman R. Thickness-dependent spontaneous dewetting morphology of ultrathin ag films. *Nanotechnology*. 2010;21:155601.
2. Xie R, Karim A, Douglas JF, Han CC, Weiss RA. Spinodal dewetting of thin polymer films. *Physical Review Letters*. 1998;81(6):1251-1254.
3. Favazza C, Kalyanaraman R, Sureshkumar R. Robust nanopatterning by laser-induced dewetting of metal nanofilms. *Nanotechnology*. 2006;17:4234.
4. Singh SP. Spinodal theory: A common rupturing mechanism in spinodal dewetting and surface directed phase separation (some technological aspects: Spatial correlations and the significance of dipole-quadrupole interaction in spinodal dewetting). *Advances in Condensed Matter Physics*. 2011;2011. doi: 10.1155/2011/526397.
5. Cavallini M, Biscarini F, Leon S, Zerbetto F, Bottari G, Leigh DA. Information storage using supramolecular surface patterns. *Science*. 2003;299(5606):531-531. http://www.sciencemag.org/cgi/doi/10.1126/science.1078012. doi: 10.1126/science.1078012.
6. Ghezzi, Thickett, Neto. Early and intermediate stages of guided dewetting in polystyrene thin films. *Langmuir*. 2012;28(27):10147-10151. http://pubs.acs.org/doi/abs/10.1021/la301773h. doi: 10.1021/la301773h.
7. Cavallini, Gentili, Greco, Valle, Biscarini. Micro- and nanopatterning by lithographically controlled wetting. *Nature Protocols*. 2012;7(9):1668-1676. http://www.nature.com/doifinder/10.1038/nprot.2012.094. doi: 10.1038/nprot.2012.094.
8. Bystrenova E, Facchini M, Cavallini M, Cacace MG, Biscarini F. Multiple length-scale patterning of DNA by stamp-assisted deposition. *Angewandte Chemie International Edition*. 2006;45(29):4779–4782. http://onlinelibrary.wiley.com/doi/10.1002/anie.200600114/full. doi: 10.1002/anie.200600114.
9. Herz, Wang, Schaaf. Dewetting of au/ni bilayer films on prepatterned substrates and the formation of arrays of supersaturated au-ni nanoparticles. *Journal of Vacuum Science & Technology B: Microelectronics and Nanometer Structures*. 2014;32(2):021802. http://scitation.aip.org/content/avs/journal/jvstb/32/2/10.1116/1.4863320. doi: 10.1116/1.4863320.
10. Wang, Ji, Schaaf. Formation of precise 2D au particle arrays via thermally induced dewetting on pre-patterned substrates. *Beilstein Journal of Nanotechnology*. 2011;2:318-326. http://www.beilstein-journals.org/bjnano/content/2/1/37. doi: 10.3762/bjnano.2.37.
11. Sharma A, Ruckenstein E. Energetic criteria for the breakup of liquid films on nonwetting solid surfaces. *Journal of Colloid and Interface Science*. 1990.
12. Kim, Giermann, Thompson. Solid-state dewetting of patterned thin films. *Applied Physics Letters*. 2009;95(25):251903. http://scitation.aip.org/content/aip/journal/apl/95/25/10.1063/1.3268477. doi: 10.1063/1.3268477.
13. Ye J, Thompson CV. Anisotropic edge retraction and hole growth during solid-state dewetting of single crystal nickel thin films. *Acta Materialia*. 2011;59(2):582-589.

http://www.sciencedirect.com/science/article/pii/S1359645410006397. doi: 10.1016/j.actamat.2010.09.062.
14. Basu, Carter, Divakar, Mukherjee, Ravishankar. Nanopatterning by solid-state dewetting on reconstructed ceramic surfaces. *Applied Physics Letters*. 2009;94(17):171114. http://scitation.aip.org/content/aip/journal/apl/94/17/10.1063/1.3127442. doi: 10.1063/1.3127442.
15. Fowlkes JD, Kondic L, Diez J, Wu Y, Rack PD. Self-assembly versus directed assembly of nanoparticles via pulsed laser induced dewetting of patterned metal films. *Nano Lett*. 2011;11:2478-2485.
16. Kuznetsov A, Koch J, Chichkov B. Nanostructuring of thin gold films by femtosecond lasers. *Appl Phys A*. 2009;94:221-230.
17. Rack PD, Guan Y, Fowlkes JD, Melechko AV, Simpson ML. Pulsed laser dewetting of patterned thin metal films: A means of directed assembly. *Appl Phys Lett*. 2008;92:223108.
18. Singer JP, Lin P, Kooi SE, Kimerling LC, Michel J, Thomas EL. Direct-write thermocapillary dewetting of polymer thin films by a laser-induced thermal gradient. *Advanced Materials*. 2013;25:6100-6105. doi: 10.1002/adma.201302777.
19. Ferrer AJ, Halajko A, Amatucci GG. Micro-patterning of metallic film structures through direct-write dewetting. *Advanced Engineering Materials*. 2014;16(9):1167–1178. http://onlinelibrary.wiley.com/doi/10.1002/adem.201400240/abstract. doi: 10.1002/adem.201400240.
20. Xiao SY, Che LF, Li XX, Wang YL. A novel fabrication process of MEMS devices on polyimide flexible substrates. *Microelectronic Engineering*. 2008;85(2):452-457. http://www.sciencedirect.com/science/article/pii/S0167931707006582. doi: 10.1016/j.mee.2007.08.004.
21. Miyoshi Y, Tkeuchi T, Saito T, et al. A wearable humidity sensor with hydrophilic membrane by soft-MEMS techniques. *2nd IEEE International Conference on Nano/Micro Engineered and Molecular Systems, 2007. NEMS '07*. January 2007:211-214. doi: 10.1109/NEMS.2007.352264.
22. Noha H, Huangb Y, Hesketha PJ. Parylene micromolding, a rapid and low-cost fabrication method for parylene microchannel. *Sensors and Actuators B: Chemical*. 2004;102(1):78-85. http://www.sciencedirect.com/science/article/pii/S0925400504004769. doi: 10.1016/j.snb.2003.09.038.
23. Lienhard D, Heepmann F, Ploss B. Thin nickel films as absorbers in pyroelectric sensor arrays. *Microelectronic Engineering*. 1995;29(1–4):101-104. http://www.sciencedirect.com/science/article/pii/0167931795001247. doi: 10.1016/0167-9317(95)00124-7.
24. Choi J, Sung W. A PLANAR AND MEMBRANELESS MICROSCALE FUEL CELL USING NICKEL AND SILVER AS CATALYSTS. *The 13th International Conference on Solid-State Sensors, Actuators, and Microsystems*. 2005:1852-1855. doi: 10.1 pW/cm2.
25. Haynes WM, ed. *CRC handbook of chemistry and physics.* 95th ed. Boca Raton, FL: CRC Press/Taylor and Francis; 2015.
26. Wyart, Daillant. Drying of solids wetted by thin liquid films. *Canadian Journal of Physics*. 1990;68(9):1084-1088. http://www.nrcresearchpress.com/doi/abs/10.1139/p90-151. doi: 10.1139/p90-151.
27. Mills, Fry. Rate of evaporation of hydrocarbons from a hot surface: Nukiyama and leidenfrost temperatures. *European Journal of Physics*. 1982;3(3):152-154. http://stacks.iop.org/0143-

0807/3/i=3/a=005?key=crossref.84acc51fced5e38663a33f4e2f090d87. doi: 10.1088/0143-0807/3/3/005.
28. Choi S, Newby BZ. Dynamic contact angle in rim instability of dewetting holes. *J Chem Phys*. 2006;124(5):054702.
29. Brochard-Wyart, Redon. Dynamics of liquid rim instabilities. *Langmuir*. 1992;8(9):2324-2329. http://pubs.acs.org/doi/abs/10.1021/la00045a041. doi: 10.1021/la00045a041.
30. Sekimot K, Oguma R, Kawasaki K. Morphological stability analysis of partial wetting. *Annals of Physics*. 1987;176(2):359-392. http://www.sciencedirect.com/science/article/pii/0003491687900078#. doi: 10.1016/0003-4916(87)90007-8.
31. Thomy, Seefeld, Vollertsen. The occurrence of humping in welding with highest beam qualities. *Key Engineering Materials*. 2007;344:731-743. http://www.scientific.net/KEM.344http://www.scientific.net/KEM.344.731. doi: 10.4028/www.scientific.net/KEM.344.
32. Tyson WR, Miller WA. Surface free energies of solid metals: Estimation from liquid surface tension measurements. *Surface Science*. 1977;62(1):267-276. http://www.sciencedirect.com/science/article/pii/0039602877904423. doi: 10.1016/0039-6028(77)90442-3.
33. Weissler GL. *Vacuum physics and technology*. 2nd ed. ; 1979.
34. Tan, Craighead. Surface engineering and patterning using parylene for biological applications. *Materials*. 2010;3(3):1803-1832. http://www.mdpi.com/1996-1944/3/3/1803/. doi: 10.3390/ma3031803.
35. R. H. French, "Optical Properties of Materials for Concentrator Photovoltaics." Presentation: 2009
36. Jeong YS, Ratier B, Moliton A, Guyard L. UV-visible and infrared characterization of poly(p-xylylene) films for waveguide applications and OLED encapsulation. *Synth Met*. 2002;127:193.
37. Rhee. Surface energies of silicate glasses calculated from their wettability data. *Journal of Materials Science*. 1977;12(4):823-824. http://link.springer.com/10.1007/BF00548176http://www.springerlink.com/index/pdf/10.1007/BF00548176. doi: 10.1007/BF00548176.
38. Gusarov A, Doyle D, Glebov L, Berghmans F. Radiation-induced transmission degradation of borosilicate crown optical glass from four different manufacturers. *Optical Engineering*. 2007;46(4):043004. doi: 10.1117/1.2722322.

5 Summary

We have shown that the meta-stability of thin metallic films can be exploited to great effect, especially when using polymer substrates. This direct-write dewetting can be used to accumulate material from a relatively large surface area of pre-deposited film to build out-of-plane structures of different heights without having to deposit or remove material. Geometries such as lines and hemispheres were built from surrounding material and exhibited increases of up to 4900% in thickness when compared to the original film. A number of contrasting and more complex pattern designs were created, including an inter-digit electrode design exhibiting complete electronic isolation, shapes and letters.

After the initial demonstration using Bi and Sn films, the explored technique was expanded. Successful dewetting of high temperature films such as nickel and silver was demonstrated. The limiting factor for dewetting these films seems to rest solely in the metal/polymer interface. The consequences of this interaction are two-fold. In cases where features are spaced apart and the spatial distribution of heat during processing is less concentrated, the films may display a delamination event. While it is unclear whether this event occurs prior or concurrent with the melting and dewetting, it is evident that the delamination partially shields the underlying polymer from the greatest amounts of conducting heat. For those processing regimes that have closely spaced features or for films that exhibit good initial adhesion, heat build-up in the underlying polymer substrate can lead to degradation and deformation of the polymer itself.

For processing films that require high intensity, heat build-up may be mitigated through use of the scan system. Higher speed processing enables high power dewetting of reflective films without the destruction of the sensitive polymer underneath. Additives to the surface of the such films reduces the need for such high intensity,

however, in-homogeneity of the films absorption and thermal conduction properties can lead to the growth of instabilities during the liquid phase of processing. For silver films, this can be mitigated by annealing steps that have the effect both of homogenizing the thermal properties of the film and by lowering the film's surface energy. Structures created out of built up nickel seem feasible, but are limited by the thermal stability of the substrates. Results suggest that small increases in feature height are possible through the use of overlapping laser scans, but are limited in size and volume. The success of this patterning technique is highly dependent on the manipulation of heat distributions within the target and underlying supporting films.

6 Future Work

This work represents the initial findings for a technique that has the potential for significant impact in the development of flexible electrode devices. The next steps in the development will most certainly deal in the optimization of processing regimes as well as the expansion of the technique for use with different target films, different substrate chemistries, and smaller length scales. A few areas of development are listed here:

1. Since the temperature distribution of the film stack remains the critical processing variable in this technique it is imperative that proper modelling and prediction is developed. A complete understanding in how processing parameters, target chemistry, and processing environment interact with regard to the thermal conduction of the films will allow future demonstrations of this technique to create even more complex designs with more rigid control over height.
2. Expansion of the possible film compositions may be carried out through investigations of different laser sources and surface treatments. It has been shown that most metals will absorb radiation with shorter wavelengths more efficiently, which suggests that such lasers would greatly expand the possible compositions used with this technique.

This work remains an initial demonstration of feasibility and looks to explore the potential of this processing method for use in MEMS systems. In this respect, pathways for improvement upon these methods may be as numerous as there are types of micro systems.